

MASTER THESIS

ADDITIVE MANUFACTURING OF INCONEL 718 FOR
AEROSPACE APPLICATIONS
TOWARDS PROCESS-MICROSTRUCTURE-PROPERTY RELATIONSHIPS



A. Hooghiemster

Faculty of Engineering Technology
Department of Mechanics of Solids, Surfaces and Systems
Chair of Production Technology

EXAMINATION COMMITTEE

Prof. dr. ir. R. Akkerman

Dr. ir. T.C. Bor

Dr. L. Cordova Gonzalez

Ir. M. van Ramshorst

Dr. ir. T.H.J. Vaneker

Confidential version

Enschede, The Netherlands
February 18, 2021

UNIVERSITY OF TWENTE.

Abstract

Additive manufacturing (AM) opens up new worlds of design freedom, enabling the rapid and mould-free production of complex parts for various industries, including the aerospace industry. Laser powder bed fusion (L-PBF) is an AM process capable of manufacturing complex-shaped parts by melting metallic powder using a laser, in a layer by layer fashion, directly from a Computer-aided design (CAD) model. In recent years the field of AM employing L-PBF has advanced rapidly. The quality of the produced parts is approaching the level required by the aerospace industry, mainly through advances in process control and process monitoring. Hence, the emphasis on the development of the L-PBF process may change from process control to microstructure control in order to prevent inconsistencies in the mechanical properties of complex-shaped aerospace parts.

This research project explores the relations between the process conditions, the development microstructure and the (mechanical) properties of a complex-shaped aerospace part employing Inconel 718, which is a well-known creep resistant, weldable and corrosion-resistant nickel-based superalloy. The influence of different geometrical features (i.e. overhangs, thin or thick sections and complex shapes), located within the complex aerospace part, on the microstructure and (mechanical) properties was studied. Also, the influence of a post-manufacturing heat treatment on the resulting microstructure and (mechanical) properties was included.

The examined aerospace part showed gas-induced porosity, lack of fusion and micro-scaled cracks close to the surface. Gas-induced porosity type was predominant, but the local density of the aerospace part was according to the requirement of 8.1 g/cm^3 . Large variations in surface roughness between different surfaces appeared. These were larger than the requirement of $3.175 \mu\text{m}$, except for the horizontal surface. Down-skin surface showed the highest average surface roughness of $21.3 \mu\text{m}$, compared to the lowest on the horizontal surface of $2.5 \mu\text{m}$. The as-built parts showed an inhomogeneous dendritic microstructure comprising in general columnar grains, oriented mostly parallel to the build direction. The grains extend through multiple as-deposited layers, due to epitaxial growth. The differences in local process conditions led to variations in the mechanical properties of the different geometrical features as observed through hardness measurements. After the post-manufacturing heat treatment, the samples showed a considerable increase in the hardness, with an average increase of 33 %. Moreover, the variations in hardness of the different geometrical features were also removed, yielding a part with almost uniform mechanical properties. Apparently, the post-manufacturing heat treatment is not only a powerful treatment to enhance the mechanical properties, but it also removes inhomogeneities in the mechanical properties, which are almost inevitable during manufacturing of products with complex features.

Thesis Committee

Prof. dr. ir. R. Akkerman
Professor
Chairman
Department of Mechanics of Solids, Surfaces & Systems (MS3)
University of Twente

Dr. ir. T.C. Bor
Associate Professor
Supervisor
Department of Mechanics of Solids, Surfaces & Systems (MS3)
University of Twente

Dr. L. Cordova Gonzalez
Assistant Professor
Supervisor
Department of Mechanics of Solids, Surfaces & Systems (MS3)
Fraunhofer Project Center & University of Twente

Ir. M. van Ramshorst
Mentor from company
Material and Process Engineer
Aeronamic B.V. (Almelo)

Dr. ir. T.H.J. Vaneker
Associate Professor
External member
Department of Design, Production and Management (DPM)
University of Twente

Acknowledgments

I am majoring in Mechanical Engineering, and I am a second-year master student at the University of Twente in Enschede. Before the Master, I completed HBO Mechanical Engineering and after that the Pre-master Mechanical Engineering track to be able to join the Master study. I have a comprehensive background in Design Engineering. My emphases are designing machines and constructions in 3D CAD software using AutoCAD, Inventor, Solid Edge and Solid Works.

This thesis report is about the project titled "Additive Manufacturing of Inconel 718 for Aerospace Applications towards Process-Microstructure-Properties Relationships". The research is performed on behalf of Aeronamic and cooperation with Fraunhofer Project Center and the University of Twente. The full-time graduation thesis duration was 9 months and my main goal was to extend my materials science knowledge, which includes experimental work, structure and properties of materials, crystallography and mechanical properties.

I would like to thank sincerely all the people who assisted me during my graduation project. My university supervisor Laura Cordova Gonzalez for the weekly meetings, her professional knowledge and support throughout this graduation project. My supervisor Ton Bor from the University of Twente for the very critical questions and his great knowledge of materials science. I would also like to thank Nick Helthuis for assisting me in the production lab during the experimental work.

I would like to thank Aeronamic, and especially I want to thank Maarten van Ramshorst for making it able to do this graduation project and provide me with the experimental materials and knowledge. I would also like to thank his colleague Peter Oomen who was always there to help me when Maarten was not available. Peter also gave a helping hand to bring samples to me, which saved me a lot of time.

Enschede, February 2021

Arjen Hooghiemster

Contents

Abstract	iii
Acknowledgements	v
List of Figures	3
List of Tables	7
List of Abbreviations	8
1 Introduction	9
1.1 Background	9
1.1.1 Laser powder bed fusion	9
1.1.2 Inconel 718	11
1.2 The part	11
1.3 Research objectives	12
1.4 Method	13
2 Literature review	14
2.1 Alloy Inconel 718	14
2.1.1 Microstructural phases	14
2.1.2 Formation of phases	16
2.2 Microstructure of additive manufactured parts	16
2.2.1 Melt pool characteristics	17
2.2.2 Grain morphology	17
2.2.3 Grain texture and structure	19
2.2.4 Phases and precipitates	19
2.3 Process conditions during additive manufacturing	20
2.3.1 Process parameters	20
2.3.2 Support structure	21
2.3.3 Build orientation	21
2.3.4 Build height	23
2.4 Porosity	24
2.5 Surface conditions	25
2.6 Conclusions	27
3 Experimental procedures	28
3.1 Additive manufacturing machine and process parameters	28
3.2 Powder characteristics	28
3.3 In-process monitoring systems	29
3.3.1 Optical Tomography system	29
3.3.2 PowderBed system	31
3.4 Cutting plan	31
3.4.1 Labelling system	32
3.5 Heat treatment	33
3.6 Density measurements	34

3.7	Microscopy	35
3.8	Microhardness	36
4	Results	37
4.1	Powder characterisation	37
4.2	Process monitoring	38
4.3	Porosity determination	42
4.4	Surface topography	44
4.5	Microstructure observations	45
4.5.1	Microstructure analysis	46
4.5.2	Other observations	47
4.5.3	Melt pool characteristics analysis	48
4.5.4	Phases and precipitates	50
4.5.5	Grain morphology	53
4.6	Microhardness	54
5	Discussion	56
5.1	Process monitoring	56
5.1.1	Heat conduction during additive manufacturing	56
5.1.2	The outer ring section	59
5.1.3	The upper ring section	59
5.1.4	The vanes section	60
5.2	Microstructure development	62
5.2.1	The dendritic as-built microstructure	62
5.2.2	Grain structure	63
5.3	Effect of the heat treatment	64
6	Conclusions	67
6.1	Recommendations	68
6.2	Future work	68
	References	69
A	Detailed images of the part	74
B	Optical tomography images of the outer ring	75
C	Optical tomography images of the upper ring	76
D	Optical tomography images of the vanes	77
E	Powder bed images of the vanes	78
F	Micrographs showing porosity	79
G	Microstructure of the vanes	80
H	The cause of the contamination	81
I	Derivation of the thermal model	83

List of Figures

1	Schematic overview of L-PBF process (for further understanding see text) [1].	10
2	Most commonly considered process parameters in the L-PBF process [2].	10
3	(a and b) The inlet housing part manufactured using L-PBF with the support structures still attached. The circular red arrow indicates the rotational direction of the part (b). . . .	12
4	Crystal structure of (a) the gamma, (b) the gamma prime and (c) the gamma double prime [3].	15
5	Crystal structure of the delta phase [4].	15
6	IN718 time temperature transformation diagram for welds [5].	16
7	A representation of a melt pool. The cross-sectional area is indicated by the area enclosed by the dotted line [6].	17
8	Effect of laser power and scanning speed on melt pool (a) width and (b) depth [6].	18
9	Tensile load (a) parallel to the columnar grains and (b) perpendicular to the columnar grains [7].	18
10	IN718 solidification map for grain structures [2].	18
11	Schematic overview of solidification modes with respect to the thermal gradients and undercooling [8, 9].	19
12	Schematic representation of the manufactured samples with different inclination angles between the specimens and the build direction [10].	21
13	Scanning electron microscope images showing the Laves phase obtained at different inclination angle [10].	22
14	(a) The used laser scanning strategy and build direction of the samples. (b) The tensile samples. (c) The tensile sample after machining [7].	23
15	Hardness variations along the build height in the as-EBM-built and heat-treated state for longitudinal samples [11].	23
16	The influences of the laser power and scanning speed on the porosity [2].	24
17	M_d^o is the minimum layer thickness required to obtain full fusion and M_d is the depth of the melt pool. M_d^o is dependent on the coupled parameters hatch distance (w) and layer thickness (h) given a constant melt pool size [2].	25
18	Layer approximation of the CAD geometry which results in the staircase error [12].	25
19	R_a values for different build angles a) 0° build orientation (flat) with support structures under side 4, b) 60° build orientation, and c) 90° build orientation (vertical).	26
20	Powder size distribution graph of approximately 10 times reused IN718 powder particles.	29
21	EOS M290 L-PBF machine setup showing the laser heating the powder, the sCMOS camera capturing the OT images during manufacturing process and the EOSTATE PowderBed camera capturing images before and after a recoater cycle [13].	30
22	Emitted radiation during the L-PBF process [13].	31
23	Top view of the inlet housing part showing the first three cutting lines.	32
24	Overview of cutting lines to obtain a series of samples for further analysis. The top side numbers correspond to the same cross-section of the number of the bottom side due to the direction reversal of the y-coordinate.	32
25	Sample labelling system used in this research.	33
26	Graph showing the time-temperature curve of the solution and precipitation heat treatment applied on the IN718 samples [14].	34

27	The green arrows indicate surfaces that generally will be post-processed and the red arrows indicate the surfaces that were measured.	35
28	Features examined for microstructure analyses.	36
29	The microstructure of IN718 powder particles. (a) Optical micrograph of the cross-section of multiple powder particles; (b) SEM micrographs of a powder particle using back-scattered electrons; (c) Two locations used for EDS elemental mapping of the IN718 powder particle; (d) Chemical composition of the two locations.	37
30	(a) EBSD analysis shows the grains of the IN718 powder particles and (b) shows the different phases present in IN718 powder particles.	38
31	Raw data of the sCMOS camera monitoring the powder bed during manufacturing the inlet housing part. The brown graph represents the mean grey value from all pixels of a part for each layer. The purple graph, indicated with 1, represents the mean grey value of the support structure of the vanes. The indication list marks layers red that observed locally higher thermal radiation than a set threshold value of $4.5 \cdot 10^4$, see colourbar.	39
32	The mean hardness with plus-minus two times the standard deviation on the region with higher thermal radiation as compared to the other regions showing mean thermal radiation on the OT images. The locations of the measurements are also shown.	40
33	3D model of the OT images created by the software ImageJ. The colourbar in Figure 31 gives the relation between the colour and the thermal radiation.	40
34	The grain size distribution of the bulk bottom and bulk top in the as-built state.	41
35	Schematic drawing of the build process of the vane.	42
36	The surface topography maps of (a) the vane showing high thermal radiation and (b) the vane showing mean thermal radiation.	42
37	Graph showing the mean density of the as-built (blue dots) and the heat-treated (red dots) samples with plus-minus two times the standard deviation (solid black lines) of each sample. The location of each sample within the part is also indicated.	43
38	Optical micrographs of the as-built vane (AS-1) showing gas-induced porosity, process-induced porosity and micro-cracks.	44
39	Graph showing the average surface roughness (blue) and the plus-minus one times standard deviation (black). The red line indicates the surface roughness requirement given by Aeronamic. The locations of the measurements are shown in Figure 27.	45
40	The surface topography maps of (a) the horizontal surface (AS-3) and (b) the 45-degree up-skin (AS-5) with recognizable scanning lines (red arrows) and unmelted powder particles stuck to the surface (black arrows).	45
41	The etched microstructure of the bulk bottom sample in (a) as-built (AS-1) and (b) heat-treated state (HT-1). The build direction (BD) is orientated upward.	46
42	The etched microstructure of the 45-degree overhang in (a) as-built (AS-7) and (b) heat-treated state (HT-7).	46
43	The etched microstructure of the vane in as-built state (AS-1).	47
44	(a) Optical micrograph showing contamination after etching a sample with a solution and precipitation heat treatment (HT-1 bulk bottom) and a pore indicate the cause of the contamination and (b) showing SEM image with the contamination of the vane after etching with only precipitation heat treatment (HT-1).	48
45	The melt pools of the bottom bulk (AS-1) manufactured with the part infill process parameters.	49

46	Optical micrographs of the melt pools (AS-1) showing porosity at the melt pool boundaries. It was manufactured with the part infill process parameters.	49
47	Schematic of the laser absorption mechanism during L-PBF process taken from [15].	50
48	BSE micrographs of the bulk bottom in as-built state (AS-1) showing (a) columnar dendritic structures, grains boundaries, (b) change of dendritic arm spacing crossing a melt pool boundaries and columnar dendrites crossing melt pool boundaries.	51
49	BSE micrograph of the bulk bottom (AS-1) showing the dendrites with hexagonal pattern, columnar dendrites and carbides.	51
50	BSE micrographs showing the heat-treated micrograph of (a) and (b) the bulk top (HT-4), (c) bulk bottom (AS-1) (D) needle-like precipitate located in the bulk bottom (AS-1). The (b) and (c) micrographs showing disk-shaped precipitates distributed in the gamma matrix.	52
51	EBSD analyses showing the grains and the zig-zag pattern of the grains in the bulk bottom in the (a) as-built (AS-1) and (b) heat-treated state (HT-1).	53
52	Grains size distribution of the bulk bottom, the 45-degree and the vane in (a) the as-built and (b) heat-treated state.	54
53	(a) showing micro-hardness of as-built and heat-treated samples with the mean and plus-minus two time standard deviation at 4 different features and (b) showing the hardness indents of the as-built bulk bottom (AS-1).	55
54	Geometry used for the calculations of the heat build-up and solidification cooling rate.	57
55	(a) Graph showing the effect of the support height on the heat build-up for different values of volume fraction. The red vertical line indicates the height of the support structure used to manufacture the inlet housing part. (b) The cooling curve by manufacturing on solid material with no heat build-up and the cooling curve with heat build-up, manufacturing on support structure.	59
56	(a) Powder bed image showing no powder distributed at certain regions of the vanes after a recoating cycle, located on the top side of the part, indicated with the red arrows. (b) showing the high thermal radiation from the vanes at the location with no powder distributed, as seen in (a). The orientation of the vanes relative to the recoater direction (α) is also indicated. Note that the OT-image was taken from another inlet housing part, but the process parameters and shape of the vanes were similar.	60
57	Schematic overview of an overhang's orientation relative to the recoater direction, expressed in α , and increasing by turning the overhang in a clockwise direction.	61
58	(a) showing the warping principle, (b) the warping interaction with the recoater direction of the vanes located on the bottom half of Figure 56 ($\alpha = 0^\circ$) and (c) warping accumulation with the vanes located on the upper half ($\alpha = 180^\circ$) [16, 17].	61
59	Specimens with the same inclination angle of 25° but created at different angles of α [17]. The warpage level Δh deviates by different values of α and increases by larger angles of α	62
60	Schematic overview of the direction of the dendrites and the columnar grains with different crystalline orientations. The dendrites in the middle change their direction at melt pool boundaries, rotated 90° and pointed to the direction of the thermal gradient, creating a zigzag pattern [18].	63
61	(a-f) Schematic diagram with the morphology of the γ'' and γ' above a given size L of y' particles. For further understanding, see text. TEM micrographs obtained (g) after homogenisation for 48 h at 1200°C and ageing heat treatment of IN718 for 700°C for 524 hours and (H) for 770°C for 19 hours [19].	65

62	SEM micrograph showing γ'' precipitates and possible γ' precipitates. This micrograph shows the heat-treated bulk bottom (HT-1), taken from Figure 50c with higher magnification.	66
63	Detailed images of the inlet housing part, where (a) shows the front view and (b) depicts the bottom view. The transition from the support structure to the solid material exhibits warping up to 2 mm.	74
64	OT-images of the transition of support structure to the first few layers of the inlet housing part (1-2019-063). The support structure ends at layer 434 and the first layer of the inlet housing part is 435.	75
65	OT-images of the inlet housing part (1-2019-063) showing the high thermal radiation in the bulk material on the top.	76
66	OT-images of the vane depicted overheating on the down-skin of the vane.	77
67	Powder bed images of the vanes on layer 320 to 324 indicating areas of the vanes without powder distribution after a recoater cycle.	78
68	Non etched optical images showing the porosity.	79
69	(a) The etched microstructure of the vane in heat-treated state and (b) EBSD analysis showing an overview of the grains in the as-build state (AS-1).	80
70	Steps taken to find the root cause of the contamination and the contamination on the optical micrographs are shown at each step.	82

List of Tables

1	IN718 material properties of wrought, cast and L-PBF production process at room temperature [20–22].	11
2	Composition of IN718 according to AMS standard [22].	14
3	Microstructure of IN718 obtained after AS: as-built, ST: solution treatment and DA: double ageing.	20
4	Mechanical properties at room temperature of L-PBF IN718 specimens with solution and precipitation heat treatment [23].	22
5	Process parameters used to manufacture the inlet housing part with the EOS M290 L-PBF machine using IN718 powder particles.	28
6	Composition of fresh IN718 powder, utilised for manufacturing the inlet housing part, obtained from the supplier PraxAir.	29
7	Density and surface roughness measurements on the vanes which showed mean and high thermal radiation. The location of the peaks are shown in Figure 33.	42
8	The melt pool characteristics of four features manufactured with part infill process parameters.	49
9	Process parameters used to manufacture the inlet housing part and IN718 material properties used for the thermal calculations.	57
10	Table showing the results of the heat build-up, solidification rate and cooling time for manufacturing the part with and without support structure.	58

List of Abbreviations

AM	additive manufacturing.
BCT	body centered-tetragonal.
BD	build direction.
BSE	backscattered electrons.
CAD	computer-aided design.
CT	computed Tomography.
EBM	electron beam melting.
EBS	Electron BackScatter Diffraction.
EDS	Energy Dispersive X-ray Spectrometer.
FCC	face-centred cubic.
GA	gas atomisation.
HCP	hexagonal close-packed.
IN718	Inconel 718.
LED	linear energy density.
L-PBF	laser powder bed fusion.
MC	metal carbides.
MGV	mean grey value.
OM	optical microscope.
OP-S	oxide polishing suspension.
OT	optical tomography.
sCMOS	scientific Complementary Metal–Oxide–Semiconductor.
TEM	transmission electron microscopy.
TTT	time-temperature transformation.
UTS	ultimate tensile strength.
VED	volumetric energy density.
YS	yield strength.

1 Introduction

Aeronamic B.V. (Almelo) is a company that produces complex aerospace parts for the aerospace industry of commercial and military aircraft. Up to now, these parts were made by casting and afterwards machined to obtain the final geometry. Besides casting, Aeronamic wants to produce these complex parts by additive manufacturing (AM) using laser powder bed fusion (L-PBF) because the AM production process has a number of benefits Aeronamic is interested in, for example, design freedom. AM is a manufacturing process of 3D parts, made layer by layer, as opposed to conventional techniques that have a subtractive nature. There are more reasons why Aeronamic is investing money to replace the casting process. Firstly, the order process time of one year is too long. Secondly, since there is only one certified company that is able to cast the complex aerospace parts, the costs of those parts are relatively high. Finally, Aeronamic wants to become a leading and certified company for L-PBF-based aerospace parts to gain an advantage over their competition.

The complex parts that Aeronamic typically have to manufacture, contain different features such as overhangs, variable thickness, complex shapes, that make it challenging to obtain a manufactured product with a uniform microstructure and uniform mechanical properties. The material's microstructure is strongly linked to the process settings and the local heating/cooling conditions that provide the thermal history. Even with constant process settings, the thermal history of the complex part will vary from place to place, possibly leading to unwanted variations in microstructure and mechanical properties. So, Aeronamic wants to have insight into how the different features within the complex aerospace parts influence the manufacturing process parameters. Knowing this, Aeronamic can modify the manufacturing process parameters on the local area to control microstructure within the build.

To become an L-PBF certified supplier of high-quality aerospace parts, Aeronamic started cooperation with the Fraunhofer Project Center at the University of Twente with the aim to manufacture certified L-PBF aerospace parts, which can be used in the aerospace industry. This graduation project included collaboration with the Fraunhofer Project Center. This research was focused on studying process-microstructure-property relationships. So, the process conditions used to manufacture a complex aerospace part were related to the developed microstructure and the (mechanical) properties.

In this graduation thesis, the L-PBF process, the examined part's material Inconel 718 (IN718) and the main- and sub-research questions to obtain the process-microstructure-property relationships, are described in this Chapter 1. Chapter 2 represents the literature review to gain an understanding of the current state of AM IN718 by L-PBF. The process conditions, microstructure and properties of L-PBF manufactured parts obtained by previous researchers are discussed. Chapters 3, 4 and 5 describes the experimental procedure, the results obtained in this graduation thesis and the discussion of the results, respectively. Finally, the process-microstructure-property relationships obtained from the results and discussion are listed in the conclusions, see Chapter 6. In the end, the recommendations and future work are provided.

1.1 Background

This section describes the background information of the L-PBF process and an introduction to the material IN718. A more detailed description of the alloy IN718 is provided in the Literature review.

1.1.1 Laser powder bed fusion

Additive manufacturing (or also referred to as 3D printing or rapid prototyping) is a production process which converts digital 3D Computer-aided design (CAD) models into physical 3D parts from powder,

sheets or wires by building it in a layerwise fashion. L-PBF is one of the AM processes where thermal energy from a laser source is used to fuse or weld powder together in order to make 3D parts. According to I. Baturynska et al. this type of AM process is widely used to manufacture parts and therefore, more research activities are focused on the improvements of the product properties (physical, material and mechanical properties) [24]. The L-PBF process is schematically shown in Figure 1. A spreading mechanism (recoater) is used to homogeneously deposited powder particles from the powder reservoir over the build plate (substrate). Once a layer is deposited, a laser selectively melts powder particles together under the inert gas or vacuum atmosphere to prevent oxidation of the melt pool [2]. After each layer, a new layer of powder is deposited by the recoater (indicated in Figure 1 as roller) and the process repeats itself. Once the manufacturing process is finished, the part can be removed from the build plate and the remaining powder surrounding the part can be partially reused. The powder is usually reused to increase cost-efficiency and sustainability of the production process. However, reuse of powder particles is challenging due to various reasons including material degradation [25]. Support structures are usually used to maintain structural integrity of the part by mechanically supporting it and providing a way to dissipate the heat of the production process. Supports are not always needed because the powder surrounding the product being manufactured can be used as support material, leading to less wasted material. However, the support structures are much more efficient in dissipating the heat, as the powder particles act more like an insulator due to the air gap between the particles.

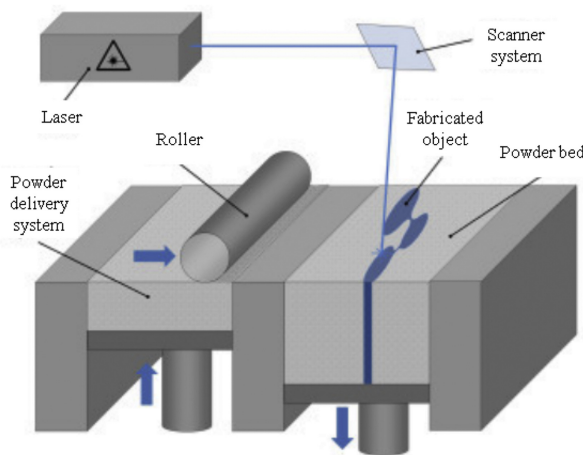


Figure 1: Schematic overview of L-PBF process (for further understanding see text) [1].

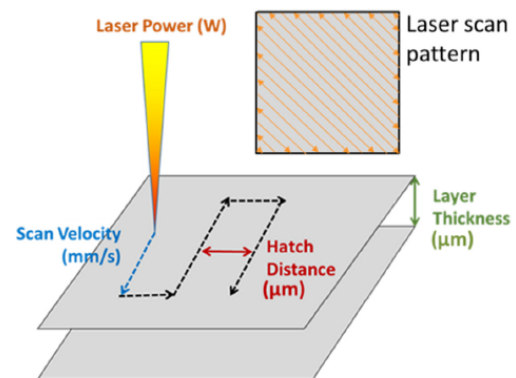


Figure 2: Most commonly considered process parameters in the L-PBF process [2].

L-PBF machine manufacturers have developed a set of optimum processing conditions (machine settings and process parameters) for different materials because of the complexity of the L-PBF process. The most commonly researched process parameters are shown in Figure 2 [2]. Important process parameters discussed in this report are the linear energy density (LED), see Equation 1, and the volumetric energy density (VED), see Equation 2. They are characterised by laser power (P), laser speed (v), hatch distance (w) and powder layer thickness (h). Laser power controls the amount of energy input into the powder bed. The laser speed (or scan velocity) is the speed of the laser scanning the powder particles. Lower scanning speed increases the dwelling time (interaction time between the laser and the powder particles) [26]. The hatch distance corresponds to the distance from the centre of two consecutive laser scans. The thickness of the powder layer is the height of the powder bed (the build plate) going down, which therefore equals the height of the powder particles spread by the recoater. Figure 2 also shows the laser scan pattern, which is the scan pattern followed sequentially by the laser tracks.

$$E_{lin} = \frac{P}{v} \text{ [J/mm]}. \quad (1)$$

$$E_{vol} = \frac{P}{v * w * h} \text{ [J/mm}^3\text{]}. \quad (2)$$

1.1.2 Inconel 718

IN718 is a nickel-based superalloy that is characterized by high strength at room and elevated temperatures, excellent weld-ability, corrosion resistance in both aqueous and high temperature and other physical properties [9]. However, these properties lead to poor machinability [27]. IN718 is mostly used in high-temperature applications, like aerospace, nuclear industry, turbines etc. which are regularly subjected to high mechanical loads. The excellent mechanical properties of IN718 are attributed to the presence of some key chemical elements in the composition like Ni, Nb, Cr, Fe and Ti. A more detailed description of the alloy IN718 is mentioned in the literature review, see Section 2.1.

Table 1 shows the mechanical properties of IN718 wrought, cast and L-PBF production methods. From Table 1, it can be concluded that the forged IN718 has higher mechanical properties as compared to cast production method. U. Glatzel et al. compared the mechanical properties of L-PBF material to forged and cast IN718. They concluded that the mechanical properties of the L-PBF manufactured parts are better than forged and cast products at room temperature, see Table 1, and display equal properties of forged at elevated temperatures [28]. However, inconsistency in (mechanical) properties of complex-shaped parts, produced by L-PBF, constrain the use in the aerospace industry [29]. The tensile specimens produced by L-PBF used for measuring the mechanical properties, given in Table 1, are machined and heat-treated after manufactured.

Table 1: IN718 material properties of wrought, cast and L-PBF production process at room temperature [20–22].

Properties	Forged AMS5662	IN718 Cast AMS5562	IN718 L-PBF (homogeniza- tion + ageing)
Melting range [°C]		1260 - 1336	
0.2 % Yield strength [MPa]	1034	758	1174
Ultimate tensile strength [MPa]	1276	862	1451
Elongation [%]	12	5	13.5
Microhardness [HRC]	40 (max)	30 (min)	45

1.2 The part

The aerospace part manufactured by Aeronamic and examined in this research is depicted in Figure 3. The working principle is as follows: The inlet housing part is clamped between two flanges, the upper and lower one (behind the support structure) and fixed with the mounting holes. Air goes from the top through part and the shape of the vanes inside the part creating a (clockwise) rotational thrust when air is going through the part, as seen in Figure 3b. The approximate dimensions of the inlet housing part are 170 mm in diameter and 50 mm in height. The inlet housing part must have the following requirements:

- The minimum local density of the part must be 8.1 g/cm³ (which is ≈ 99 % dense);
- No cracks are allowed;
- Porosity derived from lack of fusion is not allowed;

- The hardness requirement is 320 HV (\approx 35 HRC);
- Surface roughness (Ra) has to be smaller than $3.175\mu\text{m}$. Some surfaces of the part need lower surface roughness and this will be obtained by post-processing.

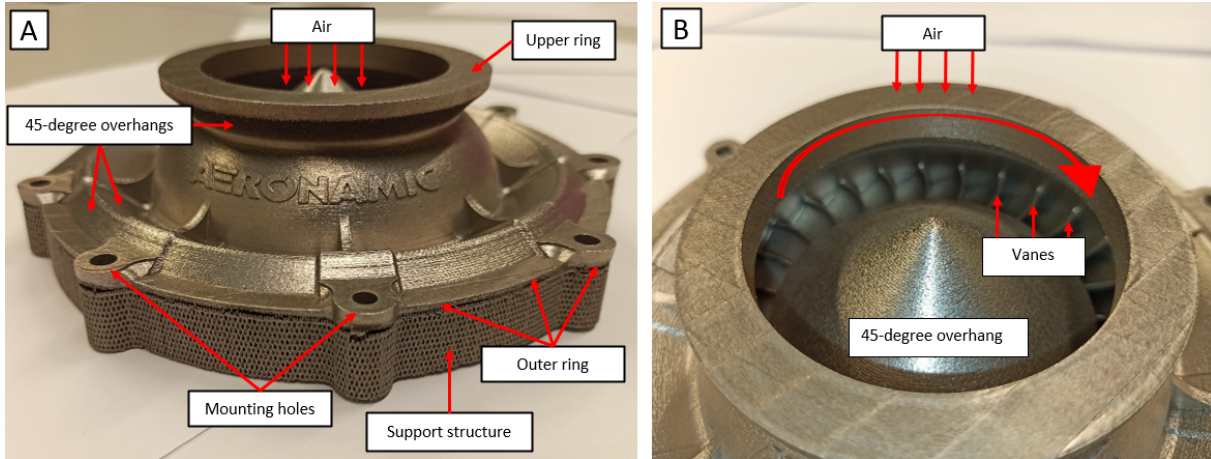


Figure 3: (a and b) The inlet housing part manufactured using L-PBF with the support structures still attached. The circular red arrow indicates the rotational direction of the part (b).

1.3 Research objectives

This research aimed to find the relation between the process conditions with the microstructure and (mechanical) properties of the complex-shaped aerospace part, depicted in Figure 3. The process conditions and the subsequent cooling rates determine the microstructure of the as-built conditions. The main focus of the process conditions is on the different geometrical features located within the part. Different geometrical features lead to differences in cooling rates and thus variations in microstructure and mechanical properties. The reason why and to what extent the microstructure and the mechanical properties vary in the as-built state are important. Often, additional heat treatments are given to the manufactured part to improve the mechanical properties. It is important to know the exact role of the heat treatment on the microstructure and mechanical properties. Do the process parameters have to be optimized in each feature in order to obtain similar cooling rates and thus homogeneous microstructure throughout the part or does the heat treatment erase the thermal history of the part. If the heat treatment erases the thermal history and the microstructure fulfils costumers needs, the process parameters can be optimized to manufacturing speed, prevention of porosity, optimisation of surface roughness etc. The following main-research question is formulated to find the relations between the process-microstructure-property.

Main research question:

- Why and to what extent do the microstructure and (mechanical) properties vary within the complex L-PBF manufactured aerospace part in as-built and heat-treated states by using IN718 as material?

The main research question is divided into multiple sub-research questions:

Sub-research questions:

- Which type of porosities are present and does the local density of the complex manufactured aerospace part meet the requirements of 8.1 g/cm^3 ?

- Which phenomenon is predominant in determining the surface roughness and is the surface roughness of the complex manufactured aerospace part within the requirements of $3.175\mu\text{m}$?
- What are the differences between the microstructure of the different geometrical features within the L-PBF manufactured aerospace part and why are these differences present?
- Why and to what extent do the solution and precipitation heat treatment, according to AMS2774 standard, influence the microstructure?
- Are there relations between the microstructure and the (mechanical) property after manufacturing and after heat treatment?
- How and to what extent can the Optical Tomography images be linked to microstructure, hardness, porosity and surface roughness variations?

1.4 Method

To obtain the goal of this research, the project consists of three main subjects: The Optical Tomography (OT) in-process monitoring system, microstructure and (mechanical) properties of different geometrical features, and post-manufacturing heat treatment. The OT images were captured during the manufacturing process of the inlet housing part. The OT images were used to discover if defects (i.e. porosity) or differences in microstructure and (mechanical) properties can be identified. OT images show the thermal radiation of each layer during the manufacturing process of the part. The aerospace part is cut into smaller samples to analyse the microstructure and (mechanical) properties on specific features. The literature review aimed to see which features located in the inlet housing part are interested to examine on density, surface roughness, microstructure and microhardness. Not all the features of the part matter cause certain regions will be machined afterwards. Finally, the influence of the post-manufactured heat treatment on the microstructure and (mechanical) are analysed. The approach of the research is described step by step in the Experimental chapter.

2 Literature review

The literature review was focused on finding the relations between the process condition, the microstructure and (mechanical) properties of different geometrical features within complex parts in the as-built and heat-treated state.

2.1 Alloy Inconel 718

IN718 is a nickel (Ni) based superalloy with high weld stability, corrosion resistance and microstructure stability at high temperature (650°C), which gives it incredible resistance to creep deformation [3]. Table 2 shows the chemical composition specification of the IN718 superalloy. The primary matrix is an austenitic gamma (γ) phase, based on Ni as primary element and strengthened by solid solution (alloying elements). The solid solution strengthening is achieved by adding alloying elements (Co, Cr, Fe, Mo, W and Ta) to the main crystalline lattice (γ) which have differences in atomic radii, leading to non-uniformity in the atomic lattice and inhibits dislocation movement [9]. The uniformity makes plastic deformation more difficult by suppressing dislocation movement, thus increasing the strength of the material.

IN718 is also strengthened by the precipitations of secondary phases (gamma prime and gamma double prime) in the primary γ -matrix. Precipitates or solid impurities are fine particles which hinder the movement of dislocations or defects in the crystal lattice and thus harden the material [30]. The formation of these precipitates is dependent on the solubility of solids at high temperature. Niobium (Nb) is an important element, since it forms the γ'' strengthening precipitates. The chemical elements aluminium (Al) and titanium (Ti) are essential elements for the gamma prime (γ') precipitates [9]. The excellent corrosion resistance property of IN718 is mainly due to the presence of 15 to 25 weight percent of chromium (Cr), which gives a protective surface oxide layer [31]. Boron (B) contributes to excellent creep properties of IN718 [31].

The most common phases in the γ -Ni microstructure of the alloy IN718 are, besides the γ' and γ'' , also the Delta (δ), MC-type carbides (metal carbides) and the Laves phase. These phases will be discussed in more detail in the following section.

Table 2: Composition of IN718 according to AMS standard [22].

Ni	Fe	Cr	Cu	Mo	Nb	C	Mn
50.00-55.00	Balance	17.00-21.00	0.30 max	2.80-3.30	4.75-5.50	0.08 max	0.35 max
P	S	Si	Ti	Al	Co	B	-
0.015 max	0.015 max	0.35 max	0.65-1.15	0.20-0.80	1.00 max	0.006 max	-

2.1.1 Microstructural phases

The gamma phase (γ) is the continuous matrix of IN718 and it is a solid solution phase with a face-centred cubic (FCC) crystal structure, see Figure 4a. The lattice constant (the physical dimension of unit cells) of the matrix is $a_\gamma = 0.3553 \text{ nm}$. Nickel is the primary element in the γ phase and retains its FCC structure up to its melt temperature [32]. The γ phase has a large capacity for solid solution hardening by elements such as Fe, Cr, Mo, W, V, Ti and Al, according to S. Azadian [31].

The gamma prime phase (γ') has a chemical composition of Ni_3Al or Ni_3Ti and also has an FCC crystal structure where aluminium or titanium occupies the corner sites and nickel atoms at the face centres, see Figure 4b [3]. The γ' phase is spherical in shape and has almost the same lattice parameters as the γ phase, ranging between $a_{\gamma'} = 0.3561$ to 0.3568 nm [9]. This phase looks almost similar to the γ

phase. However, the properties are different. The γ' phase is an inter-metallic structure because it tends to retain the order arrangement, which interferes with dislocation motion, thus strengthening the alloy. Generally, the γ' phase precipitates homogeneously in the γ phase matrix [31].

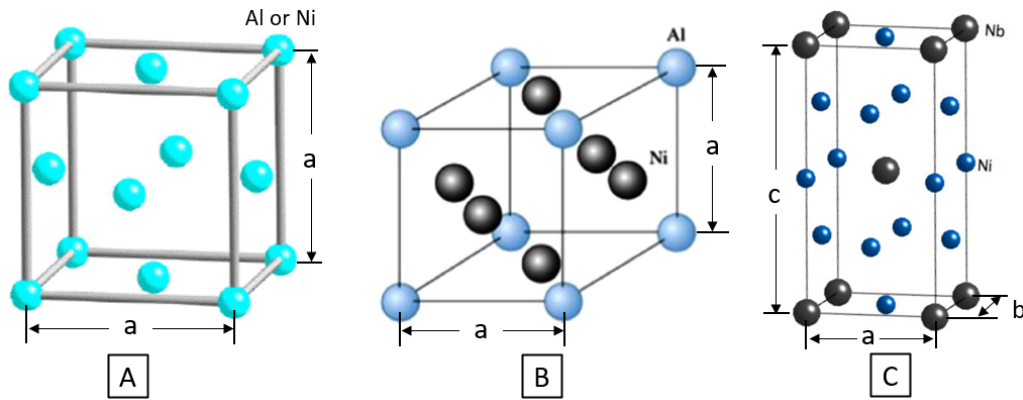


Figure 4: Crystal structure of (a) the gamma, (b) the gamma prime and (c) the gamma double prime [3].

The gamma double prime precipitates (γ'') have a chemical composition of Ni_3Nb and have a body centered-tetragonal (BCT) crystal structure, see Figure 4c. The lattice parameters are $a_{\gamma''} = b_{\gamma''} = 0.5093 \text{ nm}$ and $c_{\gamma''} = 0.7406 \text{ nm}$ [9]. The c-axis has a $c_{\gamma''}/a_{\gamma}$ ratio of 2. Besides the γ' precipitates IN718 is reinforced with meta stable, disk shaped γ'' precipitates and it retains its strength up to $650 \text{ }^\circ\text{C}$ due to the slow diffusion rates of the elements [33, 34]. At temperatures above $650 \text{ }^\circ\text{C}$, the γ'' phase will decompose to thermodynamic stable delta (δ) which is accompanied by a deterioration in mechanical properties and will be fully decomposed at $950 \text{ }^\circ\text{C}$.

The niobium rich delta phase (δ) has a needle-like shape and an orthorhombic crystal structure, see Figure 5. Its chemical composition is Ni_3Nb , which is the same as the γ'' phase but it has a different crystal structure. The growth of the δ phase occurs by solid-state diffusion at the expense of the γ'' and the growth rate is larger at higher temperatures up to the solvent temperature of $1000 \text{ }^\circ\text{C}$ [9]. The δ phase does not confer any strength to the γ matrix, leading to a loss in mechanical properties [29]. However, a small volume fraction of the δ phase at grain boundary can prevent grain growth and grain boundary sliding. Grain boundary sliding is one of the contributors to creep, improving the material's creep behaviour. [29, 33, 35].

Also, different types of MC carbides are formed in alloy IN718. NbC is the predominant carbide phase that is a niobium (Nb) rich MC-type carbide, where M is the metal component. The high content of Nb is known to favour the development of MC carbides in nickel-based superalloys [36]. According to H. K. D. H. Bhadeshia, the carbide tends to precipitate at grain boundaries and hence, reduces the tendency for grain boundary sliding [3].

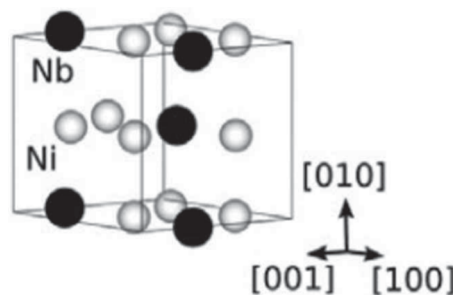


Figure 5: Crystal structure of the delta phase [4].

The Laves phase is a brittle intermetallic phase that has a hexagonal close-packed (HCP) crystal structure and has A_2B composition with Ni, CR and FE in position A and Nb, Mo and Ti in position B . The Laves phases is obtained in the last stage of the solidification process [9]. The Laves phase is an Nb rich phase that will take away the Nb from the γ'' strengthening precipitates. Also, the characteristic of being brittle reduces the mechanical properties [37]. It also contains the Mo, Ti and Ni elements which can also affect the solid solution strengthening and decrease the number of γ' phase to weaken the effect of precipitation, so it is considered that the Laves phase is undesirable, as mentioned by Popovich et al. [38].

2.1.2 Formation of phases

The solidification sequence of IN718 involves the initial precipitation of $L \rightarrow \gamma$ dendrites, in the direction of the heat flux, at the liquidus temperature and the interdendritic liquid remaining, enriches in Nb and C [39]. Further solidification, an eutectic reaction of $L \rightarrow \gamma + MC(NbC, TiC)$ carbides occurs and reduces the C content in the liquid [40]. The solidification terminates with the formation of the Laves phase by the $L \rightarrow \gamma + Laves$ phase eutectic reaction [39]. Strengthening precipitates mentioned in the previous section, are formed with heat treatments. The most common phases mentioned in the previous section are shown in the time-temperature transformation (TTT) diagram for isothermal treatment, see Figure 6. The TTT-diagram is a plot of temperature versus time which gives an insight into the phase transformations that will occur over time at a certain temperature. This TTT-diagram can be used to select heat treatments that produce a microstructure of interest [41].

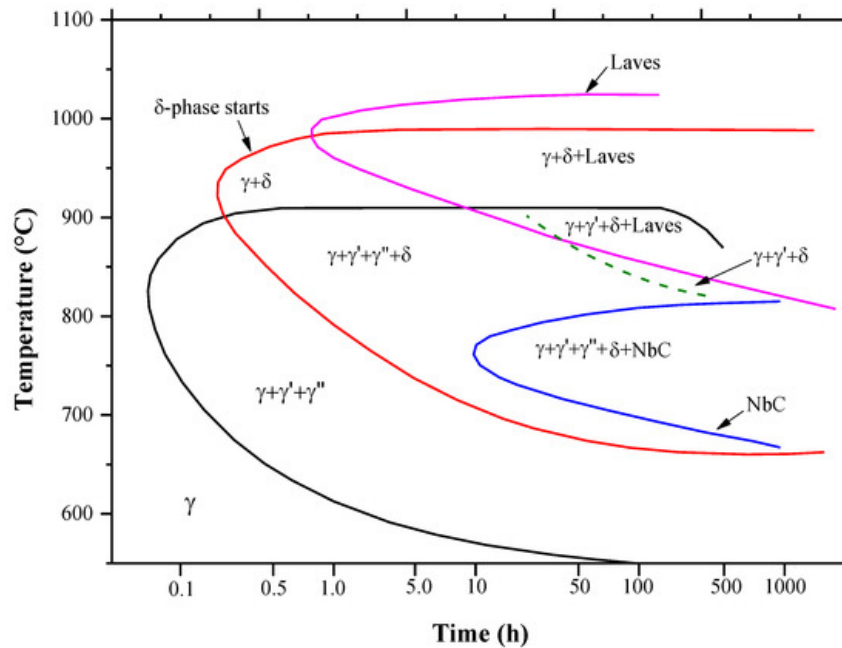


Figure 6: IN718 time temperature transformation diagram for welds [5].

2.2 Microstructure of additive manufactured parts

The microstructure of IN718 produced by L-PBF depends on the thermal history during the manufacturing process which can be controlled by the temperature gradient (G), the solidification velocity (R), under-cooling (ΔT) and eventually the heat flow during the solidification [38]. These parameters are influenced by the temperature development parameters (i.e. laser power, laser speed etc), the heat transfer

(absorption) of the laser to the melt pool. Besides, the heat dissipation plays an important role which is different on solid material than on powder material. This will be discussed in more detail in following sections.

2.2.1 Melt pool characteristics

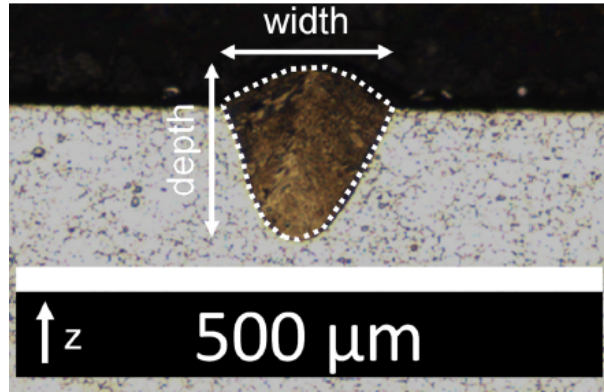


Figure 7: A representation of a melt pool. The cross-sectional area is indicated by the area enclosed by the dotted line [6].

J.P. Oliveira et al. noted that most of the materials-related properties are primarily determined at the melt pool level since microstructure is primarily controlled by solidification characteristics [2]. The cross-sectional area, depth and width of a melt pool are shown in Figure 7. The temperature of the melt pool is of great importance since it has an influence on the sputtering, the viscosity of the molten metal and the surface tension [42]. Sputtering occurs as a result of melt evaporation which ejects liquid droplets and non-melted powder particles around the melt pool. Overheating the melt pool causes sputtering and the intensity increases with an increase in LED. The viscosity of the molten metal is important because it influences the balling phenomenon, which will be discussed in Chapter 2.4. The melt pool's temperature increases with an increasing laser power but slightly decreases with an increasing laser velocity. The width and depth of the melt pool decrease by an increasing laser speed [6, 42]. The effect of the laser power and laser speed on the melt pool's width and depth are shown in Figure 8.

2.2.2 Grain morphology

The grain size and orientation have influence on the mechanical properties (yield strength, ultimate tensile strength, elongation and fatigue). The effect of the grain size can be explained with the Hall-Petch relation that describes the relationship with the yield strength and the grain size:

$$\sigma_y = \sigma_0 + \frac{k_{hall}}{\sqrt{d_{eff}}} \quad (3)$$

where σ_y , σ_0 , k_{hall} and d_{eff} are the yield strength, the friction strength, the Hall-Petch coefficient and the diameter of the grains, respectively. Equiaxed grains have the same dimensions in all directions and columnar grains are elongated in one direction [43]. The diameter of columnar grains depends primarily on the slip conditions, for example in an extreme assumption slip may be activated such that dislocations only propagate along the length of the columnar grains. As a consequence, it gives a high value of d , leading to lower σ_y , according to Gallmeyer et al. [44]. So, the mechanical properties of

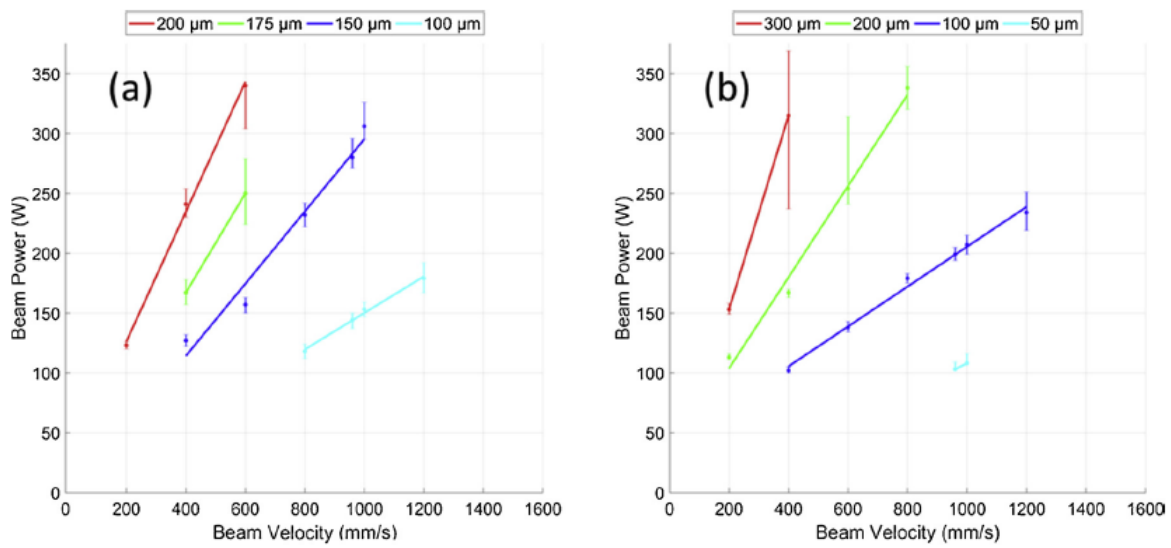


Figure 8: Effect of laser power and scanning speed on melt pool (a) width and (b) depth [6].

equiaxed grains are sort of similar in all direction, i.e. homogeneous/isotropic, whereas the properties of columnar grains are direction dependent/anisotropic.

Columnar grains typically form during the AM process in the solidification direction which is almost parallel to the building direction. Many studies concluded that horizontal tensile specimens show higher ultimate tensile strength (UTS) and yield strength (YS) but lower elongation than vertical ones [7, 11]. The anisotropy in ductility (elongation) is attributed to the different crack growth. For example, by applying a tensile force along with the columnar grains or perpendicular to them, see Figure 9. In both cases, they comply with Mode I opening tension, which is a tensile force applied normal to the plane of the crack. However, when the tensile load is parallel to the columnar grains, the cracks growth perpendicular to the building direction. There are only some short axes of the grains submitting to Mode I opening tension, which means more difficult for opening failure, so higher ductility, according to M. Ni et al. [7].

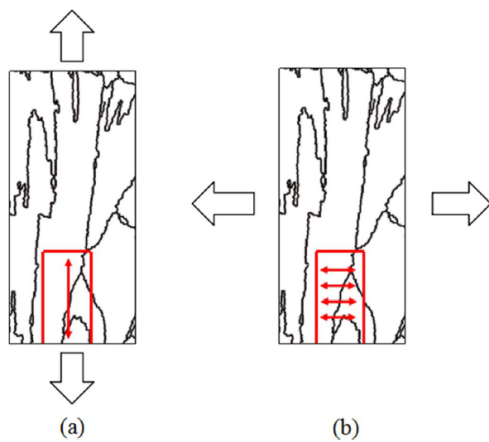


Figure 9: Tensile load (a) parallel to the columnar grains and (b) perpendicular to the columnar grains [7].

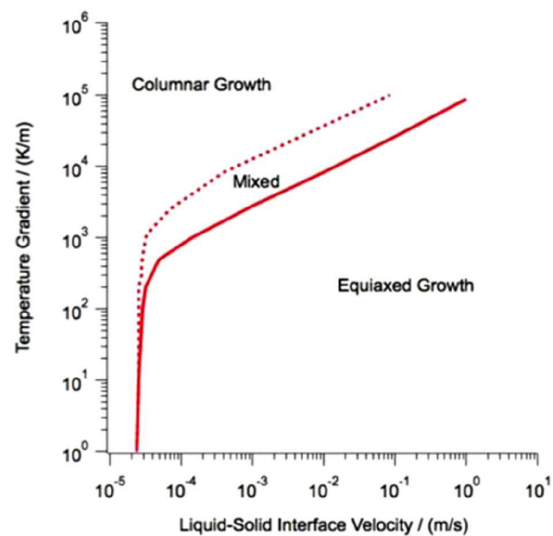


Figure 10: IN718 solidification map for grain structures [2].

2.2.3 Grain texture and structure

A strong morphology and crystallographic texture were observed in the columnar structures of IN718 part produced by L-PBF [42]. The grains growth direction are normally closely aligned to the build direction. According to Collins et al. [8] the transition between textured (columnar) and non-textured (equiaxed) structures has been related to spatial-temporal variation in the thermal gradient G and the solidification rate velocity R . This can be seen in the solidification map in Figure 10, where the dominant morphology and the presence or absence of texture can be predicted. The solidification microstructure also depends on the under-cooling (ΔT). The rapid conduction of heat creates undercooling large enough to stimulate dendritic solidification. [2]. So, undercooling drives dendritic growth and composition at the dendritic tip. The undercooling can exceed 50 - 100 K in the L-PBF process and is largely dependent on the G/R ratio. The G/R ratio also determines the formation of different microstructure types that can be seen in Figure 11 and the $G \cdot R$ ratio determines the size of the solidification structure. Lower cooling rates (lower $G \cdot R$) give coarser structure and higher cooling rates give finer structure [45].

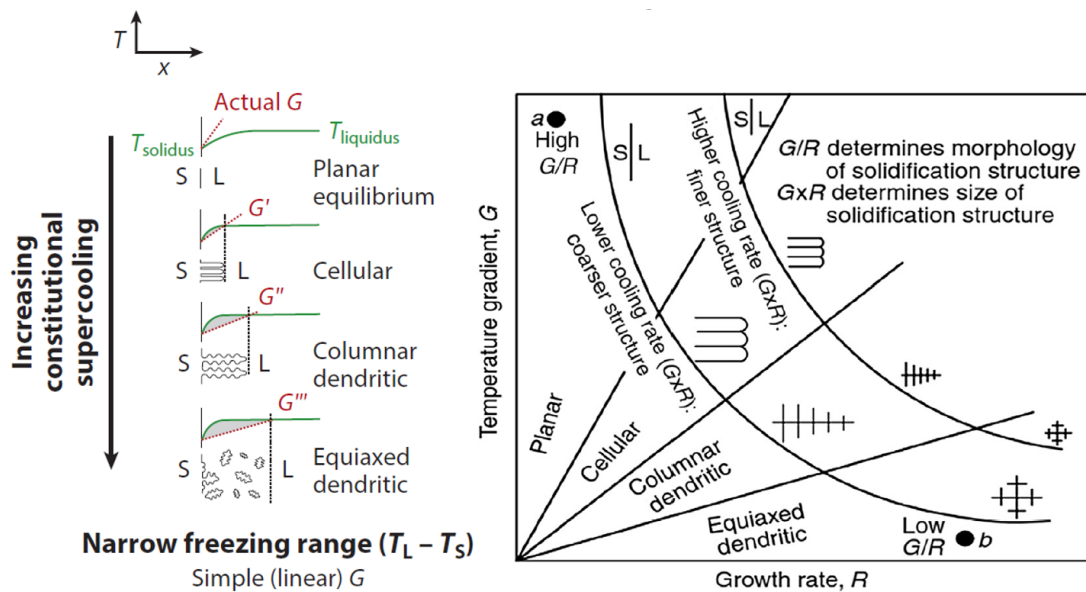


Figure 11: Schematic overview of solidification modes with respect to the thermal gradients and undercooling [8, 9].

2.2.4 Phases and precipitates

The mechanical properties of the material depend not only on the grain size and orientation but also on the phase and precipitate distribution [38]. IN718 phase transformation during the L-PBF process of liquid metal to solid is important since the strength of the material relies on the hardening precipitates γ' and γ'' as already discussed in Section 2.1. T. DebRoy et al. stated that γ' does not develop readily in the L-PBF manufacturing process, so thermal post-processing is needed [46]. This is the reason why the hardness of non-heat-treated parts is typically lower [11]. Table 3 shows different obtained phases with different heat treatments.

Table 3: Microstructure of IN718 obtained after AS: as-built, ST: solution treatment and DA: double ageing.

Alloy	Process	Condition	Microstructure	Refs
IN718	L-PBF	AS	Laves phase in interdendritic region of γ -matrix	[29]
		ST (980 °C/1h/AC)	δ + Laves phase in γ -matrix	[47]
		DA (720 °C/8h/FC, 620 °C/8 h/AC)	γ' + γ'' , δ + Laves phase in γ -matrix	[46]

2.3 Process conditions during additive manufacturing

This section describes the influence of the process parameters, the support structure, build orientation and build height on the microstructure and mechanical properties.

2.3.1 Process parameters

Different studies investigated the influence of the process parameters on the microstructure of the L-PBF process. The studies showed that the microstructure can be controlled in AM by varying the process parameters. V.A. Popovich et al. observed with lower laser power (250W) much finer equiaxed grained microstructure compared to higher laser power (950W) by using the same VED [38]. Higher laser power has more energy applied which leads to more extensive and deeper melt pool and shows coarse microstructure with large columnar grains parallel to the build direction because of the heat flow (conduction) through the previous layers. Also, a higher fraction of Laves phase was found by using higher laser power, which is undesirable, as explained in Section 2.1. The number of precipitates did not show a significant difference between the used laser powers. The hardness of the coarse grains (950W) showed around the 20 % lower hardness, YS and UTS. The larger columnar grains in pull direction were probably the reason for the difference of the YS and UTS in the 950W samples. The higher hardness observed with lower laser power can be related to the finer-grained regions. Besides that, it is also stated that an increase in porosity and undesirable Laves phase play a role in reducing the mechanical properties [38].

X. Wang et al. concluded that an increased scanning speed increases the thermal gradient and the cooling rate which lead to smaller columnar grains (finer microstructure) and higher strength of the parts. Higher scanning speed gives smaller columnar grains but at a certain point, the columnar grains will not reduce further [48]. X. Wang et al. also concluded that average hardness on the z-plane is higher than the x-plane since the z-plane has homogeneous microstructure and the grains are smaller than the side surfaces. Smaller grains lead to higher hardness according to Hall-Petch relation.

A.A. Popovich investigated the influence of the layer thickness on the microstructure and mechanical properties of IN718 bulk material [49]. Higher layer thickness (30, 50, 100 μm) produces larger grains sizes (0.7–0.9, 0.9–1.1 and 1.3–2.0 μm , respectively) by using the same VED. There was no predominant orientation of the equiaxed grains shown at a layer thickness of 50 μm , while the sample with a layer thickness of 100 μm had columnar grains with predominant orientation parallel to the build direction. The layer thickness also influenced the strength of the specimens (YS and UTS) at room temperature and elevated temperatures. Higher strength was obtained at lower layer thickness attributed to smaller grains. The applied heat treatment (hot isostatic pressing, solution annealing and ageing) improved the YS and UTS of the specimens, while the elongation decreased.

2.3.2 Support structure

H. Song et al. manufactured cubes on the build plate and the support structure with 5 mm height and investigated the effect on the microstructure [50]. The supported geometry with an area fraction of 37 % showed a higher heat built-up after laser exposure (487 K versus 353 K without support), slightly lower cooling rate and a slightly longer time spent at high temperature. The theoretical calculation of the solidification cooling rate with and without support was $8.45 \cdot 10^5$ and $6.57 \cdot 10^5$ K/s, respectively. However, in both cases, the solidification cooling rate was calculated with the thermal conductivity of solid IN718 material, while support structure with an area fraction of 37 % has lower thermal conductivity than solid material. The lower thermal conductivity was not taken into account. Higher area fraction of the support structure or lower support height leads to more heat conduction through the support structure, so the closer the microstructure and mechanical properties are, compared to the bulk material. They concluded that slightly lower heat conduction through the support structure did not result in mayor microstructural changes. The average micro-hardness with support showed slightly lower hardness of 301 against 316 HV without support. The surface roughness between the support and without support structure was not compared.

2.3.3 Build orientation

This section discusses how the build inclination angle influences the microstructure and mechanical properties. D. Du et al. investigated the effect of the build angle on the microstructure, mechanical properties and corrosion resistance of IN718 samples produced by L-PBF [10]. The results revealed that with an increasing inclination angle, the angle between the sample and the build direction, as shown in Figure 12, the fraction of Laves phase increased in the samples, see Figure 13. The main reason

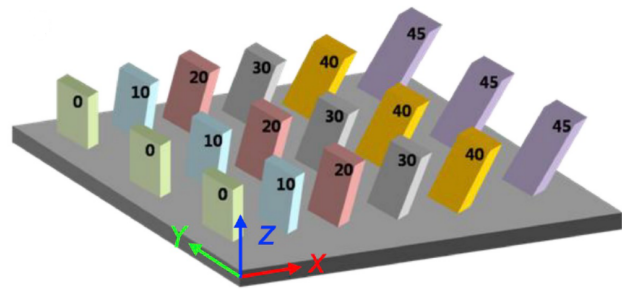


Figure 12: Schematic representation of the manufactured samples with different inclination angles between the specimens and the build direction [10].

is that the thermal gradient in the melt pool during solidification decreased, because the heat transfer dissipation decreased with an increasing inclination angle since powder particles have a lower thermal conductivity than solid material [10, 16]. As mentioned earlier, it is known that the Laves phase decreases the mechanical properties. However, the UTS and YS of the L-PBF parts increased with an increasing inclination angle (tested up to 45 degrees), but elongation remained relatively unchanged. Du et al. concluded that the crystallographic orientation, the orientation of the $\{111\}110$ preferential slip system for FCC, is an important factor for improving mechanical strength [10]. G.E. Bean et al. also found superior mechanical properties at room temperature of IN718 specimens with solution treatment at 955°C for 1 hour and precipitation heat treatment at 720°C for 8 hours and 620°C for 18 hours [23]. The results are shown in Table 4. The 45-degrees specimens showed the highest YS, UTS and elastic modules and the vertical sample showed the lowest properties but the highest elongation.

Table 4: Mechanical properties at room temperature of L-PBF IN718 specimens with solution and precipitation heat treatment [23].

Specimen orientation	YS (MPa)	UTS (MPa)	Elastic modules (GPa)	Elongation (%)
Vertical	1034 ± 1.4	1365 ± 1.4	193.8 ± 3.4	28.7 ± 0.2
Angled (B + 45)	1062 ± 1.4	1407 ± 4.1	206.9 ± 1.2	24.7 ± 0.4
Horizontal	1055 ± 2.1	1407 ± 2.1	201.4 ± 3.2	21.6 ± 0.5

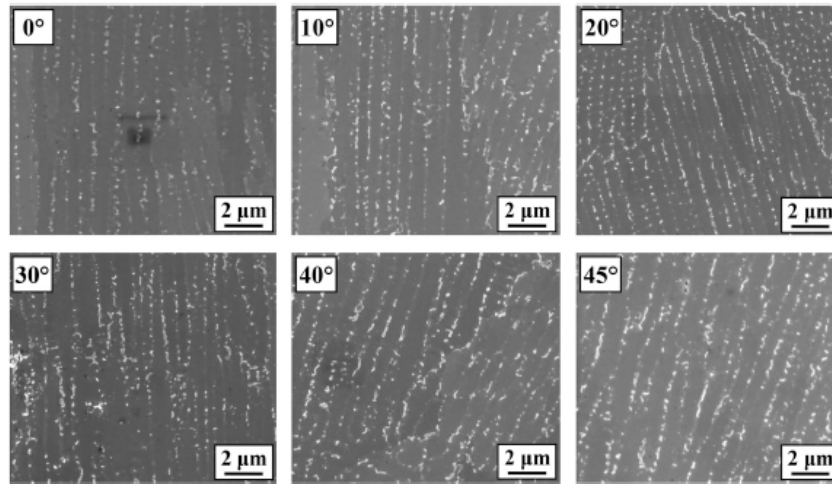


Figure 13: Scanning electron microscope images showing the Laves phase obtained at different inclination angle [10].

Ni et al. observed differences in mechanical properties in different directions (anisotropy) of L-PBF IN718 samples [7]. The samples build direction and scanning strategy are shown in Figure 14. They found that the longitudinal samples, parallel to the vertical building direction indicated with *A*, showed a lower UTS and YS than the transverse samples, perpendicular to the vertical building direction indicated with *B*, of 1101 MPa and 710 MPa versus 1167 MPa and 850 MPa, respectively. Although, the longitudinal samples showed a higher elongation (24.5%) compared to the transverse samples (21.5%). J. Strössner also found anisotropy behaviour of the horizontal direction compared to the vertical build direction [51]. The anisotropy in strength and ductility was attributed to the fibre texture of columnar grains (parallel to the build direction) which led to high strength in the transverse direction. The columnar grain boundaries also served as a path along which damage can preferentially accumulate, leading to earlier fracture and thus lower ductility, according to Ni et al. [7].

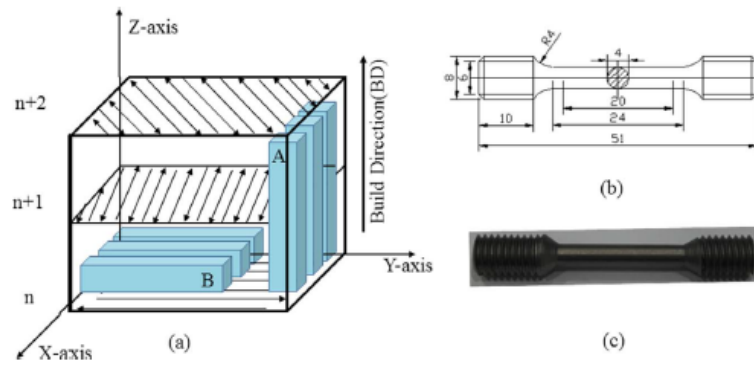


Figure 14: (a) The used laser scanning strategy and build direction of the samples. (b) The tensile samples. (c) The tensile sample after machining [7].

2.3.4 Build height

The build height can also influence the microstructure of L-PBF parts. X. Wang et al. investigated the effect of the build height on the microstructure of IN718 samples produced by L-PBF [52]. The micrographs revealed that the vertical y-plane had a columnar grain structure due to the downward-facing heat flux into the substrate. The z-plane (parallel to the build plate) had an equiaxed grain structure due to the horizontal heat flux related to the movement of the heat source [7, 52]. The width of these columnar grains on the y-plane was different along the build height, which was caused by different cooling rates. The manufactured part's highest width of a single grain was found in the middle ($146.77\mu\text{m}$) and the lowest width was found in the bottom ($74.92\mu\text{m}$). They stated that the width differences were caused by the larger cooling rates in the bottom of the build directly connected to the build plate and had a much lower temperature than the IN718 melt pool. Higher cooling rates near the build plate as compared to the top layers were also noted by A. Mostafa et al. [5]. So, increasing the cooling rate will form smaller columnar grains, according to J. Gockel et al. [43]. The top layers also showed columnar grains with a lower width compared to the middle of the build namely $112.45\mu\text{m}$ and $146.77\mu\text{m}$, respectively. The reason for this was that the top layers of the build were in closer contact with the environmental temperature of the build chamber, leading to high cooling rates [52]. However, these large differences were not found by other papers and normally conduction is predominant compared to convection [53], so their reasoning seems a bit doubtful.

The hardness in the bottom was the highest, which was related to finer grains size and the hardness decreased with an increasing build height and increased again to the top of the sample [52]. Finer grains size leads to higher strength of the material according to the Hall-Petch relation. The reheating of previous layers could cause softening of previous layers and such influence to the middle layers was most evident, according to Wang et al. [52]. No significant difference in anisotropy was found between the side and the top surface of the parts according to the texture analysis. A trend in the decreasing hardness from the bottom to the top was also found by S. Sun et al. using electron beam melting (EBM) [11], see Figure 15.

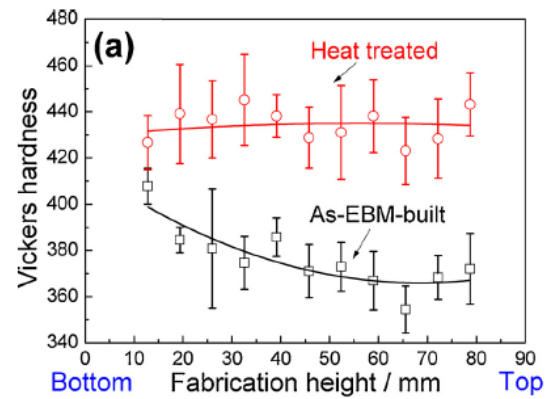


Figure 15: Hardness variations along the build height in the as-EBM-built and heat-treated state for longitudinal samples [11].

2.4 Porosity

The porosity development primarily depends on the size and shape of the melt pool, which is influenced by the LED. Small melt pool sizes (depth and width) are obtained with lower LED values and increase the processing time. Large melt pool sizes decrease the manufacturing time, but the overall porosity can increase by vaporisation of the powder or substrate leading to the formation of pores [54, 55]. J.P. Oliveira et al. summarised the influence of the laser power and scanning velocity on the porosity, see Figure 16 [2]. Lack of fusion is observed at high laser speed and lower power regime, keyhole porosity at high power and low velocity and balling at high power and high velocity. L. Scime obtained a similar graph [6].

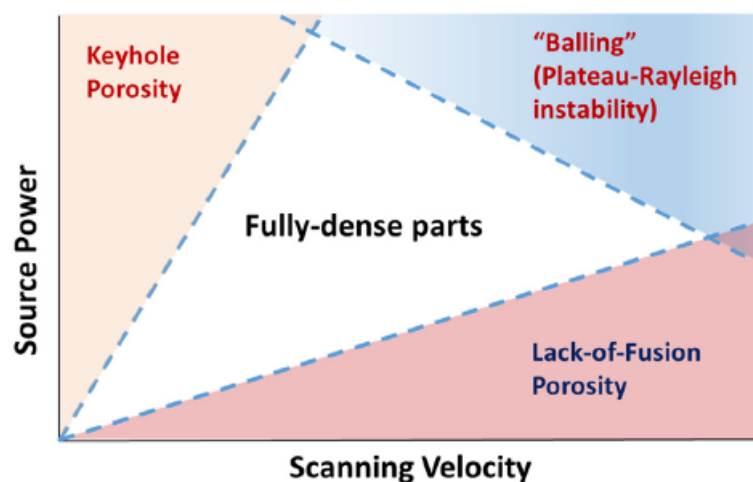


Figure 16: The influences of the laser power and scanning speed on the porosity [2].

Q. Jia et al. found higher porosity at lower LED value (180 J/mm) because of the observed balling phenomenon and open pore structure compared to higher LED value (330 J/m), which increased the density of the manufactured parts [56]. A reduction of porosity by an increasing VED value was also found by [57–59]. The balling phenomenon is characterized by groups of powder particles that break off during melting and solidify into a spherical shape along the surface of the scanning line [60]. This leads to a lower density and poor surface finish due to the formed spherical beads. At higher scanning speeds the dwelling time is shorter, which gives a lower melt pool temperature. A lower melt pool temperature has higher dynamics viscosity and hinders the proper distribution of the molten metal, leading to open pores. However, S. Sun et al. stated that too low dynamic viscosity could also lead to balling phenomena (overheating of powder), so a balance has to be found in the dynamic viscosity of the melt pool [42]. Overheating the melt pool causes sputtering, and the intensity grows with an increase in LED. Non-melted powder particles and liquid droplets around the melt pool are expelled by the recoil pressure generated on the melt pool as the result of the melt evaporating, according to S. Sun [42]. The sputtering particles are generally spherical and larger than the feed powder particles. The sputtered non-melted particles are also known as satellites.

Tillmann et al. observed the presence of argon at a small concentration of 0.3 ppm entrapped in spherical pores within manufactured IN718 samples. The gas could be entrapped in the embedded powder particles or during the L-PBF process [61]. Entrapment of argon gas in the pores can have

a significant influence on the mechanical properties. The argon gas can lead to internal stresses and acceleration of crack formation for high-temperature application. A vacuum build chamber can be a solution to reduce the entrapment of gas.

The size (depth and width) of the melt pool is from great importance to avoid non-melted powder particles (lack of fusion) in the final part, see Figure 17. No lack of fusion is achieved by fully melting the material that can be achieved by a complete overlap of the melt pools. Figure 17 shows the minimum depth of overlap M_d^o , which is affected by the hatch distance and it dictates the maximum layer thickness [2]. The layer thickness must be smaller than M_d^o to ensure no lack of fusion. The minimum depth of overlap M_d^o can be increased with a shorter hatch distance and deeper melt pools.

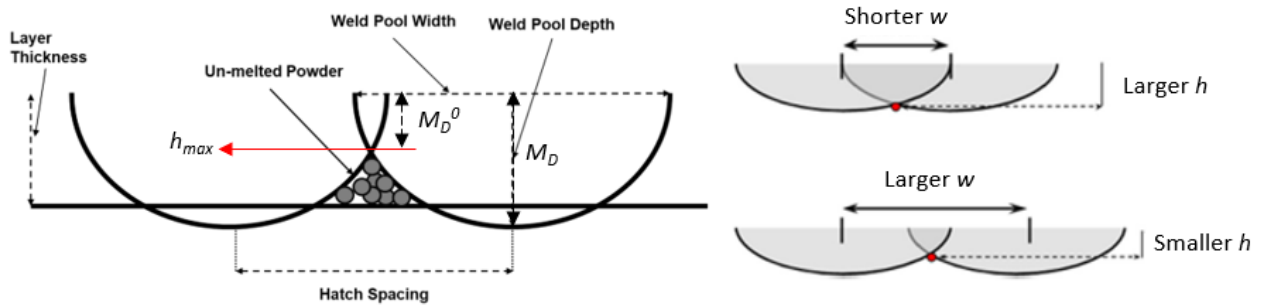


Figure 17: M_d^o is the minimum layer thickness required to obtain full fusion and M_d is the depth of the melt pool. M_d^o is dependent on the coupled parameters hatch distance (w) and layer thickness (h) given a constant melt pool size [2].

2.5 Surface conditions

The surface roughness and surface defects are an important factor for the fatigue behaviour since they are the primary factor of influence of the crack initiation and crack propagation process [62]. One of the challenges introduced for the surface finish of the manufactured part is the staircase error in the STL file, see Figure 18. The layer thickness should be infinitely small to solve this problem so that the STL file representation error is negligible. However, this is not feasible, so this effect will always play a role in the surface conditions, mainly in the z-direction, for L-PBF parts. Another challenge increasing the surface roughness is the powder particles on the surface of the final part which can be attributed to the combination of two factors: The sintering of the surrounding powder particles on the surface of the melt tracks and the sputtering of powder particles caused by overheated melt pools [63], as described in Section 2.4.

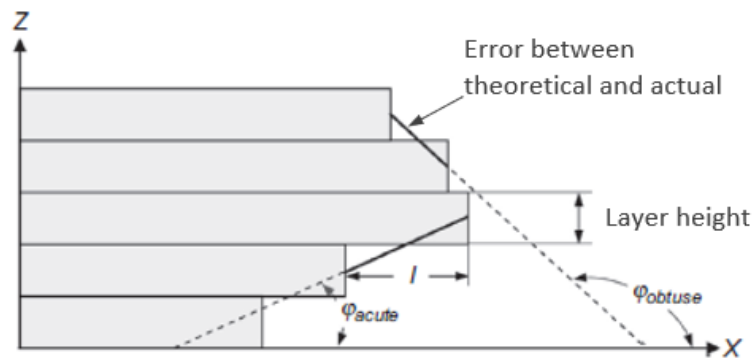


Figure 18: Layer approximation of the CAD geometry which results in the staircase error [12].

The inclination angle of overhangs also influences the surface roughness. I. Koutiri et al.[63] found that the down-skin surface of an inclination angle (tested up to 35° between the build direction and the specimen) had a higher surface roughness than the upper surface of the incline angle which was also observed by M. Leary [12] and A. Triantaphyllou [64]. The rationale for this observation is that the inclined specimens are supported by powder which has lower thermal conductivity than solid-supported zones [12]. The lower thermal conductivity causes elevated temperatures, leading to larger melt pool sizes. The melt pool sinks into the powder, due to gravity and capillary force, and the powder particles close to the melt pool are sintered to the down-skin surface [65].

The up-skin surface roughness values for specimens manufactured under an inclination angle of 10° and 35° were between 6 and $11 \mu\text{m}$ and seemed to decrease with the laser power (heat input) from 100 to 180 W. The power increased the melt pool's size, which allowed a better remelting of the previous layers and decreased the quantity of agglomerated powder so also the surface roughness. However, the specimens with 35° inclination angle showed higher up-skin surface roughness at 180 W because of the lower heat dissipation, indicating that support structures were needed to increase the heat dissipation. At the same time, support structures also increase the down-skin surface roughness after removing them which can be seen in Figure 19 on side 4 of the 0° specimen [66]. In this figure, the average surface roughness is given on four different sides of three specimens where the 60° sample shows the lowest surface roughness. The results also show higher roughness on the down skin compared to the upper skin. No large differences were found between the top surface and side surface.

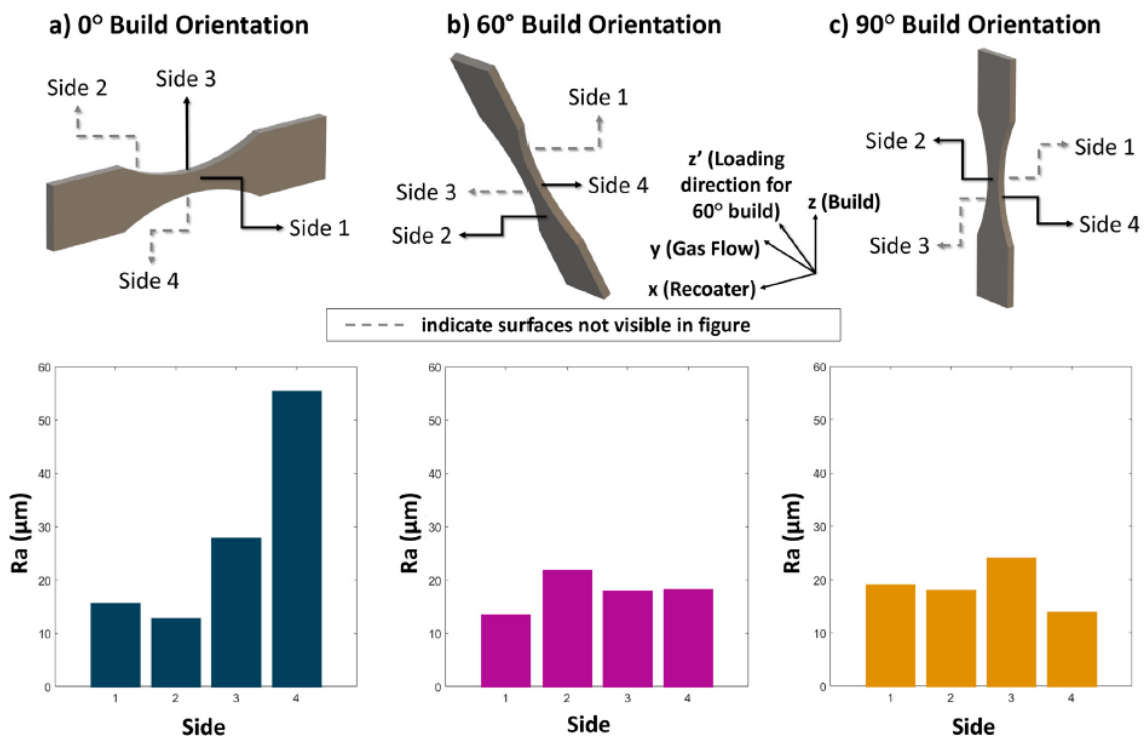


Figure 19: R_a values for different build angles a) 0° build orientation (flat) with support structures under side 4, b) 60° build orientation, and c) 90° build orientation (vertical).

The influence of the contour scan on the surface roughness was also studied by I. Koutiri et al. [63]. An increase of beam diameter at a constant laser power of 400 W increased the surface roughness. Higher volumetric energy density contour lines showed a decrease in average surface roughness (R_a). Contour lines are the outer lines that follow the contour of the part aiming for a smoother surface finish.

The R_a is the arithmetic mean deviation from a surface profile or in other words, the average surface roughness. The laser scan speed influences the melt pool at which low speeds encourage turbulent pools that result in deteriorate surface finish because the amount of agglomerated particles that spatter on the build surface becomes more significant. I. Koutiri et al. concluded that the correlation between surface roughness and the process parameters (that determine the VED) is a challenging task. Globally, the surface roughness decreased with higher laser power and increased with lower scanning speeds and with larger inclination angles [63].

Solberg et al. manufactured specimens for quasi-static and fatigues loading (notched and unnotched) where the notched specimens showed a larger difference of the up and down-skin surface [67]. The down-skin has a significantly higher roughness than the up-skin surface and sharp features with substrate defects are arose after $2 \cdot 10^6$ fatigue loading cycles. The upper skin's surface roughness was much smaller than the down skin roughness, $77 \mu m$ and $259 \mu m$, respectively.

2.6 Conclusions

Multiple papers discussed the influence of the process conditions (process parameters and build orientation) on the microstructure, mechanical properties, surface roughness and porosity. However, these results were found in relatively simple geometries and were not directly available for complex-shaped parts. The features of simple geometries still have room for improvement, such as the surface roughness on down-skin surfaces, which was relatively high compared to horizontal and vertical surfaces. The complex part of Aeronamic mainly consists of bulky regions, thin walls, overhangs and support structures. The papers that analysed complex parts with these features were mainly focused on the distortion of the part and that was out of this project's scope. So, the results discussed in this literature review can be utilised as a basis to analyse the complex part. However, more research is needed to investigate the relation between the microstructure and (mechanical) property in each feature of the specific aerospace part examined in this research.

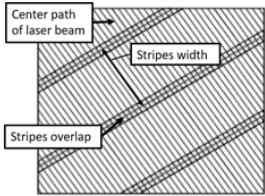
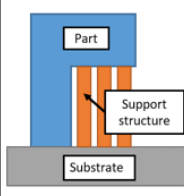
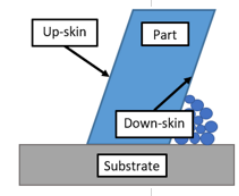
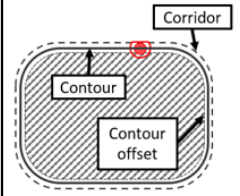
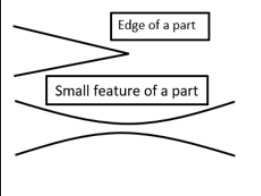
3 Experimental procedures

This chapter describes step by step the experimental procedures followed in this research. It describes the equipment used in this research and the approaches for measuring material related properties. The topics are arranged in the order of the procedures applied in this research.

3.1 Additive manufacturing machine and process parameters

The inlet housing part examined in this research was manufactured by an EOS M290 L-PBF machine. The AM machine has a building volume of $250\text{ mm} \times 250\text{ mm} \times 325\text{ mm}$ and uses a fibre laser of 400 W with high-speed scanner mirror to deflect the laser. The mirror is placed above and in the centre of the build plate (also called the substrate). The recoater used to distribute powder particles is made from high-speed steel. The part was manufactured on a $250\text{ mm} \times 250\text{ mm} \times 35\text{ mm}$ build-plate of the material C45 and the build plate was kept at $80\text{ }^\circ\text{C}$. The inlet housing part was manufactured in an argon atmosphere (0.75 mbar differential pressure over the build plate) with mono-parameters' settings based on the density results from the research of the Fraunhofer Project Center at the University of Twente [68]. Mono-parameters' settings mean that the laser scanning lines at each layer have the same process parameters, see Table 5. However, there were five different settings related to the manufacturing of the part, which were stripes (infill part), infill support, down-skin, contour and edge. The stripes setting was used to scan the infill of the part and the infill support setting was used to build the support structure. The laser scanning direction of the infill of the part was rotated 67° after each build layer. The contour laser setting was used to scan the samples' outer contour, aiming for a better surface finish and dimensional accuracy. The down-skin laser setting was used on regions that did not include any solid material under it (only powder particles) and the edge laser setting was used for sharp angles or small features, see Table 5. Detailed pictures of the manufactured inlet housing part are depicted in Appendix A.

Table 5: Process parameters used to manufacture the inlet housing part with the EOS M290 L-PBF machine using IN718 powder particles.

Infill (part)		Infill (block support)		Down-skin		Contour		Edge	
Scanning	Stripes	Unidirectional		Scanning	x	Scanning	x	Scanning	x
Laser power (W)	285	300		Laser power (W)	95	Laser power (W)	138	Laser power (W)	100
Laser speed (mm/s)	Confidential	Confidential		Laser speed (mm/s)	Confidential	Laser speed (mm/s)	Confidential	Laser speed (mm/s)	Confidential
Layer height (mm)	0.04	0.08		Layer height (mm)	0.04	Layer height (mm)	0.04	Layer height (mm)	0.04
Hatch distance (mm/s)	0.11			Hatch distance (mm/s)	0.1	Contour offset (mm)	0.012		
Stripe width (mm)	10			Up skin thickness (layers)	3	Thickness (Layers)	1		
Stripes overlap (mm)	0.12			Hatch sorting	Straight lined	Corridor (mm)	0.07		
Pattern	67° Shifted			Pattern	No pattern	Pattern	No pattern		
									

3.2 Powder characteristics

The fresh IN718 powder particles were produced by gas atomisation (GA) and obtained from the supplier PraxAir. The IN718 powder was multiple times reused before utilised to manufacturing the inlet housing part. The chemical composition of the powder particles is shown in Table 6 and is according

to the IN718 material specifications, see Table 2. The powder size distribution of non-reused powder particles was measured by PraxAir and had a D10, D50 and D90 of 17.8, 27.8 and 40.8 μm , respectively. D10 means that 10 % of the total amount of powder particles has a diameter smaller than 17.8 μm . Something similar applies to D50 and D90. The size distribution of approximately 10 times reused powder particles was also measured and revealed slightly higher D10, D50 and D90 of 19.2, 29.1 and 42.1 μm , respectively. The powder size distribution graph of reused powder is shown in Figure 20. In this figure, the red line indicates which particles' sizes are present in what proportions (percentage) from the measured particles group. The blue line indicates the sum of the percentages of the powder particle sizes where the total amount of measured powder particles is 100 %.

Table 6: Composition of fresh IN718 powder, utilised for manufacturing the inlet housing part, obtained from the supplier PraxAir.

Chemistry	Results (wt%)
Nickel (Ni)	53.24
Iron (Fe)	18.16
Chromium (Cr)	18.74
Copper (Cu)	0.03
Molybdenum (Mo)	3.07
Niobium (Nb)	5.13
Carbon (C)	0.03
Magnesium (Mn)	0.00
Phosphorus (P)	0.006
Sulfur (S)	0.001
Silicon (Si)	0.06
Titanium (Ti)	0.94
Aluminium (Al)	0.44
Cobalt (Co)	0.15
Boron (B)	0.002

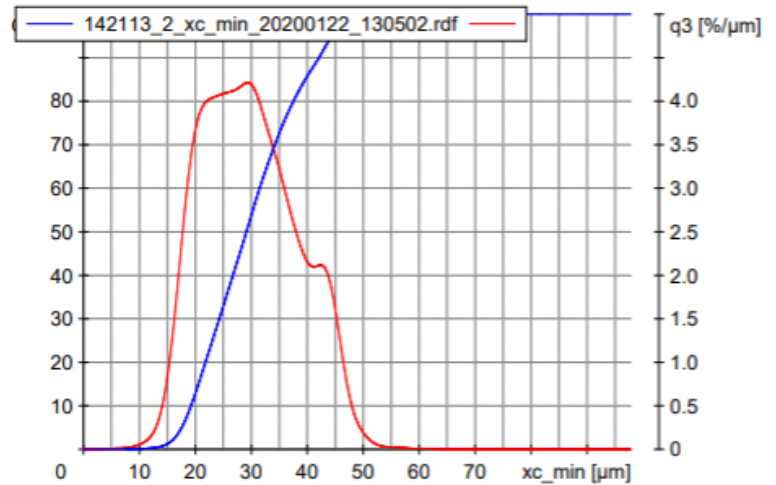


Figure 20: Powder size distribution graph of approximately 10 times reused IN718 powder particles.

3.3 In-process monitoring systems

The manufacturing machine was equipped with two in-process monitoring systems. The function and working principle of these systems are explained in the following two sections.

3.3.1 Optical Tomography system

The EOS M290 L-PBF machine was equipped with an EOSTATE Exposure Optical Tomography (OT) system to capture the emitted thermal radiation of each layer during the manufacturing process, see Figure 21. A high-resolution scientific Complementary Metal–Oxide–Semiconductor (sCMOS) camera monitored at 10 frames per second the thermal radiation of the complete build platform near-infrared range. Multiple images were obtained per build layer and the thermal radiation intensity of each corresponding pixel was summed and integrated into one picture after each build layer [13]. The final image provided data of the homogeneity and stability behaviour of the build process at each layer throughout the AM process. Image processing between the captured images and the converting process into one image was performed to reduce the noise. The output value of the camera was a mean grey value and

it was converted into a multi-coloured image using a colourbar with an upper and lower limit.

Figure 22 shows the three main components of the emitted radiation during the manufacturing process. The manufacturing process is observed best by measuring the emitted thermal radiation, which is directly dependent on the melt pool properties, according to G. Zenzinger et al. [13]. So, the captured thermal radiation must avoid the emitted radiation of other emissions shown in Figure 22. Therefore, the sCMOS camera captured the emitted radiation of 900 nm wavelength with plus-minus 12.5 nm tolerance by using a suitable band-pass filter. This wavelength is higher than the visible wavelength of the human eye (380-780 nm) and the emission that occurs during the manufacturing process which is between 400-600 nm according to literature [13]. These emissions are caused due to the laser's high energy density at the focal point, which causes vaporization and ionization gasses due to the high temperatures [13]. The captured wavelength of the camera is lower than the reflected laser wavelength of 1064 nm. So, these emissions should not have an influence on the measured thermal radiation of the melt pool.

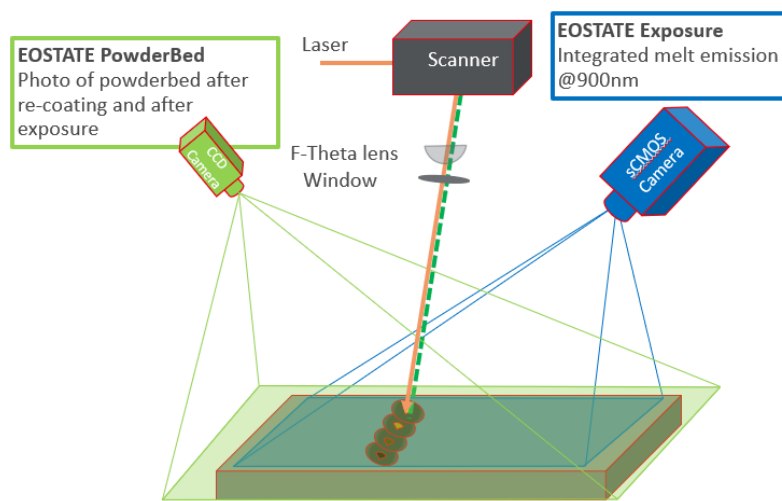


Figure 21: EOS M290 L-PBF machine setup showing the laser heating the powder, the sCMOS camera capturing the OT images during manufacturing process and the EOSTATE PowderBed camera capturing images before and after a recoater cycle [13].

The field view of the camera corresponds with the build platform dimension of the AM machine, see Figure 21. Each picture has 2000 by 2000 pixels on an area of 250 mm x 250 mm which corresponds to a resolution of 0.125 mm² per pixel, approximately. These OT-images can be used as process monitoring to detect causes of defects within the additive-manufactured part. In this research, the OT images were used to establish relationships between the OT images and defects found within the complex part.

The OT images of every layer of the inlet housing part examined in this research were not available. Only a few images could be extracted with the raw data graph of the sCMOS camera. For this reason, the available images of an older version of the examined part were used. This older inlet housing version was given the following name: 1-2018-121.

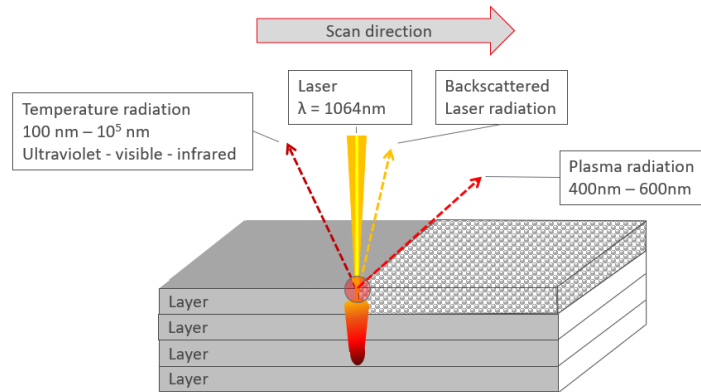


Figure 22: Emitted radiation during the L-PBF process [13].

3.3.2 PowderBed system

The EOS M290 L-PBF machine was also equipped with an EOSTATE PowderBed monitoring system which monitored the powder distribution over the build chamber during the manufacturing process. An image of the build chamber was taken after a re-coating cycle and after exposure of the laser. This method detects recoater problems and can also be used for analyzing causes for recoater crashes. In this research, the powder bed images were used to examine the powder distribution on specific layers to obtain more information about defects (i.e. porosity). The PowderBed system images of the examined inlet housing part (1-2019-062) were available and used in this research.

3.4 Cutting plan

The inlet housing part manufactured by Aeronamic was analysed on density, surface roughness, microstructure and microhardness. To do so, the part was cut into smaller pieces to make it more manageable. The cutting plan is described in detail below:

- The part was removed from the build plate using a band saw with the support structures still attached to the part.
- The first cut was precisely in the middle of the part, to obtain two symmetrical pieces, by using a band saw with a cutting speed of 20-25 *m/min*, see Figure 23. Intense liquid cooling was used to avoid changes in the material's microstructure. The two symmetrical cross-sectional surfaces, obtained from the first cutting line, were used for microstructural and microhardness analyses, respectively.
- The second and third cut were done to obtain two slices of the part and the height was kept lower than 20 *mm*. After embedding the first sample, it became clear the 20 *mm* height led to instability and the sample fell over due to the pressure applied by the embedding machine. Special springs used to keep the specimens in the right orientation did not work. For this reason, the samples were cut in half to decrease the height and increase the stability of the samples.
- The slices were cut into smaller samples by a Struers Discotom-100/-10 cutting machine in ascending order of the cutting lines according to Figure 24.

The bottom half of the part was heat-treated and indicated with the abbreviation HT, see Figure 24. Note, the numbers of the as-built and heat-treated samples corresponds to the same cross-section.

The bottom side is mirrored as compared to the top, which can be seen by the direction reversal of the y-coordinate.

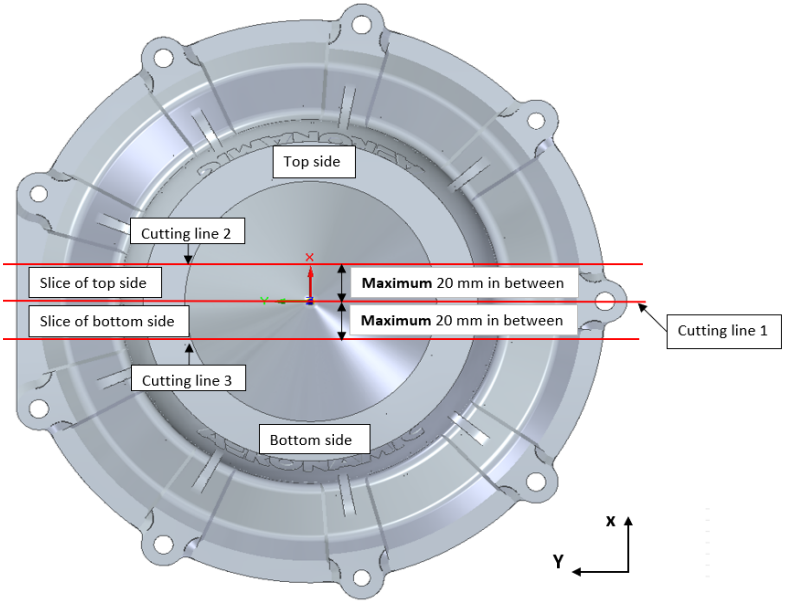


Figure 23: Top view of the inlet housing part showing the first three cutting lines.

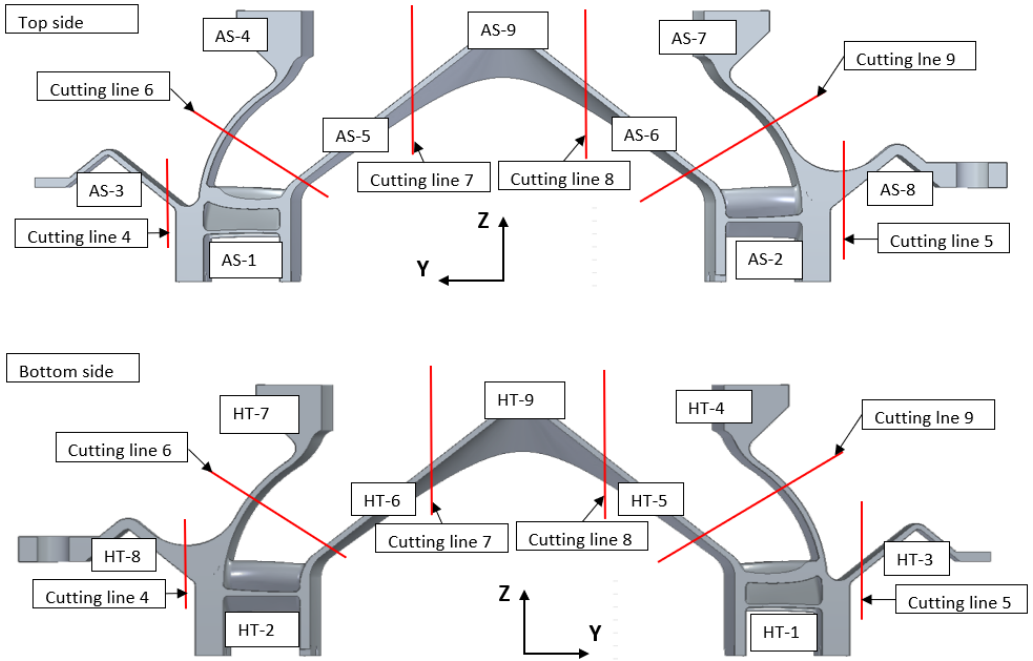


Figure 24: Overview of cutting lines to obtain a series of samples for further analysis. The top side numbers correspond to the same cross-section of the number of the bottom side due to the direction reversal of the y-coordinate.

3.4.1 Labelling system

This section describes the labelling system used in this research. The labelling system ensures the results, obtained from the (embedded) samples, can be traced back to the correct manufacturing job. Figure 25 shows the method used to label the experimental research results. The first position indicates which

aerospace part from Aeronamic was used in this research. In this report, only one inlet housing part was examined (indicated with number one) while some OT images were acquired from an older version (indicated with number two), see Chapter 4.2. The second position specifies the year in which the part was manufactured. The third position is the manufacturing sequence number of the manufacturing job given by Aeronamic. The fourth position indicates if the sample is in as-built or heat-treated state and the last position provides the actual number of the samples, see Figure 24. Therefore, the following first three characters were used for the inlet housing part examined in this research: 1-2019-062. The last two positions give the actual number of the samples, shown in Figure 24.

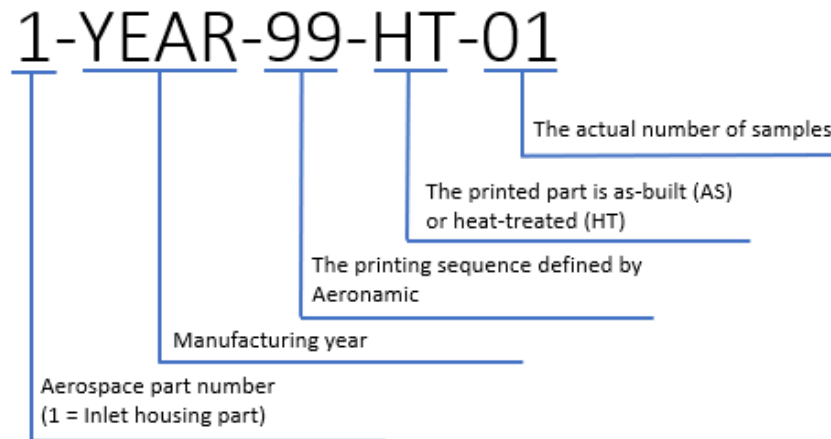


Figure 25: Sample labelling system used in this research.

3.5 Heat treatment

To study the influence of the solution and precipitation heat treatment on the microstructure characteristics and (mechanical) properties, half of the part was heat-treated (bottom side), as shown in Figure 24. The heat treatment used in this research was performed according to AMS2774 standard, using a Carbolite Gero CWF 1200 furnace [14]. First, a solution heat treatment was applied at 1066 °C for 1 hour and the samples were air-cooled to room temperature afterwards, see Figure 26. Subsequently, a precipitation heat treatment was done at a temperature of 718 °C for 8 hours, followed by furnace cooling to 621 °C and an additional ageing time of 18 hours and air-cooling afterwards. The heat treatment was carried out in an argon atmosphere, but the presence of oxygen was not excluded due to a leakage of the furnace, probably.

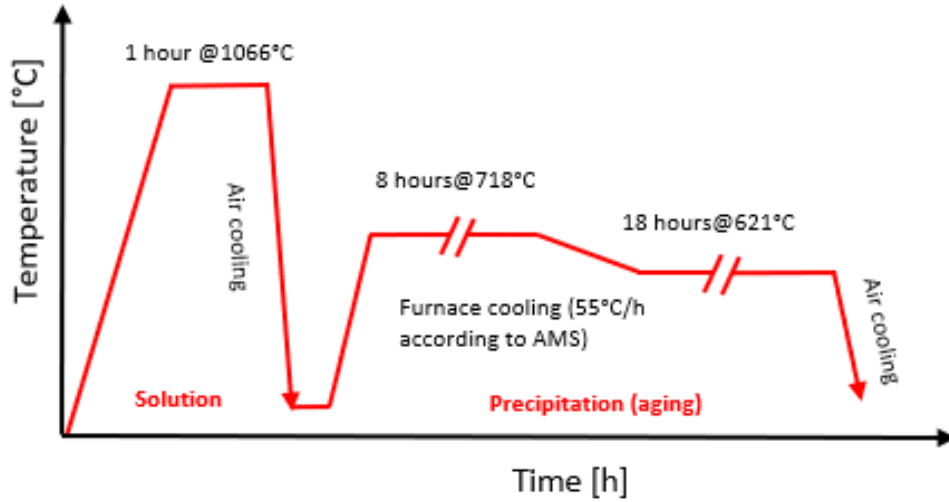


Figure 26: Graph showing the time-temperature curve of the solution and precipitation heat treatment applied on the IN718 samples [14].

3.6 Density measurements

The samples were ultrasonically cleaned, prior to the density measurements, with an Elmasonic S machine for 2 minutes at room temperature submerged in isopropanol. The density measurements were executed according to the ASMT B311 standard [69]. The density of the samples was calculated based on Archimedes principle. A body immersed in liquid, with a known density, indicates an apparent weight loss corresponding to the weight of the liquid it displaces [70]. In other words, the differences in weight in air and emerged in a liquid, is the weight of the fluid that is displaced by the object. So, the object was first weighed in air and afterwards weighted in water. A wetting agent was added to reduce the effect of surface tension of the water with a volume percentage of 0.05 to 0.1 %. The effects of the surface roughness and porosity that was open to the outside world were neglected. By knowing the density of the water, the density of the samples was calculated by the following equation:

$$D = m_A / \frac{[m_A - (m_B - m_C)]}{\rho_E}, \quad (4)$$

where m_A is the mass of the test specimen weighed in air (g), m_B is the apparent mass of the specimen and specimen support in water (g), m_C is the mass of the specimen support in the water (g) and ρ_E is the density of the water (g/cm^3) [69]. The temperature of the water was measured between every sample measurement to use the correct water density. Table 1 from ASMT B311 standard was utilised to determine the density of the water [69]. By dividing m_A by $(m_A - (m_B - m_C))$ the ratio of how many times the sample in the air is heavier as compared to the fluid is obtained. By multiplying it with the density of the water, the mass of the sample is obtained.

The requirement for the density is $8.1 g/cm^3$ over the whole part, so also local areas need to be minimum $8.1 g/cm^3$. The densities of all as-built and heat-treated samples were measured to obtain a complete overview of the part density in different features. Besides that, it also indicates if there is any difference between the as-built and heat-treated samples. The KEYENCE VHX-5000 OM was used to analyse the kind of porosity present in the samples.

3.7 Microscopy

The arithmetic average surface roughness (R_a) was measured using a KEYENCE VK-9700 confocal microscope and before testing, the samples were ultrasonically cleaned with an Elmasonic S machine for 2 minutes at room temperature submerged in isopropanol. The surface roughness was calculated by measuring the roughness of each feature on three different locations with an area of $200 \mu m \times 283 \mu m$. The average value of the measurements was taken. R_a was obtained by measuring the arithmetic average deviation of the scanned profile from the centre line of the scanned profile. The following formula was used to calculate R_a :

$$R_a = \frac{1}{n} \sum_{i=1}^n |y_j|, \quad (5)$$

where n is the number of measurements and y_j is the vertical distance from the centre line to the j^{th} data point [71]. The maximum surface roughness (R_a) requirement is $3.175 \mu m$ ($125 \mu in$). The surfaces that have a lower surface roughness requirement will be polished by post-processing after manufacturing. These surfaces are the blades, the plateaus of the holes and the horizontal surface of the upper ring, see Figure 27. The surface roughness of the down and up-skin of the 45-degree overhang were measured and also the vertical and horizontal surfaces were measured to analyse if differences were present.

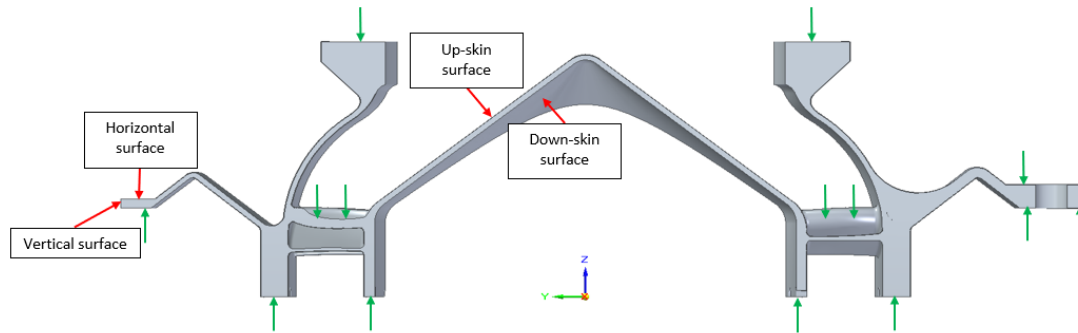


Figure 27: The green arrows indicate surfaces that generally will be post-processed and the red arrows indicate the surfaces that were measured.

All samples selected for microscopic analysis were embedded by a Struers CitoPress-5 machine. The Polyfast (bakelite with carbon filler) resin was used for embedding and the process procedure was heating at a temperature of $180 \text{ }^\circ\text{C}$ for 6.5 minutes at a pressure of 250 bar and afterwards cooling with water for 3 minutes. The samples were embedded in a disk with a diameter of 50 mm and a height of approximately 15 mm .

The grinding and polishing of the embedded samples were carried out by a Struers Tegramin-30 polishing machine. For grinding, grit sizes of 320, 500, 1000, 1500 and 2000 were used, after which polishing of 9, 3, 1 micrometer suspension and oxide polishing suspension (OP-S) were applied. The samples were cleaned with water after each step and in the end, ultrasonically cleaned with an Elmasonic S machine for 2 minutes at room temperature. After embedding Inconel 718 powder, these steps were followed: grinding with a grit size of 2000, polishing with $9 \mu m$, $1 \mu m$ and OP-S suspensions.

The samples were etched after polishing, to reveal the grain boundaries, using a 96 % volume basis of 37 % hydrochloric acid solution (HCL) and 4 % volume basis of 40 % hydrogen peroxide solution (H_2O_2). The immersion time was 6 seconds for the heat-treated and 10 seconds for the as-built samples. The samples were etched immediately after polishing since any delay in etching (exposure to air) should

be prevented because IN718 tends to oxidise instantly. The KEYENCE VHX-5000 optical microscope (OM) was used to study the microstructure of the part. The melt pools sizes were measured using the software ImageJ.

A scanning electron microscope (SEM) of model JEOL JSM-7200 was used in this research to analyse the chemical elements and study the microstructure in more detail using backscatter electrons. The crystal orientation distribution of the samples was obtained by Electron BackScatter Diffraction (EBSD) analysis integrated in the SEM microscope. This analysis technique was also used for the phase distribution measurement of the powder particles. The sample was tilted to 70 degrees, and a phosphorus screen was used to transform the backscattered electrons into a visible light signal. In the analysis of the signals from neighbouring measurement locations, a mis-orientation smaller than 10 % was considered small enough to assign the measurement locations to the same grain.

Interesting features of the inlet housing part for microstructure analyses were the bulk material at the bottom, the top, the vanes and the 45-degree overhang, see Figure 28. The heat dissipation in these different geometrical features was expected to vary, leading to change in the part's microstructure and mechanical properties. This is important to find process-microstructure-property relationships. The as-built (AS-1, AS-7 and AS-9) and heat-treated samples (HT-1, HT-4 and HT-9) were embedded, polished and etched for microstructure analysis. Optical micrographs of the polished surfaces were taken to investigate the type of porosity present in the sample. The samples were etched with hydrochloric acid and hydrogen peroxide solution, as described above, to be able to obtain the melt pool dimensions and the microstructure captured by the OM. Afterwards, microhardness measurements were performed. The samples were grinded and polished again to remove the microhardness indents. SEM analyses were performed on the bulk bottom and bulk top, the vanes and the 45-degree overhang of the thin wall structure (see Figure 28).

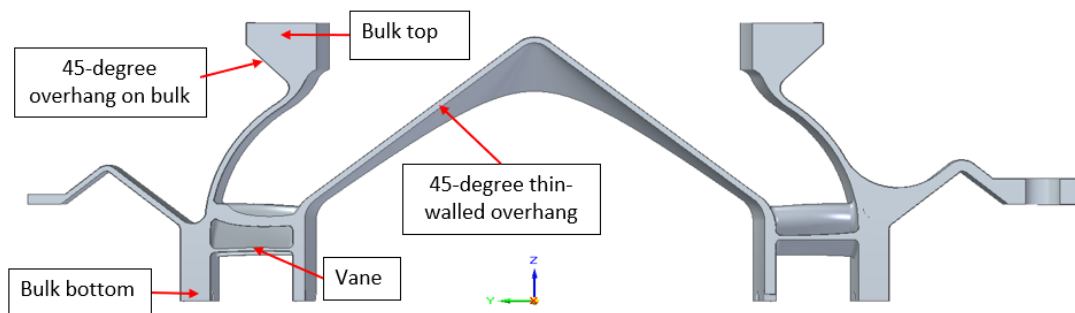


Figure 28: Features examined for microstructure analyses.

3.8 Microhardness

A Leco LM 100AT microhardness tester was used to measure the Vickers hardness of the cross-sections of the samples (y-z plane) by using a load of 500 gf and a dwelling time of 15 seconds. The tests were performed at room temperature. The microhardness was measured at four different features for both as-built and heat-treated samples (see Figure 28). On each location, 16 measurements were performed in a four by four matrix. A distance of 200 μm was used between the centre of each neighbouring indents and from the edge of the sample. This distance is minimal 3-4 times the diagonal indent diameter, so the measurements are not influenced by prior measurements according to [72]. The hardness of different features was measured on random locations and no specific points (i.e. inside melt pools or on melt pool boundaries) were selected, but pores were avoided.

4 Results

The Results chapter provides the results and some basic discussion with literature, but the main discussion is done in the Discussion chapter. This chapter aims to find process-microstructure-property relationships. The subjects are ordered in the same structure used in the Experimental chapter.

4.1 Powder characterisation

The microstructure of reused IN718 powder, utilised for manufacturing the inlet housing part, was obtained to discover the starting point of this research. The cross-section of polished non-etched IN718 powder, produced by GA, is shown in Figure 29a. The powder particles were mostly spherical, but some particles were irregular shaped. The main-sized powder particles had some small satellite particles attached to it and defects within the powder particles were also observed. A few powder particles showed gas-induced porosity inside that was entrapped during the GA production process of the powder particles. The porosity entrapped in the powder particles could be transferred to the final part. Gasses can also be entrapped in the solidified layer as a result of the turbulent nature of the fluid flow in the melt pools during the L-PBF process [5]. Gas bubbles do not have enough time to escape due to the rapid solidification in the L-PBF process [73].

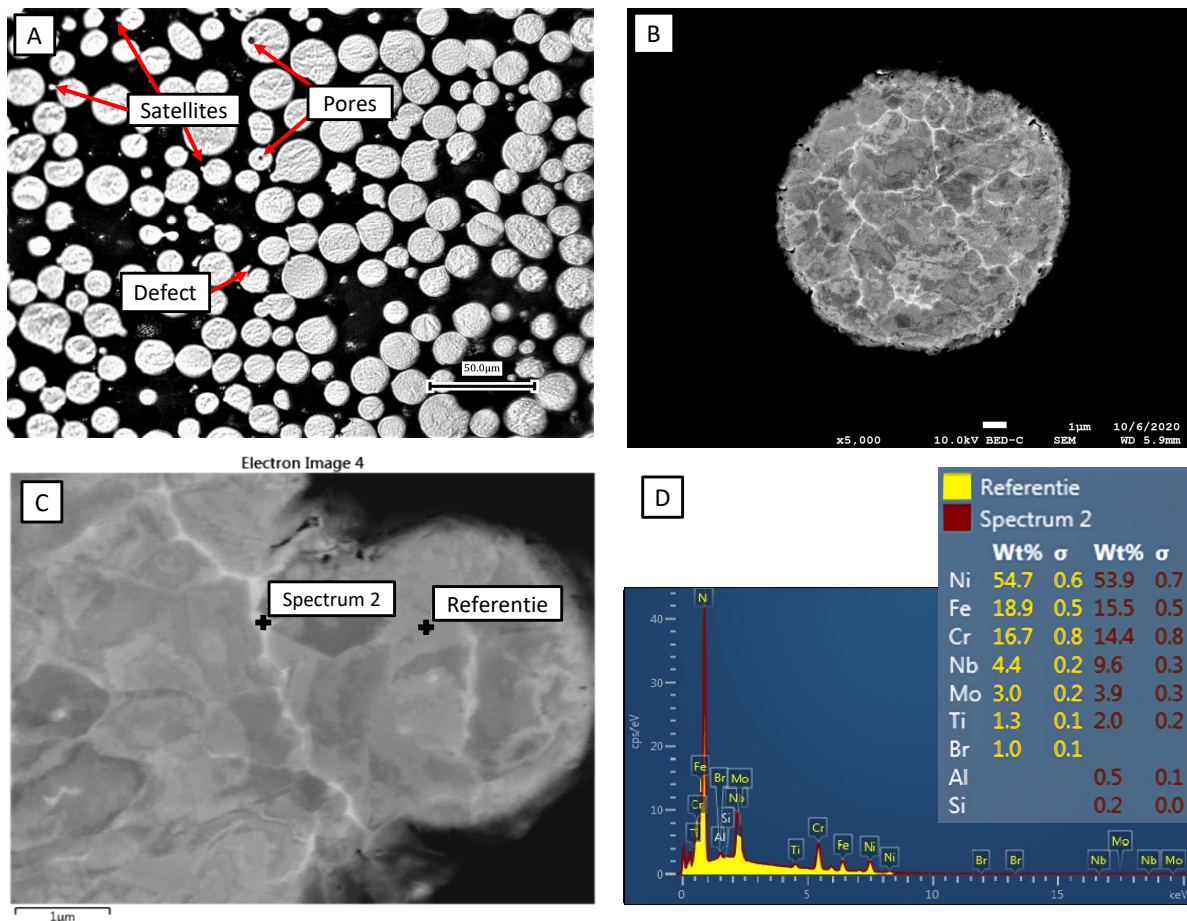


Figure 29: The microstructure of IN718 powder particles. (a) Optical micrograph of the cross-section of multiple powder particles; (b) SEM micrographs of a powder particle using back-scattered electrons; (c) Two locations used for EDS elemental mapping of the IN718 powder particle; (d) Chemical composition of the two locations.

Figure 29b shows the microstructure of a powder particle obtained by back-scattered electrons. It reveals a fine microdendritic microstructure of the spherical-shaped powder particle which was presumably caused by the rapid solidification rates in the GA process [74]. The chemical composition of the grey and white phase were measured by using Energy Dispersive X-ray Spectrometer (EDS) analysis. Figures 29c and 29d show the two measured locations and chemical composition of each location. Figure 29d reveals that the white phase area has a higher weight percentage of Nb, Mo and Ti and a lower concentration of Ni, Cr and Fe. The X-rays penetrate relatively deep into the surface (regions of about 2 microns). Therefore, EDS analysis is not suitable for surface composition measurements, according to [75]. However, it was assumed that the results provided an indication of the differences in the chemical composition of the two locations.

EBSD analysis was performed to observe the grains, see Figure 30a, and the different phases present in the IN718 powder, see Figure 30b. The powder particles had equiaxed grains and were relatively small due to the rapid cooling during the GA process. The phase analysis results (30b) revealed that the powder consisted mainly of the γ phase (red regions) and the Laves phase (yellow regions). Note that not all crystals were recognised as can be seen by the black spots, as shown in Figure 30b. The results revealed that the majority of the phases present in the powder were the γ phase and the Laves phase. The γ' could not be distinguished from the γ phase since it has the same FCC structure with almost the same lattice parameters [9].

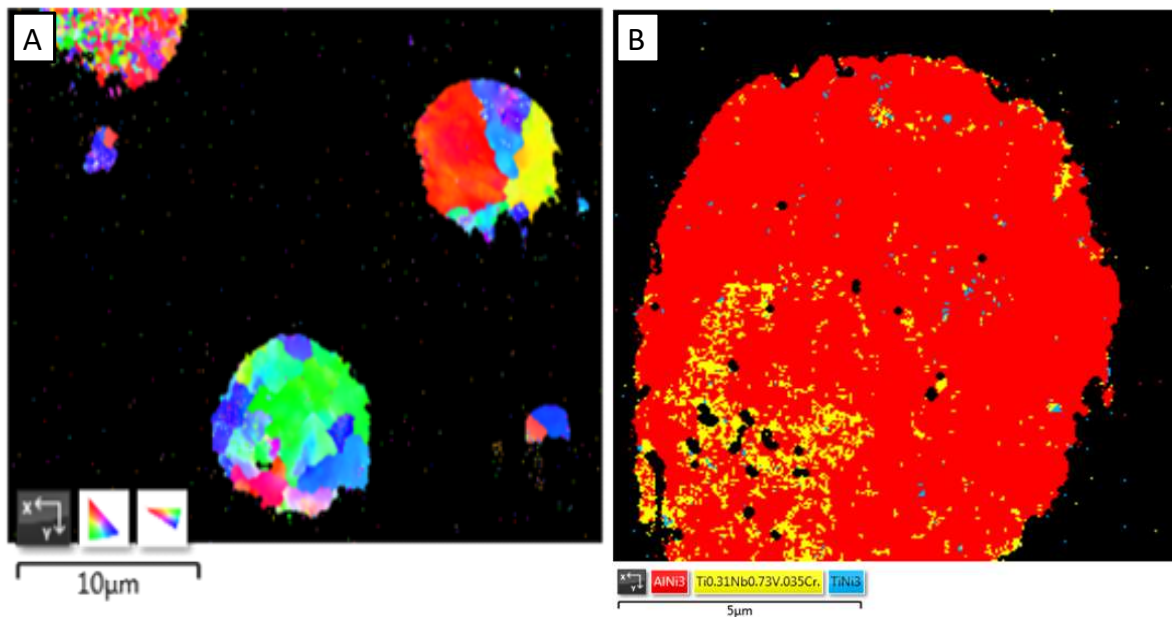


Figure 30: (a) EBSD analysis shows the grains of the IN718 powder particles and (b) shows the different phases present in IN718 powder particles.

4.2 Process monitoring

This section analysis the emitted thermal radiation during the manufacturing process of the inlet housing part. Regions with radiation that significantly deviated from the mean thermal radiation are discussed. The regions with high thermal radiation may indicate regions where the temperature was (temporarily) higher than average. Three locations are discussed and measurements such as density, surface roughness, hardness and grain sizes are also performed at these locations. The next sections contain the measurements of the features selected in the Experiment chapter.

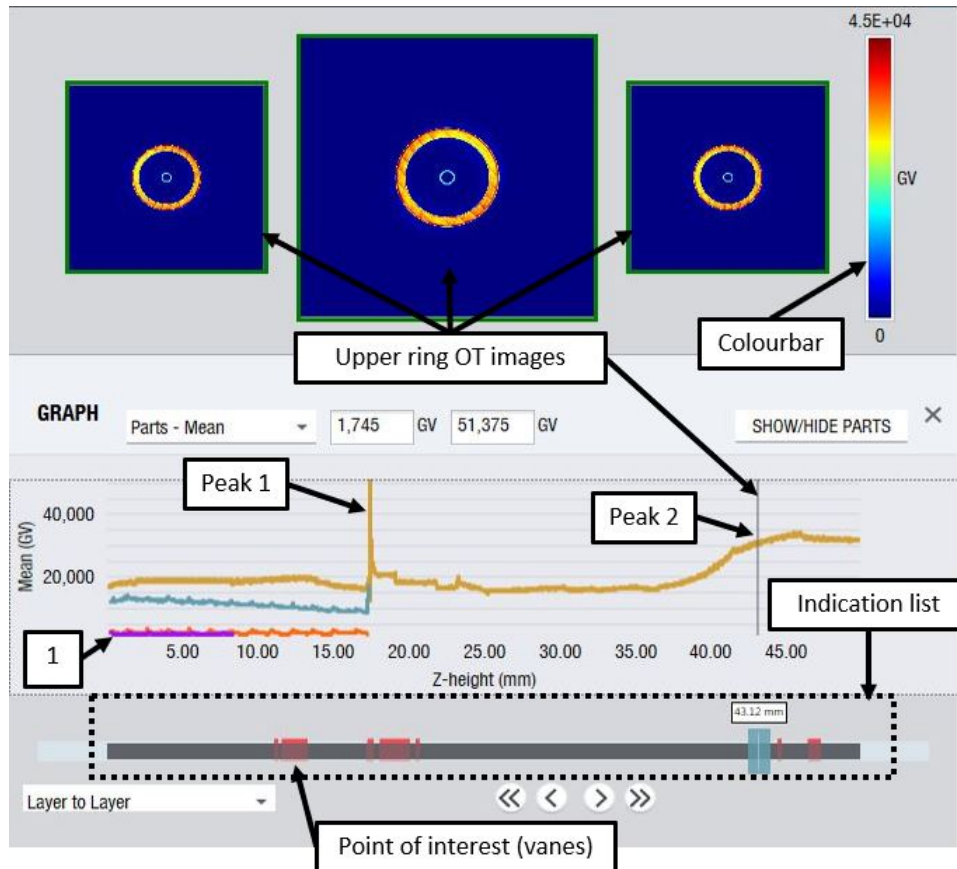


Figure 31: Raw data of the sCMOS camera monitoring the powder bed during manufacturing the inlet housing part. The brown graph represents the mean grey value from all pixels of a part for each layer. The purple graph, indicated with 1, represents the mean grey value of the support structure of the vanes. The indication list marks layers red that observed locally higher thermal radiation than a set threshold value of $4.5 \cdot 10^4$, see colourbar.

The thermal radiation of the inlet housing part examined in this research was detected during manufacturing by the sCMOS camera and the mean raw data of the camera (grey value) was plotted in a graph, see Figure 31. The brown line represents the mean grey value (MGV) of the inlet housing part and the other colours represent the mean MGV data of the support structures used to manufacture the part. The colourbar shows the amount of emitted thermal radiation, with blue colour representing low values and red representing high values. The brown line shows two interesting points in particular, indicated by peak 1 and peak 2, depicted in Figure 31. The location of the peaks is shown in Figure 33. The indication list marked the layers with higher thermal radiation levels at certain locations than the upper threshold value of the colourbar ($45,000$ MGv), see Figure 31. The first peak in the graph was caused by the transition of the support structure to the inlet housing part. The support structure had a lower volume fraction of solid material as compared to the inlet housing part. So, the heat dissipation through the support structure was lower. By manufacturing successive layers on the support structure, high thermal radiation was observed because it took more time to dissipate the heat. The emitted thermal radiation was the highest in the first layer and decreased after manufacturing successive layers since the volume fraction of solid material increased. Appendix B shows the OT images from the transition of the support structure to the first few solid layers of the inlet housing part.

Hardness measurements were conducted in this region showing high thermal radiation (peak 1) and the same regions showing mean thermal radiation around $20,000$ MGv. The results are shown in Figure

32. The hardness of the location with the high thermal radiation had a significantly lower hardness as compared to the bulk bottom and slightly lower hardness than the location showing mean thermal radiation in the same location. The microstructure in this region of the inlet housing part was not examined, so the influence of the thermal radiation on the microstructure was not investigated. Du et al. reported that a lower cooling rate will increase the concentration of Laves phase, which can be one of the contributors to the lower hardness [10].

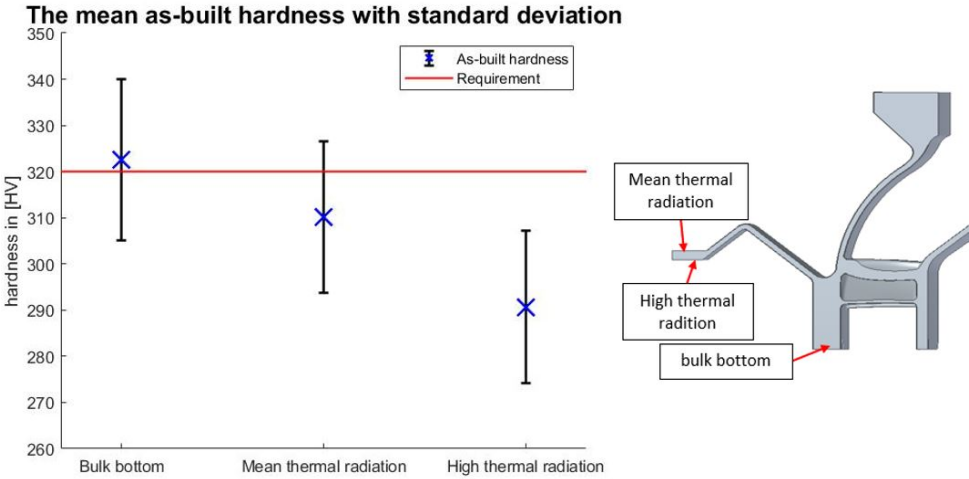


Figure 32: The mean hardness with plus-minus two times the standard deviation on the region with higher thermal radiation as compared to the other regions showing mean thermal radiation on the OT images. The locations of the measurements are also shown.

The second peak of the MGV (see Figure 31) corresponds to the highest section of the inlet housing part, which is lower and broader as compared to the first peak. The underlying structure was a thin wall which is not beneficial to the conduction of heat, leading to a lower cooling speed, which in turn led to a larger contribution of radiation as observed. This is illustrated in a 3D model shown in Figure 33. Note that the 3D model was created with another design of the inlet housing part since only a few OT images of the examined inlet housing part were available, as described in Chapter 3. However, the process parameters used to manufacture the part were identical as the examined inlet housing part in this research. Besides, the shape of the examined features was geometrically identical.

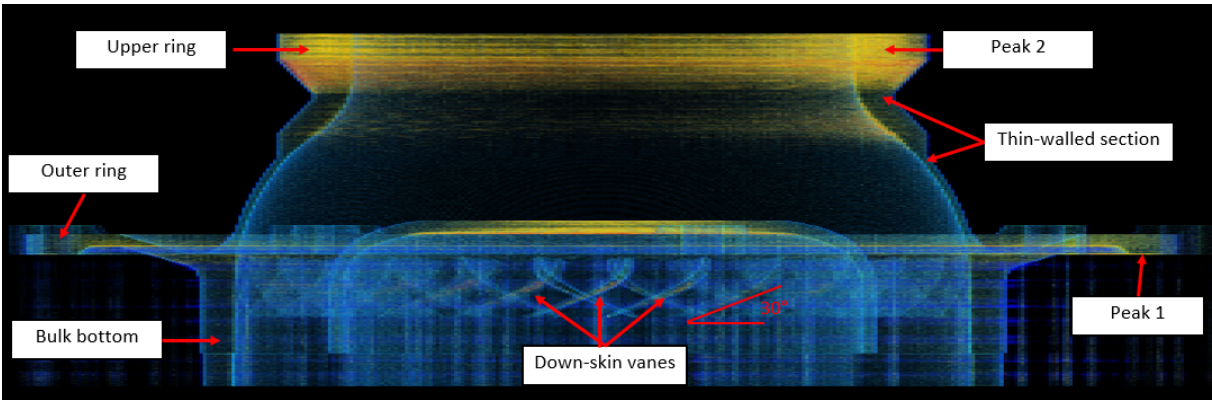


Figure 33: 3D model of the OT images created by the software ImageJ. The colourbar in Figure 31 gives the relation between the colour and the thermal radiation.

The inlet housing part was built on a relatively large build plate facilitating the conduction of heat

away from the weld pools at the start of the process. However, at the end of the manufacturing process, the distance to the build plate had grown and the geometrical features present may not support quick conduction of heat to the build plate. The lower cooling rates in the top of the part leads to coarser grains, according to literature [52]. However, the EBSD analysis did not confirm the hypothesis of the coarser grains in the top part. The number of grains in the upper ring was 463 compared to the bulk bottom with 422 grains. The results of the grain size distribution in the bulk bottom and bulk top are shown in 34. Besides, the density results (discussed in the next section) indicated a high density of the upper ring and no considerable differences between other samples without the higher thermal radiation were present. So, the grain analysis and density measurements did not reveal the origin and consequences of higher thermal radiation in this location.

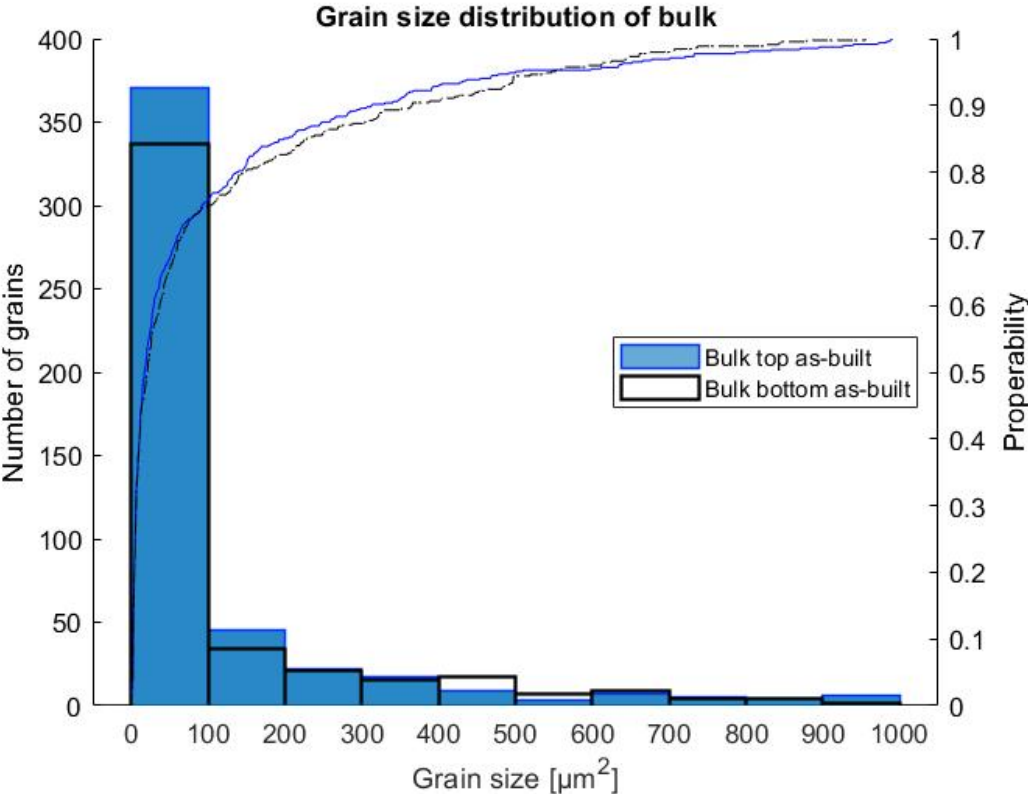


Figure 34: The grain size distribution of the bulk bottom and bulk top in the as-built state.

The down-skin surface of the vanes experienced locally higher thermal radiation during manufacturing as compared to mean thermal radiation of that specific layer, as depicted in Appendix D. Surprisingly, the radiation only appeared on one half of the inlet housing part. The high thermal radiation of the vanes is slightly visible in Figure 33. The indication list also marked the layers of the vanes because the vanes emitted higher thermal radiation than the set threshold value (45,000 MGV), see Figure 31. The high thermal radiation on the down-skin of the vanes was very localized. Therefore, the red colours are not good visible compared to the upper ring in the 3D model in Figure 33. Note that the 3D model is another version of the examined part, but the process parameters and the vanes' dimension had not been changed. So this should not influence the appeared overheating.

The first section of the vanes was built with small support structures from the build plate, see Figure 35. After the first section of the vane was manufactured, the vane was manufactured on powder, making a 30-degree inclination angle with the build plate. The overheating occurred on the down-skin of the

30-degree overhang in the middle of the vane. The purple line (indicated with number 1) in Figure 31 shows the thermal radiation of the support structures used to manufacture the first part of the vanes. Support infill process parameters were used to manufacture the support structure, as seen in Figure 5. Appendix D and E show a few OT images and powder bed images of the vanes, respectively. The reason why only one-half of the vanes showed overheating has to be further analysed. The following factors were taken into account: powder distribution after a recoater cycle, gas flow and thermal distortion.

To investigate the consequences of the higher thermal radiation, two vanes were cut from the remaining of the as-built top side part, one vane showing relatively high thermal radiation and one vane showing mean thermal radiation. The density and surface roughness measurements of these vanes revealed no large differences. The vane with mean thermal radiation showed slightly higher density and slightly higher surface roughness, see Table 7. The surface roughness was measured in the middle of the vanes over an area of $6348.9 \mu\text{m}$ by $3786.7 \mu\text{m}$. It was challenging to trace particular regions with high thermal radiation on the OT images back to the correct location, especially after cutting and embedding the samples. So, small-induced porosity found in Figure 38 and the vanes' surface topography could not be linked with the OT images.

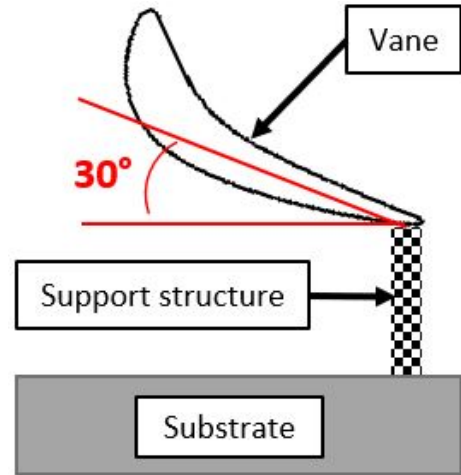


Figure 35: Schematic drawing of the build process of the vane.

Table 7: Density and surface roughness measurements on the vanes which showed mean and high thermal radiation. The location of the peaks are shown in Figure 33.

Samples	Density [g/cm^3]	Two times standard deviation	Surface roughness (R_a) [μm]
Vane showing mean thermal radiation	8.170	0.012	106.7
Vane showing high thermal radiation	8.163	0.032	97.2

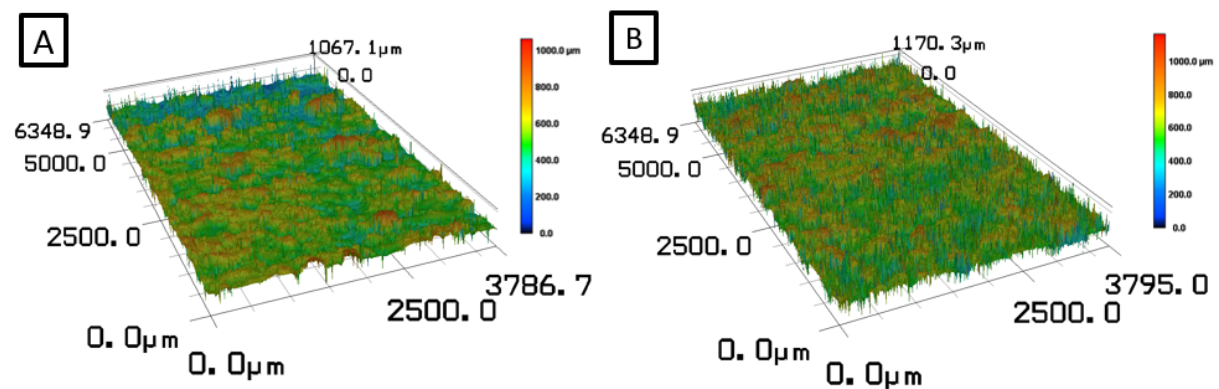


Figure 36: The surface topography maps of (a) the vane showing high thermal radiation and (b) the vane showing mean thermal radiation.

4.3 Porosity determination

The density measurements were performed to determine if the local density of each sample was in accordance with the requirements. The density of the samples was measured using the Archimedes

principle and the calculated mean density for each sample is shown in Figure 37. The results revealed that the local density of the inlet housing part was according to the requirement of 8.1 g/cm^3 . The samples were measured twice to increase the repeatability. The heat-treated samples showed more consistent results where the range was smaller as compared to the as-built sample range: $8.19 - 8.23 \text{ g/cm}^3$ and $8.13 - 8.23 \text{ g/cm}^3$, respectively. The as-built and heat-treated samples were both measured from different locations within the part. The heat-treated samples were not measured in the as-built state, so it could not be concluded that the heat treatment reduced the porosity in the samples. To obtain the influence of the heat treatment on the porosity, the samples should be measured before and after heat treatment.

Microstructure analysis was performed to get insight into the porosity's size and kind. Porosity plays an important role since it has an adverse effect on the mechanical properties of the part [61]. The micrographs revealed that gas-induced porosity was dominant in the samples with diameters up to $25 \mu\text{m}$. Few amounts of lack of fusion porosity type were also observed in the four examined features (the bulk bottom, the bulk top, the 45-degree overhang and the vanes), in contrast, the majority of lack of fusion was found on down-skin surfaces, as depicted in Figure 38. Micro-cracks were only observed on down-skin surfaces of the 45-degree overhangs and the vanes, which is also indicated in Figure 38.

The 45-degree thin-walled samples (AS-5, AS-6 and AS-9) showed lower density compared to the bulkier ones (AS-1, AS-2, AS-4 and AS-7). The influence of the surface roughness on the density was not measured. The thin-walled 45-degree overhang (thickness of $\approx 1.4 \text{ mm}$) had a very rough surface on the down-skin surface region. Optical micrographs showed that the high roughness induced some porosity close to the surface. The higher roughness was presumably the reason for the higher porosity of the thin-walled 45-degree samples and thus resulting in a lower density. The same reasoning could be used for the slightly lower density of the AS-3 and AS-8, which also had thin-walled 45-degree overhangs.

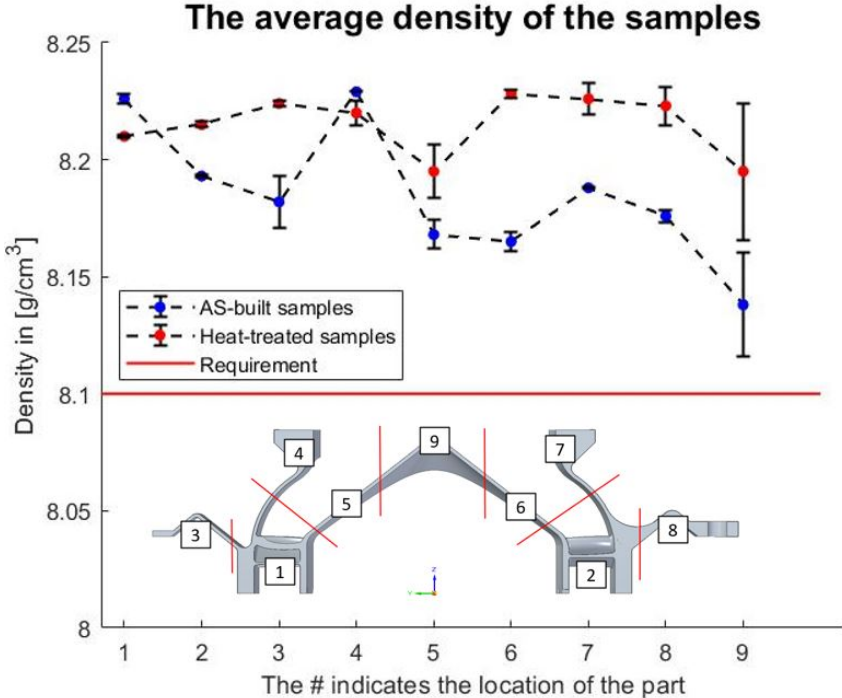


Figure 37: Graph showing the mean density of the as-built (blue dots) and the heat-treated (red dots) samples with plus-minus two times the standard deviation (solid black lines) of each sample. The location of each sample within the part is also indicated.

The AS-1 and AS-2 samples contained bulky parts and thin vanes, as seen in Figure 24. The vanes located in samples AS-1 and AS-2 showed on the optical micrographs a higher area fraction of porosity (measured with the software ImageJ) as compared to the bulk in the same sample, see Appendix F. In particular, the down-skin edge of the vane showed a higher area fraction of porosity (mainly gas and process-induced porosity), as depicted in Figure 38. However, the AS-1 and AS-2 samples' density measurements revealed relatively high-density values, which probably indicated that the high density of the bulky part of the samples concealed the lower density of the thin vanes.

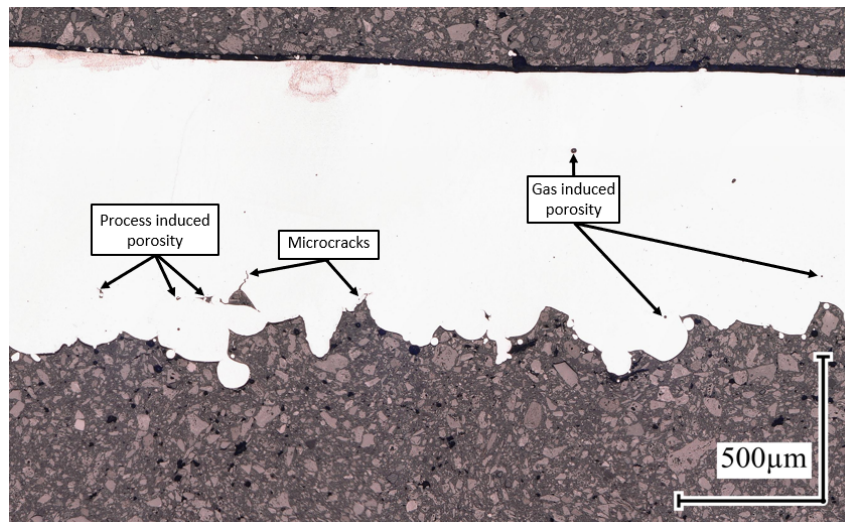


Figure 38: Optical micrographs of the as-built vane (AS-1) showing gas-induced porosity, process-induced porosity and micro-cracks.

4.4 Surface topography

The average arithmetic surface roughness was measured on four features and the results were plotted in a graph shown in Figure 39. The solid red line in the graph is the requirement ($3.175 \mu\text{m}$) given by Aeronamic. The horizontal, the vertical, the 45-degree up-skin and 45-degree down-skin have an average roughness of 2.51 , 5.37 , 7.88 and $21.34 \mu\text{m}$, respectively. The difference in roughness between the horizontal and the vertical surfaces is also notable ($2.86 \mu\text{m}$). The absence of sintered powder particles on the horizontal surface was the most significant difference observed, see Figure 40a. The horizontal surface did not have a layer of powder on top during the melting where the vertical surface had powder laying next to the melt pool. There were some small powder particles present on the horizontal surface, but these were most likely condensate particles that were ejected out of the melt pool during manufacturing.

Figure 40b shows the upper surface roughness of the 45-degree overhang indicating the two main challenges determining the roughness. Note that the area of the surface topography shown in Figure 40b is $750 \mu\text{m}$ by $500 \mu\text{m}$ and the area used for measuring the average roughness was $283 \mu\text{m}$ by $200 \mu\text{m}$, as presented in Figure 39. The roughness was primarily determined by the sintered powder particles attached to the surface and the error of the staircase effect, explained in Chapter 2. As discussed in literature, higher surface roughness was, in general, expected on the down-skin area of the 45-degree sample as compared to the up-skin area. The down-skin surface roughness was the highest, which confirms with literature. The down-skin surfaces were partially manufactured on powder particles which had lower thermal conductivity than the solid material. The heat of the melt pool accumulated due to the lower thermal conductivity and the melt pool sank downwards into the powder bed. The

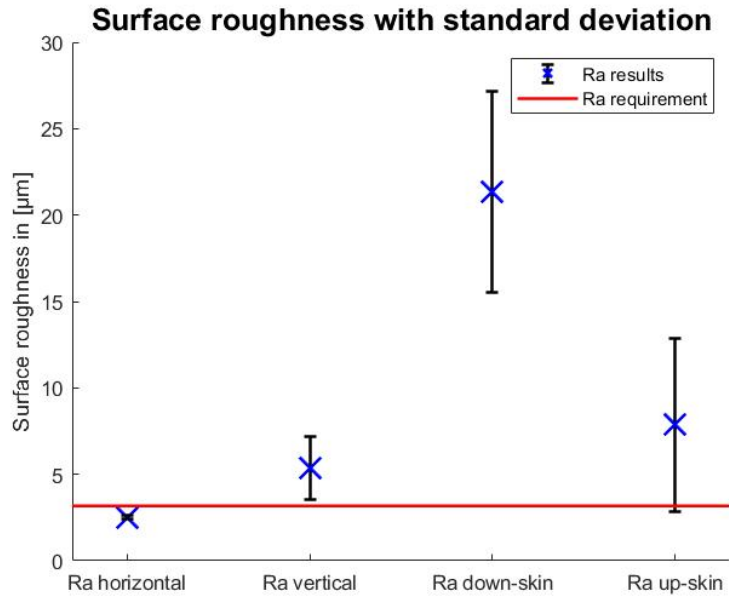


Figure 39: Graph showing the average surface roughness (blue) and the plus-minus one times standard deviation (black). The red line indicates the surface roughness requirement given by Aeronamic. The locations of the measurements are shown in Figure 27.

powder particles laying close to the melt pool boundaries were sintered to the surface, see Figure 42. Post-processing is needed to obtain lower surface roughness, mainly on down and up-skin surfaces to meet the requirements. It is not even possible to meet the requirements by manufacturing simple geometries, according to literature [63, 66, 67], let alone a complex part examined in this research.

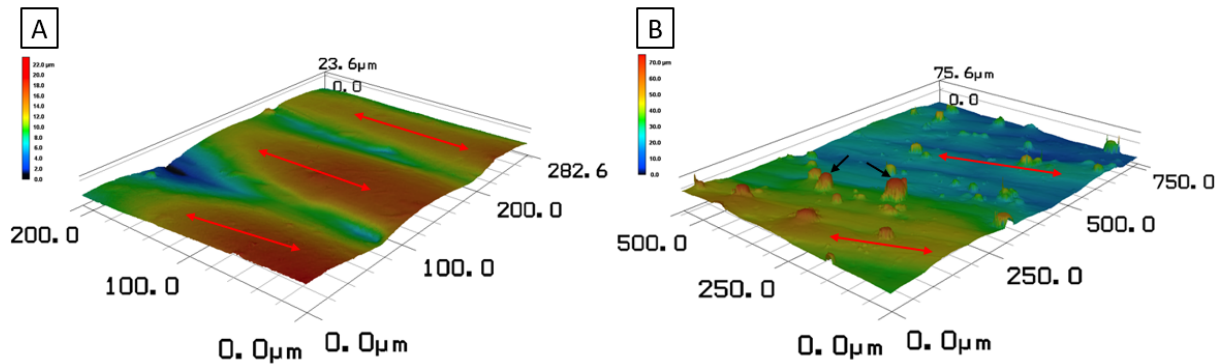


Figure 40: The surface topography maps of (a) the horizontal surface (AS-3) and (b) the 45-degree up-skin (AS-5) with recognizable scanning lines (red arrows) and unmelted powder particles stuck to the surface (black arrows).

4.5 Microstructure observations

The microstructural evolution of the as-built samples was analysed to examine the relation between the process conditions and the microstructure. Different features (the vanes, the thin-walled 45-degree overhang, the bulk bottom and bulk top) were examined to understand the influence of the features on the melt pools, grain morphology, and the formation of phases and precipitates. These microstructural properties are compared with heat-treated samples to find the influence of the heat treatment on the microstructure.

4.5.1 Microstructure analysis

Figures 41 and 42 show the microstructure of the bulk bottom and the 45-degree overhang on the y-z plane before and after heat treatment. In both figures the many melt tracks deposited to manufacture the part are discernible for the as-built microstructures (see Figures 41a and 42a) but cannot be observed anymore after the heat treatment (Figures 41b and 42b). Dendritic cellular grain structure is visible in the microstructure of the as-built samples. The as-built samples show an inhomogeneous microstructure with small dendrites at the edge of the 45-degree overhang. The heat-treated microstructure looks more homogeneous. Columnar grains aligned almost parallel along the build direction are visible in the heat-treated state. It can be seen that the heat treatment had an essential effect on the microstructure. The grains look larger as compared to the as-built microstructure. Still, the grain sizes are difficult to measure for the as-built specimens, which indicated EBSD analyses are needed to obtain a quantitative evaluation of the grain size distribution and orientation.

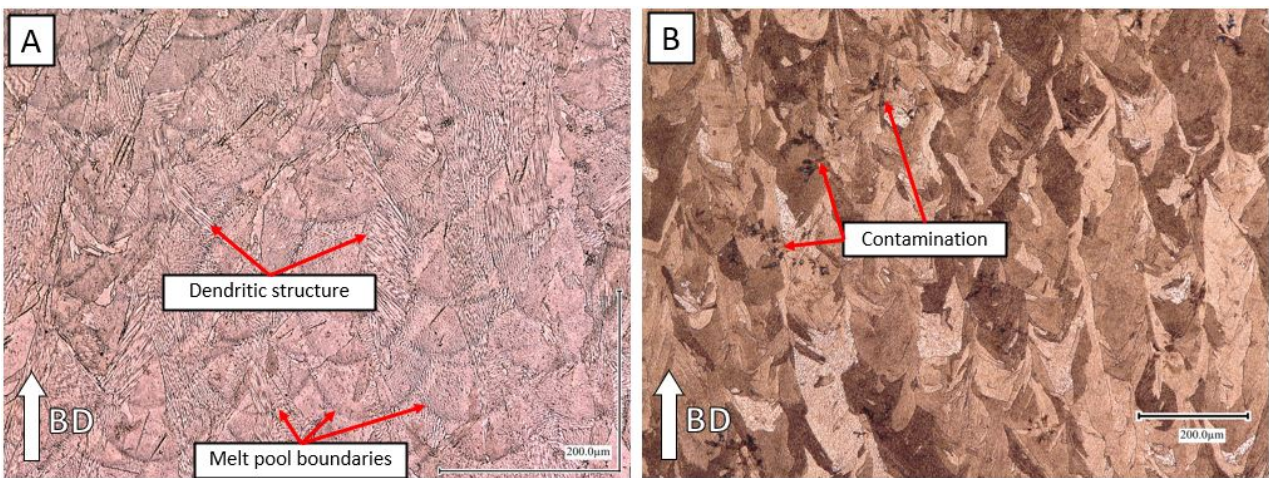


Figure 41: The etched microstructure of the bulk bottom sample in (a) as-built (AS-1) and (b) heat-treated state (HT-1). The build direction (BD) is orientated upward.

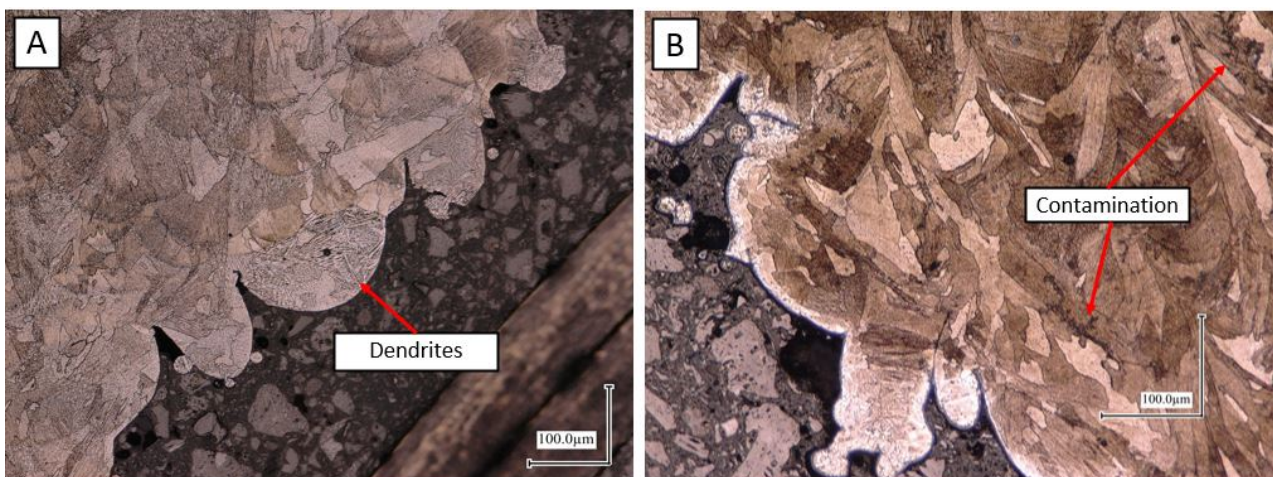


Figure 42: The etched microstructure of the 45-degree overhang in (a) as-built (AS-7) and (b) heat-treated state (HT-7).

The microstructure of the vane in the as-built state is shown in Figure 43 and the heat-treated microstructure of the vane in Appendix G. The as-built samples reveal at the bottom of the vane small

dendrites. The melt pool boundaries are also slightly visible and disappear after the heat treatment. The melt pools look less deep as compared to the melt pools observed with the bulk bottom and the 45-degree overhang samples, see Figure 41a and 42a. The as-built and heat-treated samples show fine grains with random orientation on the bottom and top side of the vane which are visible on the grain map overview of the vane, see Appendix G. Upon solidification, the grains show directional growth of columnar grains towards the build direction which are visible in the heat-treated part. The size of the grains is difficult to quantify, especially in the as-built state.

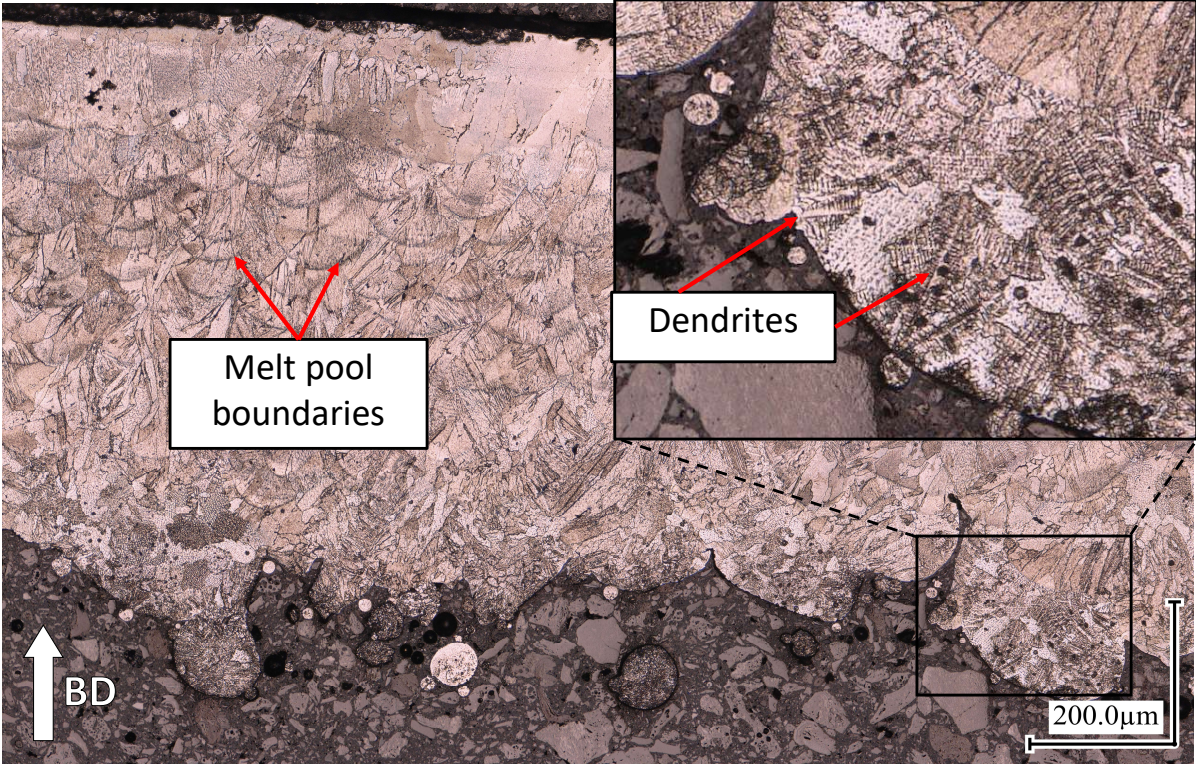


Figure 43: The etched microstructure of the vane in as-built state (AS-1).

4.5.2 Other observations

The micrographs showed contamination on the samples after etching, see Figure 44. The steps taken to find the cause of the contamination is shown in Appendix H and Figure 70. It was concluded that the etching procedure caused contamination on the samples. It seemed that etchant remained in pores, microcracks and gaps in the transition regions between the embedded resin and the sample. It was not washed away after cleaning, and the hairdryer blew the liquid out and over the surface, which created these branches like contamination. Further investigation (non-destructive) should be done in order to discover if there are pores, micro-cracks and gaps that the microscope could not observe. These small defects can have an adverse effect on the mechanical properties of the part.

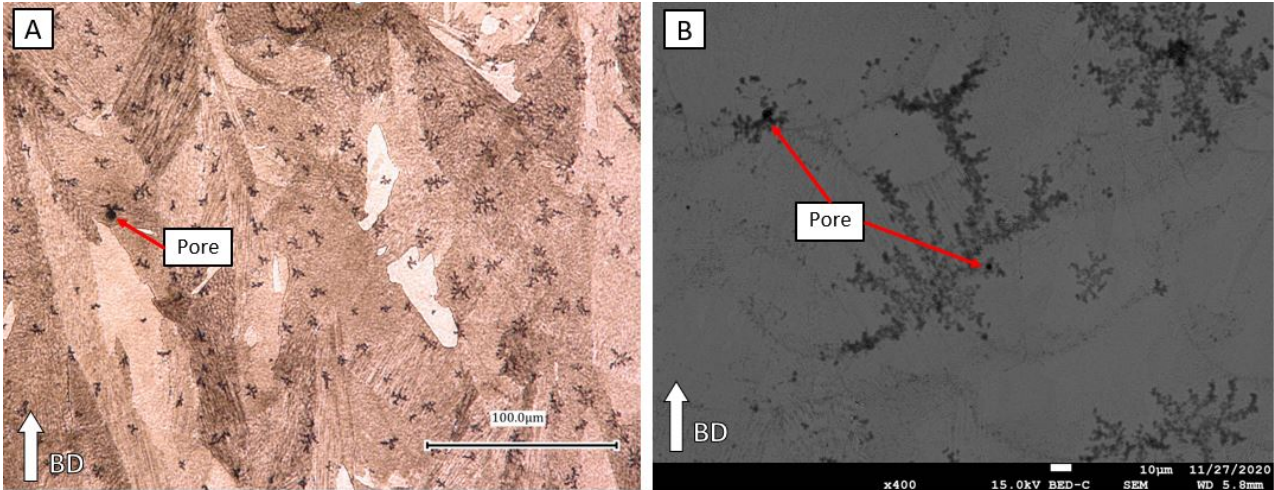


Figure 44: (a) Optical micrograph showing contamination after etching a sample with a solution and precipitation heat treatment (HT-1 bulk bottom) and a pore indicate the cause of the contamination and (b) showing SEM image with the contamination of the vane after etching with only precipitation heat treatment (HT-1).

4.5.3 Melt pool characteristics analysis

This section measured the melt pool dimensions which is important characteristic to prevent lack of fusion, as explained in Chapter [73].

The melt pool characteristics were examined in four different features of the inlet housing part. The depth and width of the melt pools were measured 10 times on each location and the average values are given in Table 8. The melt pool dimensions were measured on the locations manufactured with only part infill process parameters, see Table 5. Table 8 shows that the measured depth of the melt pool was larger than the layer thickness, while the width was almost the same as the hatch spacing. Figure 45 shows the melt pools of the bulk at the bottom of the part obtained by optical microscopy. Although the manufacturing parameters were not changed in the course of this work, the depth and width (shape) of the melt pools have noticeable differences, see Figure 45. One reason for the differences in the width of the melt pools can be explained as follows. After each layer, the laser scan pattern was rotated with an angle of 67 degrees. To measure the melt pools, cross-sections of the samples were taken, but it was unknown how the melt pools were oriented with respect to each manufactured layer in that particular cross-section. In other words, the exact width of the melt pool could only be measured exactly by taking a cross-section perpendicular to the longitudinal direction of the melt pool. Considering that the laser scan pattern was rotated each build layer, the cross-section of the sample was probably not perpendicular to the melt pool cross-section. So, the measured width must be higher than the actual width of the melt pool. This reasoning does not apply for the depth of the melt pool. The cross-section taken of the samples was parallel to the build direction, so the depth of the melt pool should be representable for the actual depth.

The density of the L-PBF manufactured parts is mainly dependent on the following three dimensionless ratios of the melt pool characteristics:

- Melt pool length/width of melt pool ratio (L_m/w);
- Melt pool width/hatch spacing ratio (w/h_s);
- Melt pool depth/layer thickness ratio (D_m/h).

Table 8: The melt pool characteristics of four features manufactured with part infill process parameters.

Features	Average depth \pm standard deviation (μm)	Depth/thickness ratio	Average width \pm standard deviation (μm)	Width/hatch ratio
Bulk bottom	76.8 ± 16.4	1.95	118 ± 12.1	1.07
Bulk top	84.3 ± 13.9	2.11	111.8 ± 13.5	1.02
45-degree overhang	88.9 ± 10.1	2.22	114.6 ± 8.6	1.04
Vane	60.3 ± 14.6	1.51	110.3 ± 19.2	1.00

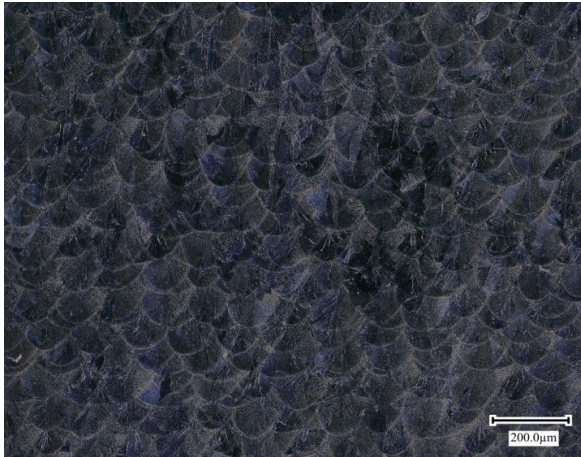


Figure 45: The melt pools of the bottom bulk (AS-1) manufactured with the part infill process parameters.

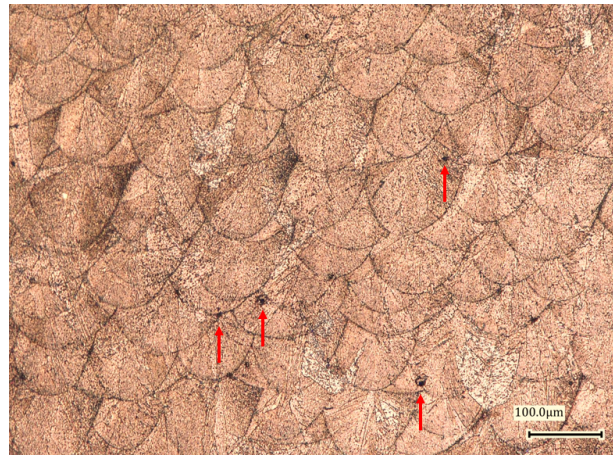


Figure 46: Optical micrographs of the melt pools (AS-1) showing porosity at the melt pool boundaries. It was manufactured with the part infill process parameters.

In this research, the length of the melt pools was not measured, so this ratio was not taken into account. The melt pool's length to width ratio is important for the balling phenomena where higher ratios lead to balling [76]. The layer thickness (h) is the theoretical thickness of the powder bed going down. After melting a layer of powder particles to solid, the mass remains the same. However, it is important to know that melting the powder layer removes the empty spaces (voids) between the powder particles leading to a higher density. It also leads to a solid layer located a bit lower than the powder layer it was created from [77]. After exposure of the laser, the average thickness of the solid material is around 40 microns, but the deposited powder layer thickness is approximately larger.

According to V, Brailovski et al. previous studies showed that the highest density was generally obtained with the following ratios: $1.5 < (D_m/h) < 2$, $1.5 < w/H_s < 2.5$ [76]. It was observed that the depth/layer thickness ratio was higher than 1.5, see Table 8, which indicated enough remelting to obtain good bonding between layers. However, the calculated width/hatch spacing ratio of the melt pools was around 1. Note that the density of the samples tested was still within requirements (higher than 99 % dense). Gas-induced porosity was also more dominant at the bottom of the melt pool boundaries, as shown in Figure 46. The optical micrographs showed a few lack of fusion porosity types in the four examined features, but much more and bigger lack of fusion was found at the bottom of the vane, as illustrated in Figure 38. Fraunhofer Project Center manufactured specimens using the same process parameters to manufacture the inlet housing part but used 90 and 110 μm hatch spacing (110 μm was used in this research). The density measurements did not indicate higher density 99,7 and 99,8 %, respectively [68]. However, it was expected that the lack of fusion porosity type could be minimized by increasing the width of the melt pools (higher laser power or lower laser speed) or decreasing the hatch spacing.

The depth/thickness ratio of the melt pools of the vane was remarkably smaller ($1.51 \mu\text{m}$) as compared to the other features (1.95 , 2.11 and $2.22 \mu\text{m}$), as shown in Table 8. Low depths are usually linked to low laser power or high scanning speed which contributes to a decrease in the dwelling time. The vane can be seen as a thin-walled section that was manufactured under a 30-degree inclination angle with the build plate, see Figure 35. The melt pools were measured in the centre of the vanes because the first three layers of the vanes were manufactured with down-skin parameters that allowed partial melting of the powder particles. So, the measured melt pools were manufactured with the same process parameters as the bulk bottom and the 45-degree overhang. The powder bed images showed no powder distribution over one side of the vanes by manufacturing the 30-degree overhang, see Appendix E. The measured sizes of the melt pools of the vanes correspond to the vanes with no powder distribution after a recoater cycle. Solid surfaces have a lower laser absorption as compared to powder surfaces which are schematically drawn in Figure 47. So less energy from the laser was aborted during the manufacturing of the vanes, leading to a lower depth of the melt pools.

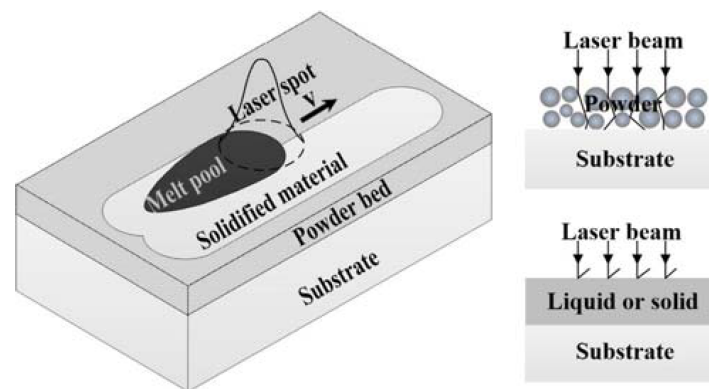


Figure 47: Schematic of the laser absorption mechanism during L-PBF process taken from [15].

4.5.4 Phases and precipitates

The microstructures of the as-built and the heat-treated samples were further analysed using backscattered electrons (BSE) of the samples' non-etched surface. Figure 48a shows small irregularly shaped white phases located in the inter-dendritic regions in the as-built state. The melt pool boundaries are difficult to observe in the BSE micrographs. However, the melt pool boundaries are slightly visible at some locations due to the change in dendritic arm spacing which is smaller in the bottom of the melt pool and becomes larger to the top, as seen in Figure 48b. It is observable that the grains cross the melt pool boundaries. The direction of the dendrites (and the grains) looked non-homogeneous, but in Figure 48b, it becomes clear that the dendritic structure grew roughly in the direction of the heat flux during the manufacturing process. Arguably, the dendrites in the bottom centre of the melt pool are going upwards (parallel to the build direction), and the dendrites on the sides of the melt pool boundaries tend to grow towards the middle of the melt pool. This gives a zig-zag pattern (or v-shape) and is further explained in the Discussion Chapter 5.

Previous studies on IN718 showed that these white phases on inter-dendritic boundaries are rich in Mo, Nb and Ti (of higher atomic number) which are the important elements of composing the Laves phase [10, 18, 20]. R. Jiang et al. also predicted microstructure segregation of Nb, Mo and Ti elements since the concentration of these elements becomes higher during solidification due to the depletion Cr and Fe elements in the liquid [78]. In other words, the solidification of the dendrites predominantly consumes Ni, Cr and Fe but refuses Nb, Mo and Ti, leading to substantial segregation and the formation

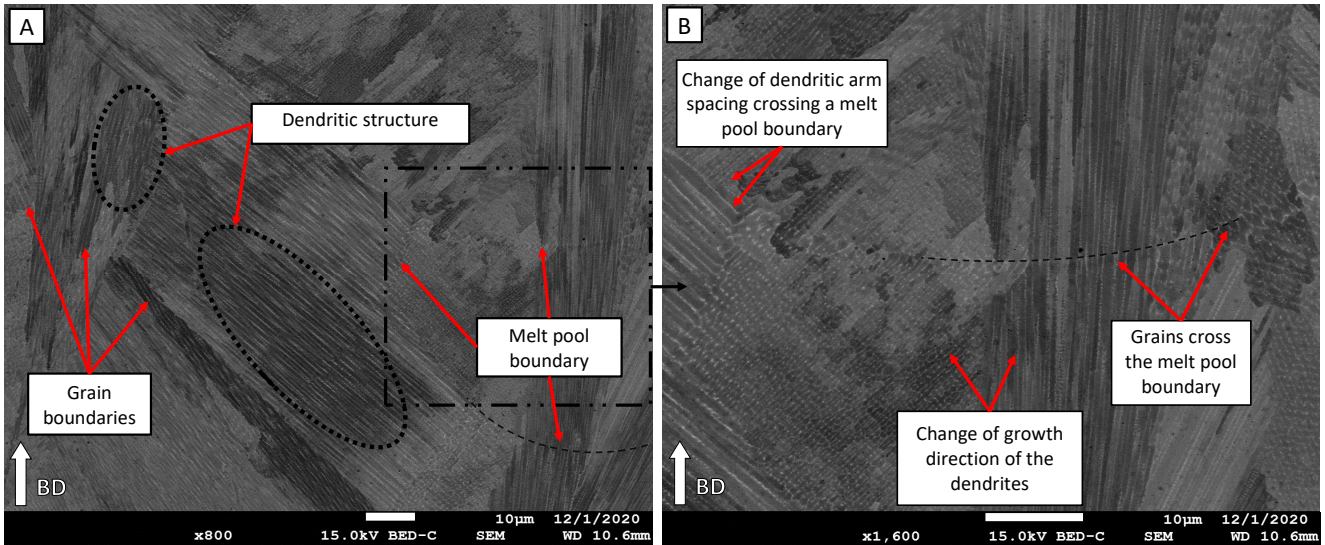


Figure 48: BSE micrographs of the bulk bottom in as-built state (AS-1) showing (a) columnar dendritic structures, grain boundaries, (b) change of dendritic arm spacing crossing a melt pool boundaries and columnar dendrites crossing melt pool boundaries.

of inter-dendritic phases [78], also explained in Chapter 2.1.

Higher magnifications of the as-built micrographs showed areas cellular-dendritic morphology and a mean dendritic arm spacing of $1 \mu\text{m}$ was observed in the bulk bottom, see Figure 49. The dendrite arm spacing in each region deviated from $0.5 - 2 \mu\text{m}$ but no large differences in dendritic arm spacing were found between different features. Also, fine black circular-shaped spots were obtained in the as-built matrix. Similar black spots in the as-built state were also observed by E. Chlebus et al. [79]. EDS analysis concluded that these black spots are fine MC-type carbides rich in Nb and Ti [38, 74, 79].

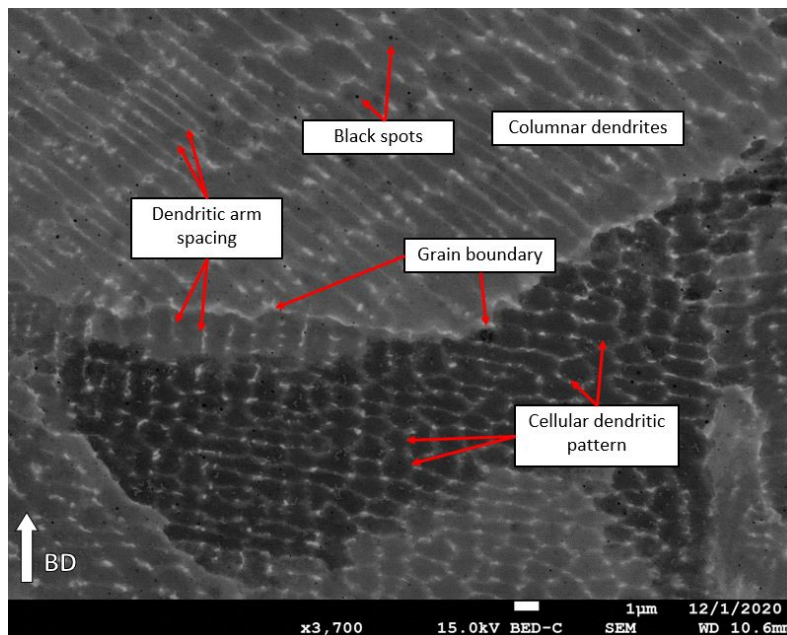


Figure 49: BSE micrograph of the bulk bottom (AS-1) showing the dendrites with hexagonal pattern, columnar dendrites and carbides.

Figure 50a and 50b illustrate the different phases and precipitates observed in heat-treated samples

of the bulk top. The fine columnar dendritic structure with the Laves phase on interdendritic boundaries had disappeared during the solution heat treatment. However, according to literature [20], the solution heat treatment is not sufficient to completely dissolve the Laves phase to improve precipitation of the γ' and γ'' phases for AM Inconel 718. So, the presence of the Laves phase is expected in the microstructure after heat treatment. The melt pool boundaries are not visible after solution and precipitation heat treatment. Higher magnifications show numerous white phase precipitates on grain boundaries and thin ellipsoidal discs precipitates rotated 90-degree angles from each other appear throughout the matrix and on the grain boundaries, as seen in Figure 50. These nanometric scale disk-shaped precipitates are γ'' precipitates also reported in heat-treated specimens using transmission electron microscopy (TEM), by [80, 81]. Previous studies also observed disk-shaped precipitates by using the SEM, but the EDS penetration depth was too large to identify the specific composition of the precipitates [5].

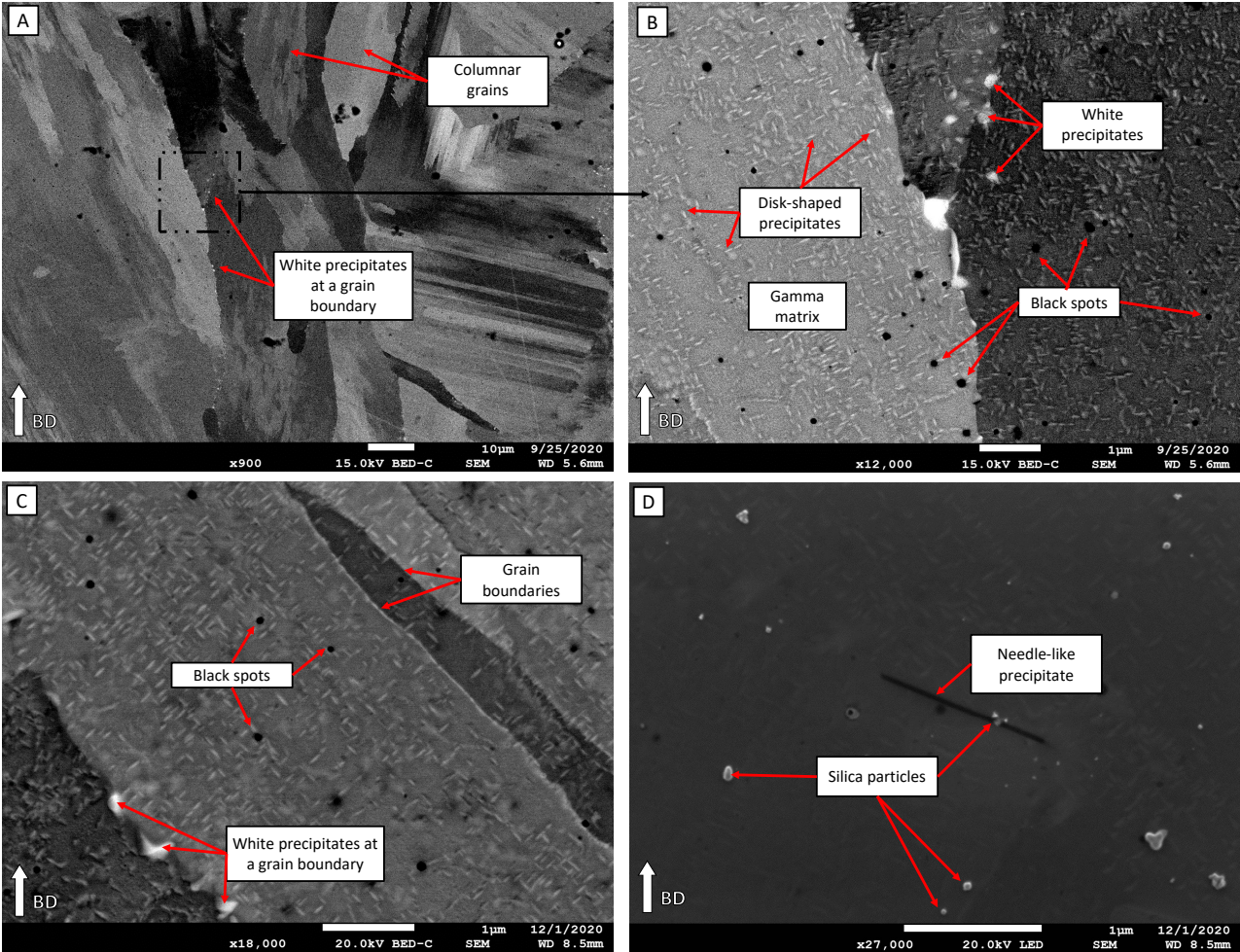


Figure 50: BSE micrographs showing the heat-treated micrograph of (a) and (b) the bulk top (HT-4), (c) bulk bottom (AS-1) (D) needle-like precipitate located in the bulk bottom (AS-1). The (b) and (c) micrographs showing disk-shaped precipitates distributed in the gamma matrix.

Furthermore, round/cuboidal shaped black spots unevenly distributed throughout the Ni rich gamma matrix were observed after heat treatment. These black spots are most likely Nb-rich and/or Ti-rich MC primary carbides [38] but note that no EDS analyses were performed in this research to identify the composition. Figure 50d displays a needle-like phase with a length of 1.3 μm. This typically looks like a Delta phase that generally precipitates at grain boundaries. This black needle like delta phase was also

observed by M. Medraj et al. [5].

In conclusion, it seems that the manufacturing conditions employed led to a microstructure and associated microstructural phases that were observed in literature as well.

4.5.5 Grain morphology

EBSD measurements were performed to analyse and quantify the grain size distribution and orientation which could not be observed by OM. The grain map of the bulk bottom sample in the as-built and the heat-treated state are shown in Figure 51. The results reveal that the majority of the grains are columnar and elongated parallel or almost parallel to the building direction. These columnar grains are typically observed in the L-PBF process because the heat dissipation happens downwards from the powder layer to the build platform. The grains in the as-built and heat-treated state have an average length to width ratio in between 2.5 - 3 and some grains with a length over $200 \mu\text{m}$ are identified. Therefore, several grains crossed the melt pool boundaries through more than 5 manufacturing layers in both as-built and heat-treated samples. Besides, a zig-zag (or V-shape) shaped pattern is observed in the grains which is also recognised from the dendrites direction in the as-built micrograph, see Section 4.5.4. The origins of the columnar grains and zig-zag pattern are discussed in the Discussion chapter 5.

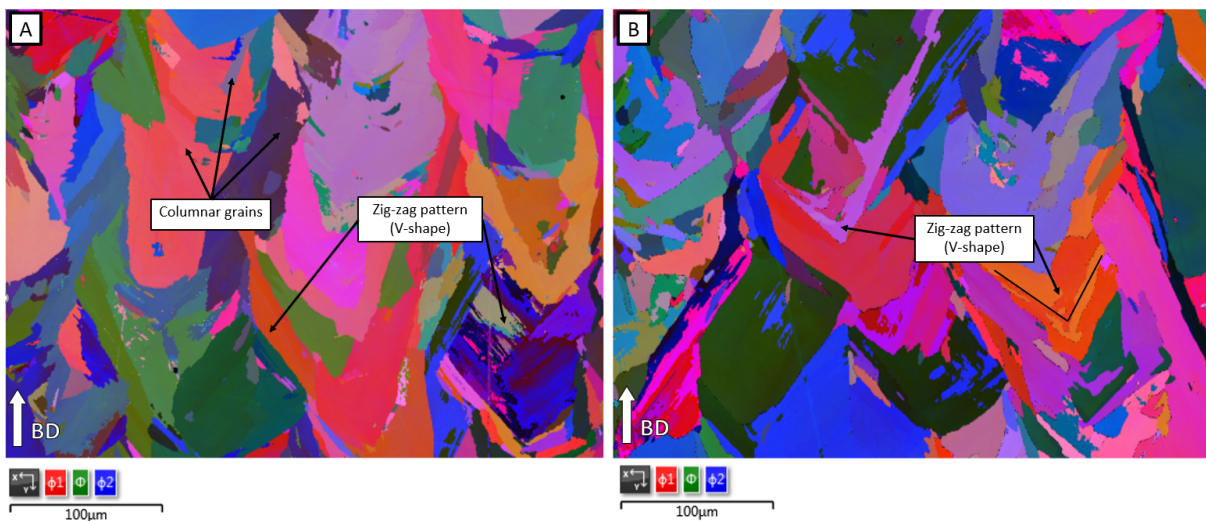


Figure 51: EBSD analyses showing the grains and the zig-zag pattern of the grains in the bulk bottom in the (a) as-built (AS-1) and (b) heat-treated state (HT-1).

The grain size distribution of the three different features (the bulk bottom, the 45-degree overhang and the vanes) for the as-built and the heat-treated samples was obtained, covering an area of $400 \mu\text{m}$ by $300 \mu\text{m}$ and the results are shown in Figures 52. The vane, bulk bottom and 45-degree overhang have in as-built state 515, 422 and 324 grains and in heat-treated state 434, 256 and 332 grains, respectively. The vane in the as-built state has the highest number of grains and the 45-degree overhang the lowest. The heat-treated 45-degree sample has more grains as compared to the as-built one. The heat-treated samples have fewer grains sizes smaller than $100 \mu\text{m}^2$ and more grains sizes larger than $100 \mu\text{m}^2$. It is clear that after the solution heat treatment, the average grain size increased and the number of grains decreased. This phenomenon is also called grain growth. This phenomenon happens when crystallisation and recovery are completed. To further decrease the material's internal energy, the total area of the grain boundary has to decrease since a defect in the crystal structure is associated with a certain amount of energy. By heating the material, kinetic energy is added, allowing the atoms to move faster. When the

total energy of atoms is larger than the energy barrier, the atoms can slide and slip into new positions, leading to increased grain size [82].

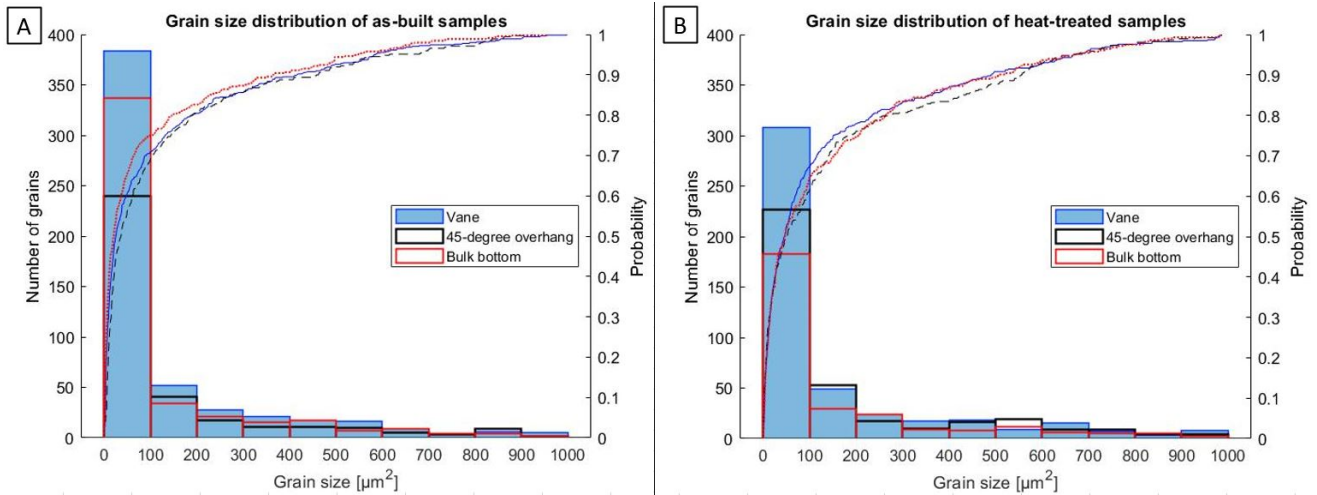


Figure 52: Grains size distribution of the bulk bottom, the 45-degree and the vane in (a) the as-built and (b) heat-treated state.

4.6 Microhardness

This section discusses the hardness, which is a measure of the mechanical properties. The hardness was measured to see how these properties are related to the manufacturing process. The hardness is measured on features which are geometrically quite different. This is done to find the difference in heating/cooling rates. Figure 53a shows the average micro-hardness of the as-built and heat-treated samples on four different features. The red line indicates the required hardness, which is 320 *HV*. The mean microhardness was strongly increased from 300 - 350 *HV* in the as-built state to 480 - 500 *HV* after heat treatment which well exceeds the required value. The as-built samples have notable variation between the mean values of the examined features but statistically less relevant due to the overlap of the standard deviation line between the features. The highest hardness in descending order was found in the 45-degree overhang, the bulk bottom, the vane and the bulk top. The heat treatment reduces any variations (homogenised) between the different features that were present in the as-built state. Therefore, the studied geometrical features did not exhibit significantly different hardness values after heat treatment in this part. The hardness variation per location was still present. The higher microhardness of the heat-treated samples was mainly caused by the strengthening precipitates γ' and γ'' that were formed during the precipitation heat treatment.

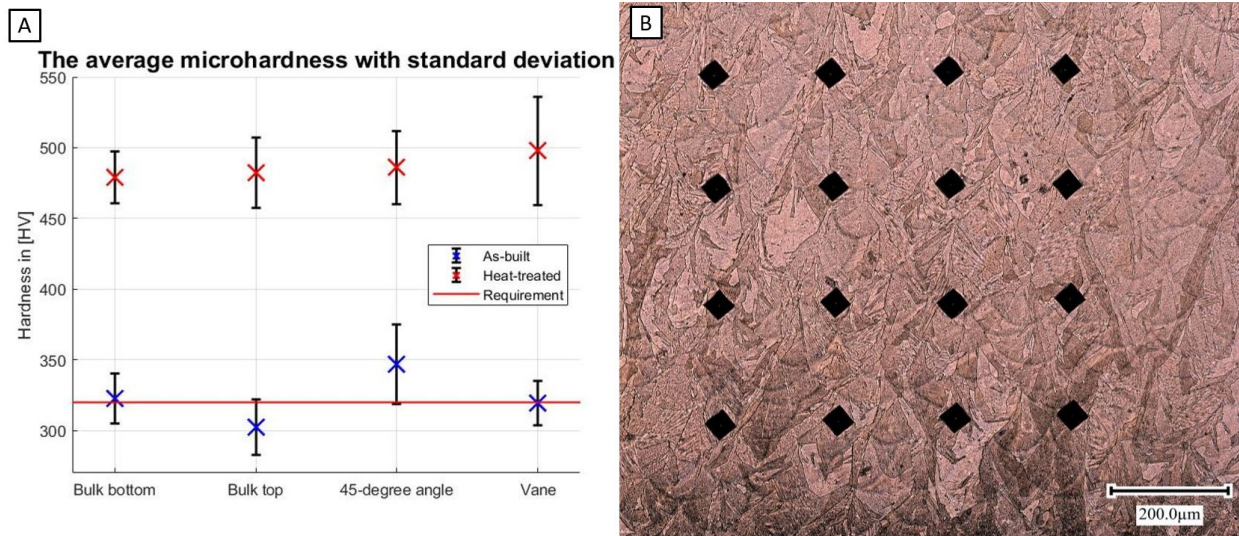


Figure 53: (a) showing micro-hardness of as-built and heat-treated samples with the mean and plus-minus two time standard deviation at 4 different features and (b) showing the hardness indents of the as-built bulk bottom (AS-1).

The two times standard deviation is around (plus-minus) 20 *HV*. Figure 53b shows the location of the indents on the bottom bulk in the as-built state. The microhardness was measured in a four by four matrix, but the indents were randomly located on the microstructure, which may cause the hardness results to vary. A few indents were measured inside the grains and melt pools while other ones were measured on the grain and melt pool boundaries. It was expected that this had caused the variation in hardness for each particular location since these boundaries make it harder for a dislocation to move, increasing the hardness of the material.

5 Discussion

This chapter evaluates the importance and relevance of the results and discusses the results with literature to find answers to the research questions. The process monitoring observations and the microstructure development of the as-built and heat-treated samples are discussed.

5.1 Process monitoring

The OT images showed regions with higher thermal radiation as compared to other regions with mean radiation (see Figure 64, 65 and 66). A simplified thermal model was made to calculate the heat build-up and solidification cooling rate to understand why these regions on the OT images showed higher radiation than the mean. Section 5.1.2, 5.1.3 and 5.1.4 discuss the specific geometrical features of the part.

5.1.1 Heat conduction during additive manufacturing

As described in the previous chapter, the heat dissipation through the support structure seemed insufficient, leading to higher temperatures and stronger radiation throughout multiple consecutive layers manufactured on the support structure. A thermal model, based on the research of H. Song et al. [50], was constructed in Matlab programming software to get more insight into the cooling rate and heat build-up from the transition of the support structure to the solid material of the part (see Figure 3). The heat build-up was calculated by taking the difference between the heat input from the laser and the heat dissipated through the support structure, see Figure 54. Important parameters for the calculations are presented in Table 9 and Figure 54. The following assumptions and boundary conditions were made to simplify the calculations:

- The heat conduction through the support structure was only considered in the build-direction (z-direction). The heat dissipation by convection of the gas-flow was neglected. In addition, the heat conduction through the loose powder particles, for instance, the powder particles existing between the grid lines of the support structures, was considered negligible. L.C. Wei et al. calculated the thermal conductivity of metal powder bed in an argon atmosphere and reported that the thermal conductivity of IN718 powder bed is less than $1/100^{th}$ compared to the solid bulk material. The thermal conductivity of the IN718 powder bed at a pressure of 101 kPa is $2.2 \cdot 10^{-4} J/(mm \cdot s \cdot K)$ which is approximately 10 times larger compared to the thermal conductivity of argon gas $1.76 \cdot 10^{-5} J/(mm \cdot s \cdot K)$ [53].
- It was assumed that the build plate was kept at a constant temperature of 80 °C, which does not change over time. The support structures were also at 80 °C at the beginning of the calculations. Besides, the thermal gradient in the support structure was not taken into account.
- The laser absorptivity changes over time because molten metal has different absorptivity as compared to metal powder or solid metal [15]. However, the laser light absorption was assumed to be constant over time and a laser absorptivity of 0.38 on IN718 powder particles was chosen from Y.S.Lee [83].

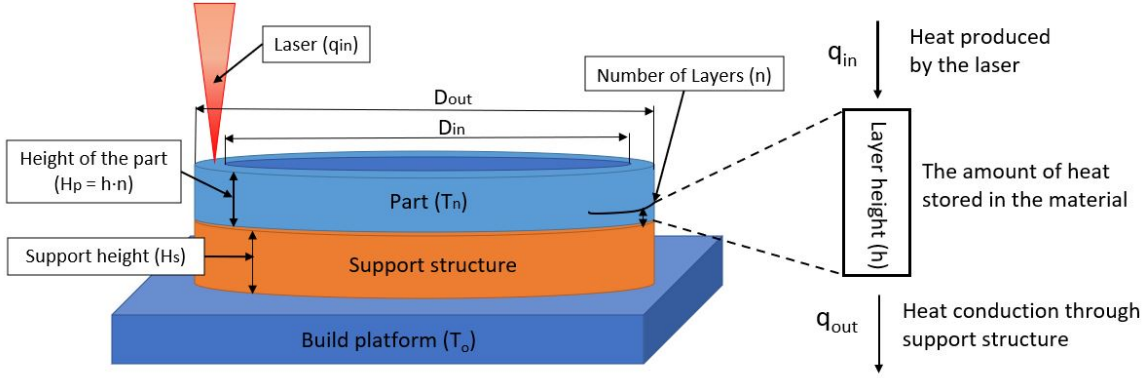


Figure 54: Geometry used for the calculations of the heat build-up and solidification cooling rate.

Table 9: Process parameters used to manufacture the inlet housing part and IN718 material properties used for the thermal calculations.

Properties	Quantity	References
Laser power, P (W)	285	
Laser absorption (on powder), η	0.38	[50]
Scanning speed, v (mm/s)	Confidential	
Hatch distance, w (μm)	110	
Area of the support structure, A (mm^2)	4712.39	
Laser-off time, Δt_{L-off} (s)	10	
Density, ρ (g/cm^3)	8.24	[53]
Build platform temperature, T_0 (K)	353	
Thermal conductivity, k ($\text{J}/(\text{mm s K})$)	0.0114	[50]
Specific heat, C_p ($\text{J}/(\text{g K})$)	0.435	[50]
Fraction of the support structure, f_s	0.5	
Ageing temperature, T_{ageing} (K)	893	[78, 79]
Solidification temperature, $T_{solidus}$ (K)	1533	[50]
Support height, H_s (mm)	17.34	
Outer diameter, D_{out} (mm)	170	
Inner diameter, D_{in} (mm)	160	

The heat build-up after melting n layers of powder particles on the support structure was calculated by the following formula:

$$h \rho C_p (T_n - T_0) = \frac{P \eta}{v w} - k f_s \Delta t \frac{T_n - T_0}{H_s}, \quad (6)$$

where the left-hand side of the equation represents the amount of heat stored into the material (q). The terms h , ρ , C_p , T_n and T_0 are the layer thickness, the density of the material, the specific heat, the nominal temperature after manufacturing n layers and the temperature of the build plate, respectively. The first and second terms of the right-hand side of the equation are the heat produced by laser (q_{in}) and the heat conducted out by the support structure (q_{out}), respectively. The term η is the laser absorptivity, k is the thermal conductivity, f_s is the volume fraction of the support structure ($0 < f_s < 1$) where 1 represents solid material and H_s is the height of the support structure. The term Δt consists of the laser-off time (recoating cycle) and the laser exposure time. The derivation to obtain Equation 6 can be found in Appendix I. The multifid term $h C_p \rho$ is the energy required to heat the block and it was neglected since the energy was a lot less than the energy conducted out [50]. Rewriting Equation 6, the heat build-up after depositing 1 layer ($n = 1$) on the support structure is obtained:

$$T_1 = T_0 + \frac{P \eta H_s}{v w f_s k \Delta t}. \quad (7)$$

The effect of the support height and the support volume fraction on the heat build-up can be seen in Figure 55a. The temperature resulting of the first layer manufactured on support structure using a support height of $H_s = 17.34 \text{ mm}$ and a volume fraction of $f_s = 50 \%$ was only 410 K and 381 K by manufacturing on solid material. The heat build-up was relatively low since the area exposed by the laser resulted in a high laser-on time. By knowing the nominal heat build-up after manufacturing the first solid layer on the support structure, the cooling condition can be determined by using the classic Rosenthal solution for a moving point heat source providing a quasi-steady-state temperature distribution for a thick plate [50]:

$$T(x, y, z) - T_0 = \frac{q_{in}}{2 \pi k} \frac{1}{R} \exp\left[\frac{v}{2 \alpha_{IN718}} (R - x)\right], \quad (8)$$

where T is the temperature at a given position (x, y, z) , x is the laser-direction, y is transfer direction, z is the build-direction, $R = \sqrt{x^2 + y^2 + z^2}$ is the radial distance from that particular location (in this research at $(0,0,0)$) to the laser centre line of the heat source and x is the distance from that point to the heat source [84]. The distance from a location to the heat source can be calculated by the laser speed multiplied to the time $x = v t$. The thermal diffusivity α_{IN718} is calculated by the following equation:

$$\alpha_{IN718} = \frac{k}{\rho * C_p}. \quad (9)$$

Inserting the heat build-up (410 K) and volume fraction of the support structure ($f_s = 50 \%$) into Equation 8, a cooling curve was calculated along the longitudinal track of the weld line by taking $y = 0$ and $z = 0$. Another cooling curve was plotted without support structure assuming a support height of $H_s = 0$, leading to a heat build-up of $T_1 \approx T_0$ by using Equation 7. The results obtained are shown in Figure 55b. The latent heat was neglected. From this curve, the solidification cooling rate was calculated by taken derivative at the point where the cooling curve intersects with the solidification temperature (1533 K). Another parameter taken from the cooling curve was the cooling time from solidification to the ageing temperature (893 K) of the material IN718 which is important for the formation of strengthening precipitates γ' and γ'' . The results are shown in Table 10.

The solidification cooling rate of the case with a support structure compared to the case without indicates why the OT images reveal high thermal radiation on the transition from the support structure to solid material. The difference in cooling time between the case with and without support is only 1.9 ms. The cooling time (T_{cool}) or time spent at high temperature is extremely low (within milliseconds), indicating why heat treatments are needed to obtain the strengthening precipitates γ' and γ'' . The microstructure in this region of the inlet housing part was not examined, so the influence of lower solidification cooling rate on the microstructure was not investigated.

Table 10: Table showing the results of the heat build-up, solidification rate and cooling time for manufacturing the part with and without support structure.

Case	Heat build-up (K)	Solidification cooling rate CR_s (K/s)	Cooling time t_{cool} (ms)
With support structure	410	$8.84 \cdot 10^5$	1.6
Without support structure	381	$4.00 \cdot 10^5$	3.7

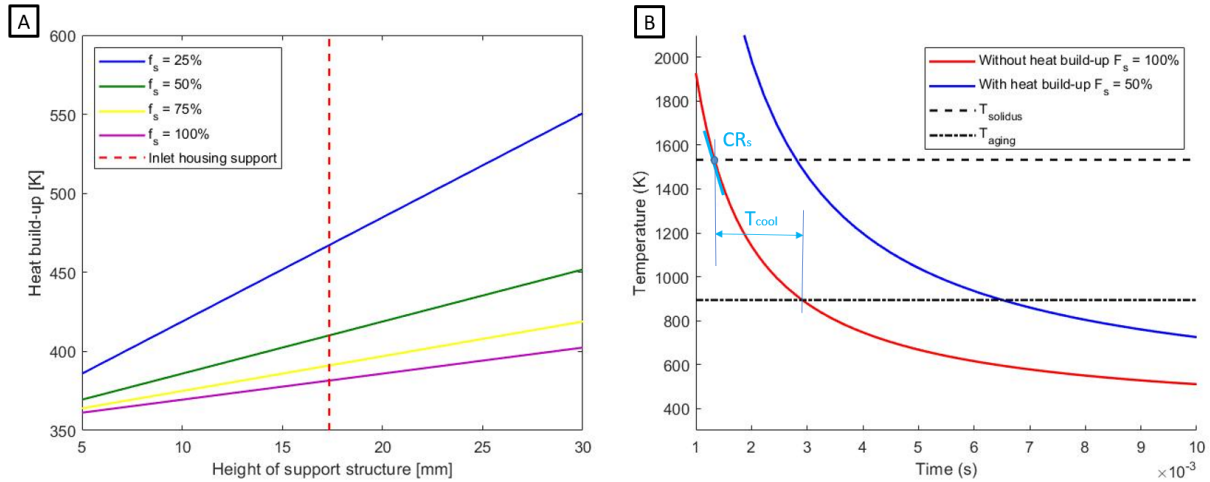


Figure 55: (a) Graph showing the effect of the support height on the heat build-up for different values of volume fraction. The red vertical line indicates the height of the support structure used to manufacture the inlet housing part. (b) The cooling curve by manufacturing on solid material with no heat build-up and the cooling curve with heat build-up, manufacturing on support structure.

5.1.2 The outer ring section

The solidification cooling rate was calculated on the outer ring (see previous section), which is the transition from the support structure to the first build-layer of the outer ring, see Figure 3 and 33. The results revealed a lower solidification cooling rate in that region, see Table 10. The lower solidification cooling rate presumably led to notable lower hardness, besides also warping up to 2 mm was observed, see Appendix A. The thermal stresses exceed the bonding strength of the material with the support structure, leading to warping. To remove the support structure, post-processing is needed afterwards. Taking this into consideration, the support structure could be entirely manufactured with solid material to avoid the warping and possible recoater crashes. However, this increases the manufacturing time of the inlet housing. To optimize the manufacturing time, the first section of the support structure can be manufactured with support process parameters, see Table 5. The last layers of the support structure, minimal of 50 layers (≈ 2 mm), with infill process parameters, see Table 5. The warping phenomenon will be displaced to the support structure, but it will not influence the part. Using this method, the solidification cooling rate and heat build-up will move more towards the same value of other regions located in the part, creating a more homogeneous and stable manufacturing process and probably similar hardness values.

5.1.3 The upper ring section

The upper ring showed higher thermal radiation due to the lower heat dissipation through the thin-walled section underneath, see Figure 33. The hardness of the upper ring in the as-built state was lower as compared to other features with mean thermal radiation, see Figure 53. The outer ring in the as-built state also showed lower hardness with high radiation on the OT images. The high thermal radiation indicated lower cooling rates and it was assumed that the lower cooling rates caused a lower hardness. To obtain similar cooling rates in the upper ring compared to other features, the process parameters can be changed to use a lower heat input. Besides, it is expected that a longer laser-off time decreases the heat build-up of the upper ring. A lower starting temperature slightly increases the solidification cooling rate (see Equation 8) and decreasing thermal radiation. Another solution can be a change in the design of the inlet housing part, for example, thicker section underneath the upper ring.

5.1.4 The vanes section

The vanes showed high thermal radiation only at the top half of the part (see Figure 56). It became clear that the higher thermal radiation of the vanes was caused by the lack of powder distributed after a recoating cycle, see Figure 56b. The reason for the absence of powder laying on top of the vanes was attributed to warping of the vanes during solidification. During solidification, thermal stresses were formed and warping occurred when the thermal stresses exceeded the strength of the material. In overhang regions, the warping effect becomes more severe because of the insufficient firm bonding between the powder particles of the previous layer and the material manufactured on powder particles, see Figure 58a [65]. Figure 58a shows the warping phenomenon of an overhang surface where the manufactured angle θ' is smaller than the theoretical angle θ of the CAD file. The warping phenomenon accumulates after manufacturing multiple layers, which influence the layer thickness of the next layer, leading to larger warping [65]. When the warping exceeds the layer thickness of the next layer, no room is left for powder particles to be distributed by the recoater. This was presumably the reason for the lack of powder distributed over the vanes, as shown in Figure 56a and Appendix E. The influence of the gas (argon) volume flow or speed over the build plate has not been investigated further. It is clear that warping causes the effect of no powder distribution. Otherwise, the powder bed images would also show on other locations (i.e. 45-degree) no powder distribution after a recoater cycle.

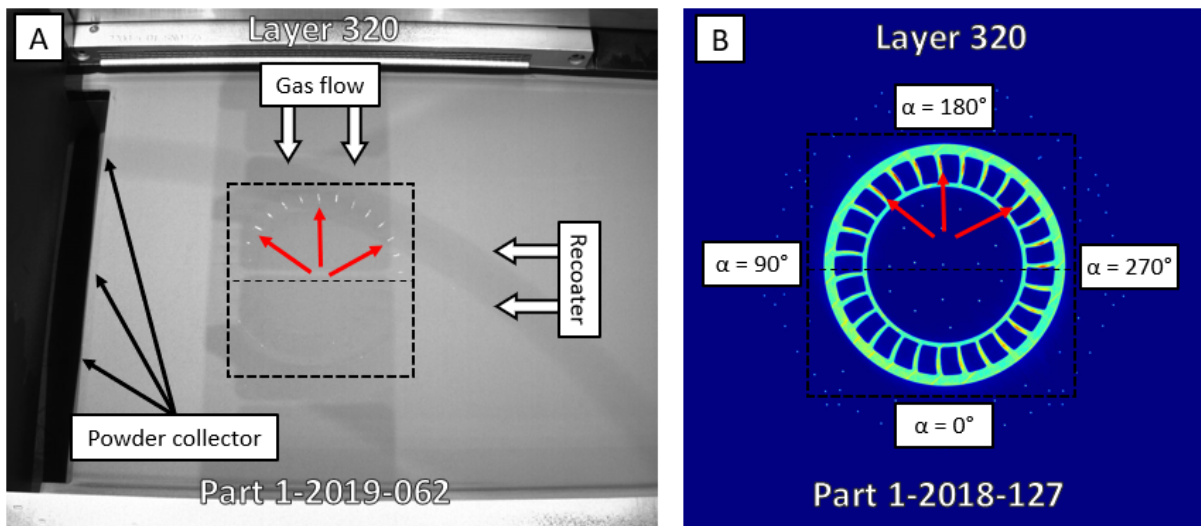


Figure 56: (a) Powder bed image showing no powder distributed at certain regions of the vanes after a recoating cycle, located on the top side of the part, indicated with the red arrows. (b) showing the high thermal radiation from the vanes at the location with no powder distributed, as seen in (a). The orientation of the vanes relative to the recoater direction (α) is also indicated. Note that the OT-image was taken from another inlet housing part, but the process parameters and shape of the vanes were similar.

The reason why the warping only occurred at the top of the part was attributed to the recoater direction and the orientation of the vanes, see figure 58b and 58c. The vanes have a 30-degree overhang constructed in the clockwise direction. The orientation of the overhang of the vanes relative to the recoater direction (α) is defined in Figure 57. The vanes with the higher local thermal radiation (upper half of the part) are oriented according to Figure 58c where the force (F_b) is pointing upwards to the right, so the warping is promoted by the recoater when moving from the left to the right. Figure 58b shows the situation of the vanes without higher radiations where the force is pointed downwards and the recoater suppresses the warping [17]. This was concluded by K. Zhang et al. [17]. They manufactured

specimens with different inclination angles and different orientations of the overhangs compared to the recoater direction, see Figure 59. They found that the forming properties of the overhangs became more superior with an increasing polar coordinate, where a polar coordinate of 0° relates to Figure 58b and a polar coordinate of $\alpha = 180^\circ$ is shown in Figure 58c. The warpage level of the specimens, expressed by Δh in Figure 59, vary with different α . The figure shows a crash of the sharp corner by using α of 180° and this can also lead to interruption of an overhang (part of the overhang is not attached to the main part).

The above-discussed phenomenon, depicted in Figure 58b and 58c, primarily applies to hard recoater types, also used in this research made of the high-speed steel. Soft recoaters have the same function as hard recoaters to distribute powder particles. However, they are made from a softer material that can slightly give way, in case the recoater collides with a metal part being built. The soft recoater can prevent build stops or models from being dragged across the powder bed.

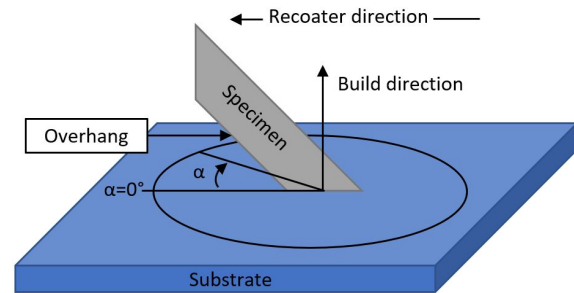


Figure 57: Schematic overview of an overhang's orientation relative to the recoater direction, expressed

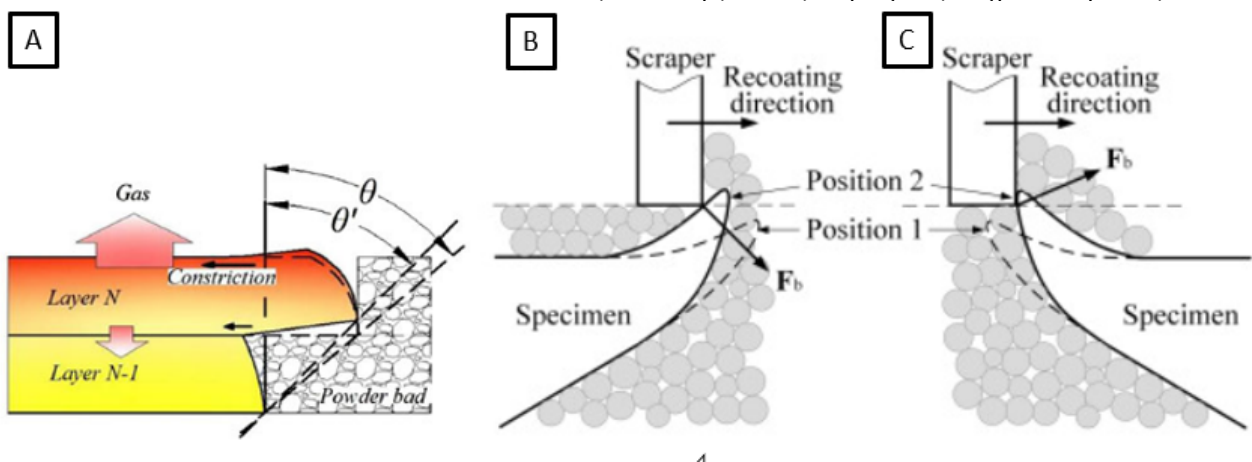


Figure 58: (a) showing the warping principle, (b) the warping interaction with the recoater direction of the vanes located on the bottom half of Figure 56 ($\alpha = 0^\circ$) and (c) warping accumulation with the vanes located on the upper half ($\alpha = 180^\circ$) [16, 17].

D. Wang et al. designed and manufactured samples with an overhang angle of 45° to 25° with the build plate [65]. The samples with an inclination angle larger than 40° were well fabricated while samples with inclination lower than 35° were subjected to warping. They concluded that overhangs lower than 35° are hard to fabricate without support structures. The two main defects of the difficult manufacturing of overhangs with small inclination angles were as follows [65]. The heat conduction rate of powder supported zone is only $1/100^{th}$ compared to the solidly supported zone. So, by using the same process parameters, the absorbed energy is higher in powder supported regions, leading to larger melt pools and the melt pool sinks into the powder due to the gravity force [16]. The other main defect is the warping phenomenon of the overhanging surface as explained earlier. D. Wang et al. also studied the important factors for the fabrication quality of overhanging structures [16]. They concluded by manufacturing smaller inclination angles, higher scanning speeds or lower laser power reduces the effect of warping and melt pool sinkage through the powder [16]. The residual stresses are increased cumulatively by an increasing number of layers of an overhang.

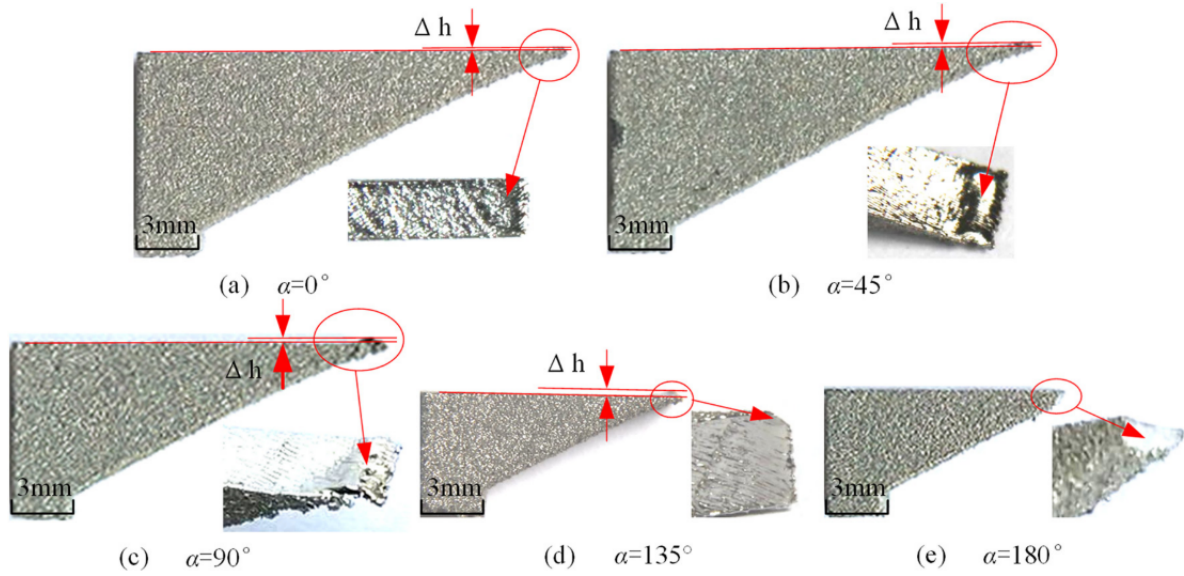


Figure 59: Specimens with the same inclination angle of 25° but created at different angles of α [17]. The warpage level Δh deviates by different values of α and increases by larger angles of α .

5.2 Microstructure development

This section discusses the development of the as-built microstructure.

5.2.1 The dendritic as-built microstructure

The as-built microstructure of the inlet housing part showed a cellular dendritic structure. The development of the as-built microstructure is controlled by the ratio of the thermal gradient (G) over the solidification rate (R), as explained in Chapter 2. Higher G/R ratios lead a stable planar structure and lower ratios lead to cells and dendrites. The condition when undercooling occurs for binary alloys under steady state solidification is shown in the following equation:

$$\frac{G}{R} < \frac{T_L - T_s}{D}, \quad (10)$$

where T_L is the liquidus temperature, T_s is the solidus temperature and D is the diffusivity of the solute in liquid. At a given value of G , conditional undercooling happens in front of the liquid-solid solidification interface when the solidification velocity exceeds certain values [18]. As a consequence, the planar interface becomes unstable and cellular dendrites growth in the direction of the thermal gradient [8]. This phenomenon was also observed in this research where a dendritical solidification structure was dominant. Besides also a zig-zag pattern was observed. The heat flux direction in the melt pool is pointed to the centre of the melt pool during solidification, creating the zig-zag pattern.

In this research, vertical dendrites at the centre of the melt pools were observed and growing through the melt pool boundaries, depicted in Figure 48. Besides, a 90° rotation of the dendrites at the melt pool boundaries was also recognized, creating a zig-zag pattern illustrated in Figure 60. The figure and explanation are taken from Calandri et al. [18]. The development of the dendrites in the as-built state can be explained as follows: The matrix of IN718 is the γ phase with an FCC crystal structure, having three equivalent and orthogonal $[100]$, $[010]$ and $[001]$ directions (90° rotated from each other), and a preferred crystal growth along the $[001]$ axis [18]. Figure 60 shows that the dendrites develop along their preferred $[001]$ axis. If the thermal gradient direction after the melt pool boundary aligns

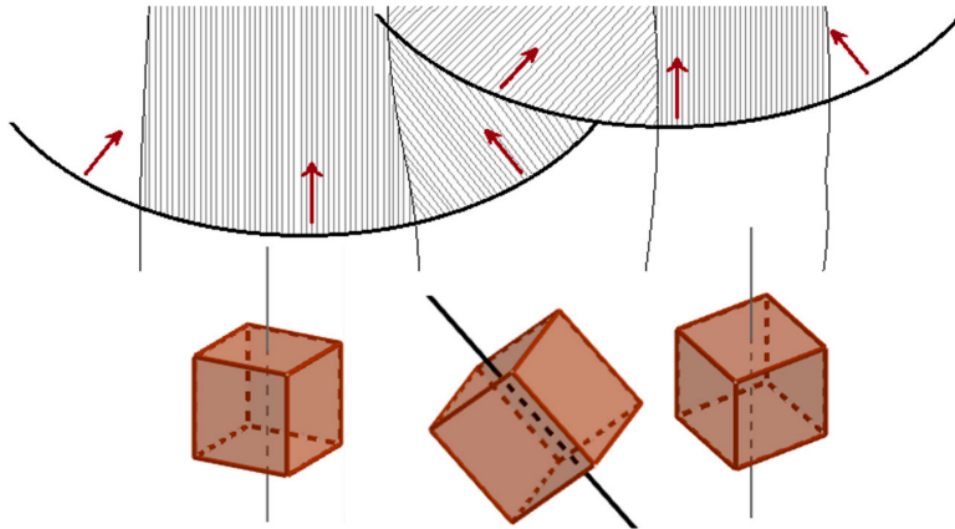


Figure 60: Schematic overview of the direction of the dendrites and the columnar grains with different crystalline orientations. The dendrites in the middle change their direction at melt pool boundaries, rotated 90° and pointed to the direction of the thermal gradient, creating a zigzag pattern [18].

most closely with the primary dendrite, for example [001] direction, the dendrites grow through the melt pool boundary. The primary dendrite with [001] direction must have the secondary dendrites arm along the [100] or [010] directions. If the heat flux direction after the melt pool boundary is changing, the [100] or [010] secondary dendrite arm, of the underlying [001] primary dendrite arm, would grow preferentially and become the new primary dendrite arm, because the [100] or [010] aligns more closely to the heat flux direction than the [001], according to D. Deng et al. [29]. This phenomenon explains the dendrites' 90° zig-zag pattern, but in both cases, no new grain and no additional nuclei are generated in the liquid ahead of the solid/liquid interface. So, the grains can also cross the melt pool boundaries.

A dendritic arm spacing between 0.5 and $2 \mu\text{m}$ was observed in this research and had a mean value of $1 \mu\text{m}$, given in Chapter 4.5.4, which is comparable with literature [18, 29, 47, 50, 56]. Figure 48 shows that the dendritic arm spacing slightly deviates. The dendritic arm spacing should be smaller in the bottom of the melt pool and become larger in the top since the cooling rates are reduced upon solidification [18]. Song et al. calculated a dendrite arm spacing of $1.6 \mu\text{m}$ with similar solidification cooling rates calculated in this study for a solid structure, see Table 10 [50]. Microscopic analysis revealed a primary dendrite arm spacing of $1 - 1.8 \mu\text{m}$, so the dendrite arm spacing observed in this research is very common for the L-PBF manufacturing process. Popovich et al. observed dendrite arm spacing of $2-3 \mu\text{m}$ but used a higher LED than employed in the current study [85]. They obtained long elongated columnar grains and larger melt pool sizes, leading to lower cooling rates, thus larger dendrites were obtained.

5.2.2 Grain structure

The inlet housing part was constructed with consecutive solidified layers during the L-PBF process. The laser caused an extremely fast melting of the powder particles of each layer, and even the previously manufactured layers were also partially remelted. As the laser passed the melt pool, the molten metal solidified due to the heat loss via convection with the atmosphere and the heat conduction through the substrate underneath. The solidification of the material occurred through two competing phenomena: epitaxial growth of columnar grains and heterogeneous nucleation of new grains [18]. Heterogeneous nucleation occurs when the newly formed crystals are interrupting the growth of the underlying grains.

The crystals at the liquid-solid interface, have a different crystalline orientation than the crystals of the previous layer. Epitaxial grain growth occurs when the newly formed crystals, at the liquid-solid interface, have the same crystalline orientation with respect to the underlying crystals. The large elongated grains, mainly in the z-direction, were obtained in the microstructure, which indicated a strong tendency of epitaxial grain growth from layer to layer, also observed by [18, 56, 85, 86]. The melt pool boundaries were not visible in the grain structure due to the strong epitaxial growth of the grains from one layer to the next. Grains longer than 200 μm were observed with a layer thickness of 40 μm .

The number of grains was measured on different locations of the inlet housing part. The bulk bottom was predicted to have more grains as compared to the bulk top based on literature [23, 52] and the higher thermal radiation found in the OT images, as seen in Figure 31. Wang et al. reported, with similar linear energy density, smaller columnar grains in the bottom of the part than the top, due to the higher cooling rates in the bottom [52]. However, smaller grains in the bottom was not the case in this research. The strong epitaxial growth of the grains could be a reason for no significant differences in the number of grains. Another important factor was the area used to measure the grain size. The EBSD analysis was only performed once at each feature with a relatively small area of 400 μm by 300 μm as compared to the areas typically employed in literature [5, 23]. The area's size was limited due to the thickness of the vanes and a distance of at least 200 μm from the edges to prevent measuring grains of agglomerate powder particles or layers with no consecutive layers on top. Apart from the reason that the measured area covered multiple melt pools, it is expected that more reliable results are obtained by measuring at least three times in different regions of each feature or by taking larger measurement areas.

In this research, the grains' size was calculated by taking the number of pixels of each grain multiplied by the area of the pixel. To compare the grain size with literature, the circle equivalent diameter was calculated by using the following equation:

$$D_e = 2 \sqrt{\frac{A_{\text{grain}}}{\pi}}, \quad (11)$$

where D_e and A_{grains} are the circle equivalent diameter and the area of the grain, respectively [87]. The mean grain area of the heat-treated samples was 340 μm^2 and substituted this in Equation 11, a circle equivalent diameter of 21 μm was obtained. This value is lower compared to literature. A. Mostafa et al. observed with similar process parameters and an additional homogeneous heat treatment a grain size between 30-50 μm measured on an area of 575 μm by 450 μm [5].

5.3 Effect of the heat treatment

The purpose of the heat treatment applied in this research was to obtain a homogenized microstructure with the solution heat treatment to promote the diffusion of segregation elements and dissolve the brittle phases (i.e. carbides and Laves phases) into the austenite matrix. Followed by a precipitation heat treatment to generate the primary strengthening precipitates γ' and γ'' to optimize the mechanical properties of the IN718 part [80], as discussed before. The solution heat treatment applied in this research almost completely dissolved the Laves phase and distributed the Nb elements throughout the γ matrix, according to [29]. This makes Nb available for the strengthening precipitate γ'' . The disk-shaped γ'' precipitates were also observed in the heat-treated microstructure, as can be seen in Figure 50b and 50c. The γ'' has a BCT crystal structure and grows coherently with the γ matrix as disk-shaped particles on the {001} plane of the FCC matrix, with the c-axis (c/a ratio of 2.04, see Chapter 2) of the BCT structure perpendicular to the disk plane [88]. So, three variants of the γ'' phase are possible. The reason why the disk-shaped particles are parallel or 90° rotated within the same grain is because of the FCC crystal

structure.

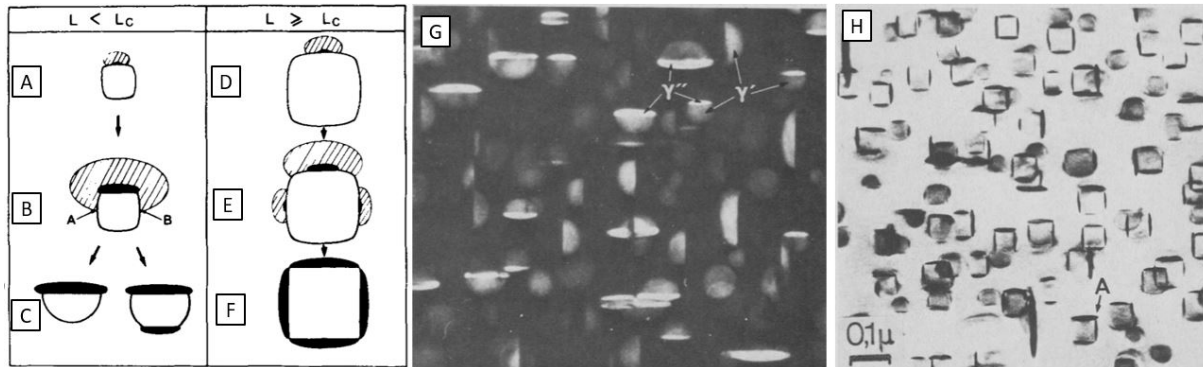


Figure 61: (a-f) Schematic diagram with the morphology of the γ'' and γ' above a given size L of γ' particles. For further understanding, see text. TEM micrographs obtained (g) after homogenisation for 48 h at 1200°C and ageing heat treatment of IN718 for 700°C for 524 hours and (H) for 770°C for 19 hours [19].

The γ' precipitates were too small to be clearly observed even by high-resolution SEM. R. Cozar and A. Pineau [19] found γ'' precipitates are always adjacent to the γ' precipitates and the most typical morphologies are shown in Figure 61c. In this figure the formation of the strengthening precipitates is shown where L is the size of the γ' precipitates and L_c is the critical size of the γ' precipitates. R. Cozar and A. Pineau reported that the critical size was around 20 nm [19]. Consider a small γ' precipitate where a γ'' precipitate (black disk-shaped) is nucleated on one of the six faces of the γ' (round cube-shaped), see Figure 61a. For a slight increase in the size of the γ' , the γ'' tends to overlap the precipitate and the Nb concentration is lowered in the diffusion zone around it, see Figure 61b. The lower Nb concentration around the γ'' precipitates (hatch zone) reduces the probability for forming new γ'' precipitates in that area (at A or B) and leads to the formation of smaller γ'' particles parallel to it, as depicted in Figure 61c and g. By using a higher ageing temperature, larger γ' particles can be formed and they can develop more easily, see Figure 61 d-f and h. The rounded square represents the γ' precipitates and the black disk-shaped region represents the γ'' precipitates. Precipitates up to 300 nm are found at an ageing temperature of 750°C at 524 hours by [88]. At higher magnification of the SEM micrograph of Figure 50c it seems that some γ' precipitates can be observed, see Figure 62. However, TEM analysis is needed to observe these precipitates more clearly, as mentioned before. Cao et al. observed γ' precipitates with a size of 20 nm using similar heat treatment as employed in this research [80].

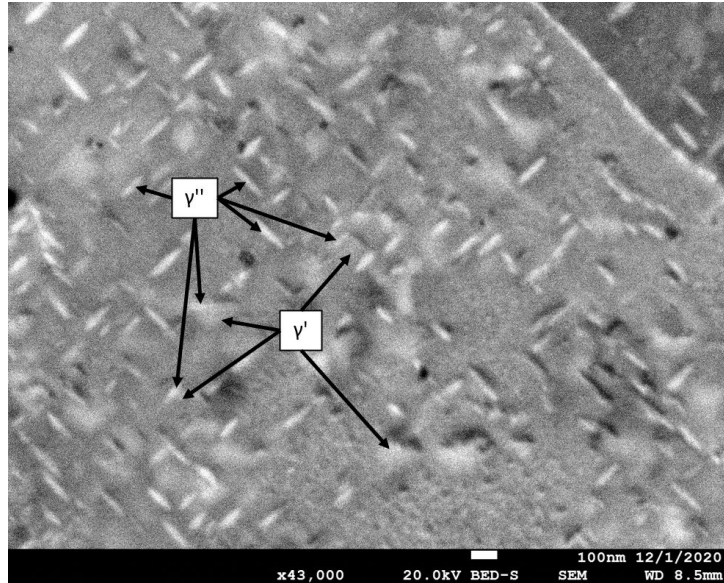


Figure 62: SEM micrograph showing γ'' precipitates and possible γ' precipitates. This micrograph shows the heat-treated bulk bottom (HT-1), taken from Figure 50c with higher magnification.

Besides, also white irregular-shaped precipitates mainly at grain boundaries are observed, as shown in Figure 50b and c. Similar white spots at the grain boundaries, with comparable size, in heat-treated samples, were revealed using EDS and X-ray diffractometer analysis and they were mentioned to be coarse MC-carbides $(0.9Nb0.1Ti)C$ [5, 89].

6 Conclusions

The microstructure and (mechanical) properties of a complex-shaped aerospace part manufactured through laser powder bed fusion (L-PBF) have been investigated. The part was cut into smaller samples to perform measurements on the following specific geometrical features: The bulk bottom, the bulk top, the 45-degree overhang and the vanes. The results were evaluated with the Optical Tomography (OT) in-process monitoring system and assessed on their detection limits. The influence of the post-manufacturing heat treatment on the resulting microstructure and the (mechanical) properties was also studied. The following conclusions were drawn to answer the research questions given in Chapter 1.3:

- Gas-induced porosity was predominant in the complex aerospace part, but the density was still within the requirement of 8.1 g/cm^3 . Besides, micro-scaled cracks on the surface and lack of fusion porosity type were also observed, which is not allowed according to the requirements. It is anticipated that the lack of fusion porosity type can be decreased by increasing the width of the melt pools (i.e. increasing laser power or decreasing laser speed) or decreasing the hatch spacing.
- The average surface roughness was measured on the horizontal, the vertical, the up-skin and the down-skin of a 45-degree surface. Only the horizontal surface was according to the requirements of $3.175 \text{ }\mu\text{m}$ and the 45-degree down-skin surface showed the highest average surface roughness due to the sintered powder particles and the staircase effect. Post-processing after manufacturing is needed to meet the surface roughness requirement in certain areas.
- The as-built part showed an inhomogeneous dendritic microstructure with Laves phase and MC carbides within interdendritic regions. The average primary dendritic arm spacing was $1 \text{ }\mu\text{m}$, while no considerable variations were observed between different geometrical features. Columnar grains almost parallel to the building direction were observed due to heat dissipation towards the build plate and strong epitaxial growth. No relation between grain size and different geometrical features could be observed.
- The heat-treated microstructure revealed MC carbides and nanoscale disk-shaped γ'' strengthening precipitates distributed throughout the γ -matrix and on the grain boundaries. γ' precipitates were too small to be observed with the high-resolution scanning electron microscope. The heat-treated samples showed larger grains, while smaller grains had disappeared.
- The differences in local process conditions led to variations in the mechanical properties of the different geometrical features as observed through hardness measurements. The hardness of the heat-treated samples increased with an average of 33 % compared to the as-built hardness due to the formation of strengthening precipitates. Besides, inhomogeneities in the mechanical properties between different features were removed after the heat treatment.
- Geometrical features with lower cooling rates had an unfavourable effect on the hardness. The OT system could not be linked to defects such as porosity and higher surface roughness.

Finally, more research in post-processing is needed to smooth the surfaces and remove microcracks for adequate preparation to the inlet housing part to meet the requirements for the aerospace industry.

6.1 Recommendations

It is recommended to further investigate how to avoid the warping of the vanes to prevent possibly recoater crashes in the future. No distortion measurements of the vanes were conducted, so the effect of the warping phenomenon on the dimensional requirements of the vanes could not be analysed in detail. The vanes had a low inclination angle (30 degrees with the build plate) and it was expected that it cannot be altered in the design stage. As a result, the orientation of the vanes could also not be adjusted. The remaining important task would be to adjust the process parameters or to add support structures to improve the vanes' quality.

The outer ring manufactured on the support structure experienced more heat build-up, lower cooling rates, slightly lower hardness and warping of the sides. To prevent this, the support structure could be manufactured from completely solid material. Another option to optimize the build speed is to manufacture the last 50 layers of the support structure with completely solid material (infill process settings). The aspects mentioned above will be moved to the support structure but do not influence the part's quality.

6.2 Future work

Less complex and smaller sized parts might provide a better understanding of the meaning of local spots with higher thermal radiation. In this research, it was challenging to trace the specific location with high thermal radiation on the OT images back to the specific location within the part, for example the vanes. Thereby, small defects (i.e. process induced porosity or higher surface roughness) could not be linked to the OT images. After embedding, grinding and polishing, the local porosity was not traceable anymore. It is recommended to make X-ray Computed Tomography (CT) scans of parts with regions that showed remarkably higher or lower thermal radiation on the OT images and make sure that these specific locations can be traced back properly.

It was concluded that the etching procedure caused contamination on the samples. It seemed that etchant remains in pores, microcracks and gaps in the transition regions between the embedded resin and the sample. It was not washed away after cleaning, and the hairdryer blows the liquid out and over the surface, which created these branches like contamination. Further investigation (non-destructive analysis such as Liquid Penetrant Testing) should be done in order to discover if there are pores, microcracks and gaps present in the part that could not be observed by the microscope. These small defects could have adverse effect on the mechanical properties of the part.

References

- [1] K. Yun Feng, P. Liu, H. Xue Li, S. Yu Sun, S. Bo Xu, and J. Ning Li, "Microstructure and phase transformation on the surface of Inconel 718 alloys fabricated by SLM under 1050°C solid solution + double ageing," *Vacuum*, vol. 145, pp. 112 – 115, 2017. [Online]. Available: <http://www.sciencedirect.com/science/article/pii/S0042207X17310928>
- [2] J. Oliveira, A. LaLonde, and J. Ma, "Processing parameters in laser powder bed fusion metal additive manufacturing," *Materials Design*, vol. 193, p. 108762, 2020. [Online]. Available: <http://www.sciencedirect.com/science/article/pii/S0264127520302963>
- [3] H. K. D. H. Bhadeshia, "Nickel based superalloys," <https://www.phase-trans.msm.cam.ac.uk/2003/Superalloys/superalloys.html>.
- [4] B. Hassan and J. Corney, "Grain boundary precipitation in Inconel 718 and Inconel 718plus," *Materials Science and Technology*, vol. 33, no. 16, pp. 1879–1889, 2017. [Online]. Available: <https://doi.org/10.1080/02670836.2017.1333222>
- [5] A. Mostafa, I. Rubio, V. Brailovski, M. Jahazi, and M. Medraj, "Structure, texture and phases in 3D printed Inconel 718 alloy subjected to homogenization and HIP treatments," *Metals - Open Access Metallurgy Journal*, vol. 7, p. 196, 05 2017.
- [6] L. Scime and J. Beuth, "Melt pool geometry and morphology variability for the Inconel 718 alloy in a laser powder bed fusion additive manufacturing process," *Additive Manufacturing*, vol. 29, p. 100830, 2019. [Online]. Available: <http://www.sciencedirect.com/science/article/pii/S2214860419306104>
- [7] M. Ni, C. Chen, X. Wang, P. Wang, R. Li, X. Zhang, and K. Zhou, "Anisotropic tensile behavior of in situ precipitation strengthened Inconel 718 fabricated by additive manufacturing," *Materials Science and Engineering: A*, vol. 701, pp. 344 – 351, 2017. [Online]. Available: <http://www.sciencedirect.com/science/article/pii/S0921509317308651>
- [8] P. Collins, D. Brice, P. Samimi, I. Ghamarian, and H. Fraser, "Microstructural control of additively manufactured metallic materials," *Annual Review of Materials Research*, vol. 46, pp. 63–91, 2016.
- [9] S. Manikandan, D. Sivakumar, and M. Kamaraj, "1 - physical metallurgy of alloy 718," in *Welding the Inconel 718 Superalloy*, S. Manikandan, D. Sivakumar, and M. Kamaraj, Eds. Elsevier, 2019, pp. 1 – 19. [Online]. Available: <http://www.sciencedirect.com/science/article/pii/B9780128181829000013>
- [10] D. Du, A. Dong, D. Shu, G. Zhu, B. Sun, X. Li, and E. Lavernia, "Influence of build orientation on microstructure, mechanical and corrosion behavior of Inconel 718 processed by selective laser melting," *Materials Science and Engineering: A*, vol. 760, pp. 469 – 480, 2019. [Online]. Available: <http://www.sciencedirect.com/science/article/pii/S0921509319306161>
- [11] S.-H. Sun, Y. Koizumi, T. Saito, K. Yamanaka, Y.-P. Li, Y. Cui, and A. Chiba, "Electron beam additive manufacturing of Inconel 718 alloy rods: Impact of build direction on microstructure and high-temperature tensile properties," *Additive Manufacturing*, vol. 23, pp. 457 – 470, 2018. [Online]. Available: <http://www.sciencedirect.com/science/article/pii/S2214860417303214>
- [12] M. Leary, "4 - surface roughness optimisation for selective laser melting (SLM): Accommodating relevant and irrelevant surfaces," in *Laser Additive Manufacturing*, ser. Woodhead Publishing Series in Electronic and Optical Materials, M. Brandt, Ed. Woodhead Publishing, 2017, pp. 99 – 118. [Online]. Available: <http://www.sciencedirect.com/science/article/pii/B978008100433300004X>
- [13] G. Zenzinger, J. Bamberg, A. Ladewig, T. Hess, B. Henkel, and W. Satzger, "Process monitoring of additive manufacturing by using optical tomography," in *AIP Conference Proceedings*, vol. 1650, no. 1. American Institute of Physics, 2015, pp. 164–170.
- [14] AMS2774, "Heat treatment nickel alloy and cobalt alloy parts," SAE, Tech. Rep., 05 2016.
- [15] G. Fu, D. Z. Zhang, A. N. He, Z. Mao, and K. Zhang, "Finite element analysis of interaction of laser beam with material in laser metal powder bed fusion process," *Materials*, vol. 11, no. 5, p. 765, 2018.
- [16] D. Wang, Y. Yang, Z. Yi, and X. Su, "Research on the fabricating quality optimization of the overhanging surface in SLM process," *The International Journal of Advanced Manufacturing Technology*, vol. 65, no. 9-12, pp. 1471–1484, 2013.
- [17] K. Zhang, Z. Mao, G. Fu, D. Z. Zhang, C. Liu, and Z. Li, "A feasible method of support slimming based on the different thresholds of polar angles in selective laser melting," *Materials & Design*, vol. 157, pp. 501–511, 2018.
- [18] M. Calandri, S. Yin, B. Aldwell, F. Calignano, R. Lupoi, and D. Uguet, "Texture and microstructural features at different length scales in Inconel 718 produced by selective laser melting," *Materials*, vol. 12, no. 8, p. 1293, 2019.

- [19] R. Cozar and A. Pineau, "Morphology of γ' and γ'' precipitates and thermal stability of inconel 718 type alloys," *Metallurgical Transactions*, vol. 4, no. 1, pp. 47–59, 1973.
- [20] H. Qi, M. Azer, and A. Ritter, "Studies of standard heat treatment effects on microstructure and mechanical properties of laser net shape manufactured inconel 718," *Metallurgical and Materials Transactions A*, vol. 40, no. 10, pp. 2410–2422, 2009.
- [21] D. Zhang, Z. Feng, C. Wang, W. Wang, Z. Liu, and W. Niu, "Comparison of microstructures and mechanical properties of inconel 718 alloy processed by selective laser melting and casting," *Materials Science and Engineering: A*, vol. 724, pp. 357 – 367, 2018. [Online]. Available: <http://www.sciencedirect.com/science/article/pii/S0921509318304301>
- [22] S. Metals, "Inconel 718," https://www.specialmetals.com/assets/smc/documents/inconel_alloy_718.pdf.
- [23] G. Bean, T. McLouth, D. Witkin, S. Sitzman, P. Adams, and R. Zaldivar, "Build orientation effects on texture and mechanical properties of selective laser melting inconel 718," *Journal of Materials Engineering and Performance*, vol. 28, no. 4, pp. 1942–1949, 2019.
- [24] I. Baturynska, O. Semeniuta, and K. Martinsen, "Optimization of process parameters for powder bed fusion additive manufacturing by combination of machine learning and finite element method: A conceptual framework," *Procedia CIRP*, vol. 67, pp. 227 – 232, 2018, 11th CIRP Conference on Intelligent Computation in Manufacturing Engineering, 19-21 July 2017, Gulf of Naples, Italy. [Online]. Available: <http://www.sciencedirect.com/science/article/pii/S2212827117311484>
- [25] L. Cordova, T. Bor, M. de Smit, S. Carmignato, M. Campos, and T. Tinga, "Effects of powder reuse on the microstructure and mechanical behaviour of al–mg–sc–zr alloy processed by laser powder bed fusion (lpbf)," *Additive Manufacturing*, vol. 36, p. 101625, 2020.
- [26] B. A. B. Ropio, "Validation of metal additive manufacturing parts."
- [27] A. Sharman, A. Amarasinghe, and K. Ridgway, "Tool life and surface integrity aspects when drilling and hole making in inconel 718," *Journal of Materials Processing Technology*, vol. 200, no. 1, pp. 424 – 432, 2008. [Online]. Available: <http://www.sciencedirect.com/science/article/pii/S0924013607008382>
- [28] T. Trosch, J. Strößner, R. Völkl, and U. Glatzel, "Microstructure and mechanical properties of selective laser melted inconel 718 compared to forging and casting," *Materials Letters*, vol. 164, pp. 428 – 431, 2016. [Online]. Available: <http://www.sciencedirect.com/science/article/pii/S0167577X15307850>
- [29] D. Deng, R. L. Peng, H. Brodin, and J. Moverare, "Microstructure and mechanical properties of inconel 718 produced by selective laser melting: Sample orientation dependence and effects of post heat treatments," *Materials Science and Engineering: A*, vol. 713, pp. 294–306, 2018.
- [30] S. S. Tavares, J. S. Corte, and J. M. Pardal, "Failure of 17-4 ph stainless steel components in offshore platforms," in *Handbook of Materials Failure Analysis with Case Studies from the Oil and Gas Industry*. Elsevier, 2016, pp. 353–370.
- [31] S. Azadian, "Aspects of precipitation in alloy inconel 718," Ph.D. dissertation, Luleå tekniska universitet, 2004, godkänd; 2004; 20061026 (haneit).
- [32] J. R. Davis and A. I. H. Committee, *Nickel, Cobalt, and Their Alloys*, ser. ASM specialty handbook. ASM International, 2000. [Online]. Available: <https://books.google.nl/books?id=15BUAAAAMAAJ>
- [33] S. Ghorbanpour, M. Zecevic, A. Kumar, M. Jahedi, J. Bicknell, L. Jorgensen, I. J. Beyerlein, and M. Knezevic, "A crystal plasticity model incorporating the effects of precipitates in superalloys: Application to tensile, compressive, and cyclic deformation of inconel 718," *International Journal of Plasticity*, vol. 99, pp. 162 – 185, 2017. [Online]. Available: <http://www.sciencedirect.com/science/article/pii/S0749641917303182>
- [34] P. Mignanelli, N. Jones, E. Pickering, O. Messé, C. Rae, M. Hardy, and H. Stone, "Gamma-gamma prime-gamma double prime dual-superlattice superalloys," *Scripta Materialia*, vol. 136, pp. 136 – 140, 2017. [Online]. Available: <http://www.sciencedirect.com/science/article/pii/S1359646217302051>
- [35] S. Ghosh, S. Yadav, and G. Das, "Study of standard heat treatment on mechanical properties of inconel 718 using ball indentation technique," *Materials Letters*, vol. 62, no. 17, pp. 2619 – 2622, 2008. [Online]. Available: <http://www.sciencedirect.com/science/article/pii/S0167577X08000232>
- [36] M. Sundararaman, P. Mukhopadhyay, and S. Banerjee, "Carbide precipitation in nickel base superalloys 718 and 625 and their effect on mechanical properties," *Superalloys*, vol. 718, pp. 625–706, 1997.

- [37] J. J. Schirra, R. H. Caless, and R. W. Hatala, "The effect of laves phase on the mechanical properties of wrought and cast + hip inconel 718," *The Minerals, Metals & Materials Society*, pp. 375–388.
- [38] V. Popovich, E. Borisov, A. Popovich, V. Sufiiarov, D. Masaylo, and L. Alzina, "Impact of heat treatment on mechanical behaviour of inconel 718 processed with tailored microstructure by selective laser melting," *Materials Design*, vol. 131, pp. 12 – 22, 2017. [Online]. Available: <http://www.sciencedirect.com/science/article/pii/S0264127517305476>
- [39] G. Knorovsky, M. Cieslak, T. Headley, A. Romig, and W. Hammetter, "Inconel 718: a solidification diagram," *Metallurgical transactions A*, vol. 20, no. 10, pp. 2149–2158, 1989.
- [40] M. Chiumenti, M. Cervera, A. Salmi, C. A. De Saracibar, N. Dialami, and K. Matsui, "Finite element modeling of multi-pass welding and shaped metal deposition processes," *Computer methods in applied mechanics and engineering*, vol. 199, no. 37-40, pp. 2343–2359, 2010.
- [41] J. R. D. BY R. G. THOMPSON and D. E. MAYO, "The effect of heat treatment on microfissuring in alloy 718," *WELDING RESEARCH SUPPLEMENT*, pp. 299 – 304, 1986. [Online]. Available: https://app.aws.org/wj/supplement/WJ.1986.11_s299.pdf
- [42] S. Sun, M. Brandt, and M. Easton, "2 - powder bed fusion processes: An overview," in *Laser Additive Manufacturing*, ser. Woodhead Publishing Series in Electronic and Optical Materials, M. Brandt, Ed. Woodhead Publishing, 2017, pp. 55 – 77. [Online]. Available: <http://www.sciencedirect.com/science/article/pii/B9780081004333000026>
- [43] J. Gockel and J. Beuth, "Understanding ti-6al-4v microstructure control in additive manufacturing via process maps," in *Solid freeform fabrication proceedings*. Univ. Tex. Austin, 2013, pp. 666–674.
- [44] T. G. Gallmeyer, S. Moorthy, B. B. Kappes, M. J. Mills, B. Amin-Ahmadi, and A. P. Stebner, "Knowledge of process-structure-property relationships to engineer better heat treatments for laser powder bed fusion additive manufactured inconel 718," *Additive Manufacturing*, vol. 31, p. 100977, 2020. [Online]. Available: <http://www.sciencedirect.com/science/article/pii/S2214860419314538>
- [45] S. Manikandan, D. Sivakumar, and M. Kamaraj, "2 - solidification of alloy 718," in *Welding the Inconel 718 Superalloy*, S. Manikandan, D. Sivakumar, and M. Kamaraj, Eds. Elsevier, 2019, pp. 21 – 46. [Online]. Available: <http://www.sciencedirect.com/science/article/pii/B9780128181829000025>
- [46] T. DebRoy, H. Wei, J. Zuback, T. Mukherjee, J. Elmer, J. Milewski, A. Beese, A. Wilson-Heid, A. De, and W. Zhang, "Additive manufacturing of metallic components – process, structure and properties," *Progress in Materials Science*, vol. 92, pp. 112 – 224, 2018. [Online]. Available: <http://www.sciencedirect.com/science/article/pii/S0079642517301172>
- [47] Z. Wang, K. Guan, M. Gao, X. Li, X. Chen, and X. Zeng, "The microstructure and mechanical properties of deposited-in718 by selective laser melting," *Journal of Alloys and Compounds*, vol. 513, pp. 518 – 523, 2012. [Online]. Available: <http://www.sciencedirect.com/science/article/pii/S0925838811020767>
- [48] X. Wang, X. Gong, and K. Chou, "Scanning speed effect on mechanical properties of ti-6al-4v alloy processed by electron beam additive manufacturing," *Procedia Manufacturing*, vol. 1, pp. 287 – 295, 2015, 43rd North American Manufacturing Research Conference, NAMRC 43, 8-12 June 2015, UNC Charlotte, North Carolina, United States. [Online]. Available: <http://www.sciencedirect.com/science/article/pii/S2351978915010264>
- [49] A. Popovich, V. S. Sufiiarov, E. Borisov, I. Polozov, and D. Masaylo, "Design and manufacturing of tailored microstructure with selective laser melting," *Mater. Phys. Mech*, vol. 38, no. 1, pp. 1–10, 2018.
- [50] H. Song, T. McGaughy, A. Sadek, and W. Zhang, "Effect of structural support on microstructure of nickel base superalloy fabricated by laser-powder bed fusion additive manufacturing," *Additive Manufacturing*, vol. 26, pp. 30 – 40, 2019. [Online]. Available: <http://www.sciencedirect.com/science/article/pii/S2214860418306845>
- [51] J. Ströfßner, M. Terock, and U. Glatzel, "Mechanical and microstructural investigation of nickel-based superalloy in718 manufactured by selective laser melting (slm)," *Advanced Engineering Materials*, vol. 17, no. 8, pp. 1099–1105, 2015.
- [52] X. Wang, T. Keya, and K. Chou, "Build height effect on the inconel 718 parts fabricated by selective laser melting," *Procedia Manufacturing*, vol. 5, pp. 1006 – 1017, 2016, 44th North American Manufacturing Research Conference, NAMRC 44, June 27-July 1, 2016, Blacksburg, Virginia, United States. [Online]. Available: <http://www.sciencedirect.com/science/article/pii/S2351978916301019>
- [53] L. C. Wei, L. E. Ehrlich, M. J. Powell-Palm, C. Montgomery, J. Beuth, and J. A. Malen, "Thermal conductivity of metal powders for powder bed additive manufacturing," *Additive Manufacturing*, vol. 21, pp. 201–208, 2018.

- [54] P. Kumar, J. Farah, J. Akram, C. Teng, J. Ginn, and M. Misra, "Influence of laser processing parameters on porosity in inconel 718 during additive manufacturing," *The International Journal of Advanced Manufacturing Technology*, vol. 103, no. 1-4, pp. 1497–1507, 2019.
- [55] "Influence of processing parameters on the evolution of melt pool, porosity, and microstructures in ti-6al-4v alloy parts fabricated by selective laser melting," *Prog Addit Manuf* 2.
- [56] Q. Jia and D. Gu, "Selective laser melting additive manufacturing of inconel 718 superalloy parts: Densification, microstructure and properties," *Journal of Alloys and Compounds*, vol. 585, pp. 713 – 721, 2014. [Online]. Available: <http://www.sciencedirect.com/science/article/pii/S0925838813023451>
- [57] L. J. S. Y. e. a. Li, R., "Balling behavior of stainless steel and nickel powder during selective laser melting process," p. 1025–1035, 2012. [Online]. Available: <https://link.springer.com/article/10.1007%2Fs00170-011-3566-1#citeas>
- [58] K. Moussaoui, W. Rubio, M. Mousseigne, T. Sultan, and F. Rezai, "Effects of selective laser melting additive manufacturing parameters of inconel 718 on porosity, microstructure and mechanical properties," *Materials Science and Engineering: A*, vol. 735, pp. 182 – 190, 2018. [Online]. Available: <http://www.sciencedirect.com/science/article/pii/S0921509318310931>
- [59] H. Attar, M. Calin, L. Zhang, S. Scudino, and J. Eckert, "Manufacture by selective laser melting and mechanical behavior of commercially pure titanium," *Materials Science and Engineering: A*, vol. 593, pp. 170 – 177, 2014. [Online]. Available: <http://www.sciencedirect.com/science/article/pii/S0921509313012665>
- [60] M. Sadowski, L. Ladani, W. Brindley, and J. Romano, "Optimizing quality of additively manufactured inconel 718 using powder bed laser melting process," *Additive Manufacturing*, vol. 11, pp. 60 – 70, 2016. [Online]. Available: <http://www.sciencedirect.com/science/article/pii/S2214860416300483>
- [61] W. Tillmann, C. Schaak, J. Nellesen, M. Schaper, M. Aydinöz, and K.-P. Hoyer, "Hot isostatic pressing of in718 components manufactured by selective laser melting," *Additive Manufacturing*, vol. 13, pp. 93 – 102, 2017. [Online]. Available: <http://www.sciencedirect.com/science/article/pii/S2214860416300495>
- [62] X. Ma, H. Zhai, L. Zuo, W. Zhang, S. Rui, Q. Han, J. Jiang, C. Li, G. Chen, G. Qian, and S. Zhao, "Fatigue short crack propagation behavior of selective laser melted inconel 718 alloy by in-situ sem study: influence of orientation and temperature," *International Journal of Fatigue*, p. 105739, 2020. [Online]. Available: <http://www.sciencedirect.com/science/article/pii/S014211232030270X>
- [63] I. Koutiri, E. Pessard, P. Peyre, O. Amlou, and T. D. Terris, "Influence of slm process parameters on the surface finish, porosity rate and fatigue behavior of as-built inconel 625 parts," *Journal of Materials Processing Technology*, vol. 255, pp. 536 – 546, 2018. [Online]. Available: <http://www.sciencedirect.com/science/article/pii/S0924013617306349>
- [64] A. Triantaphyllou, C. L. Giusca, G. D. Macaulay, F. Roerig, M. Hoebel, R. K. Leach, B. Tomita, and K. A. Milne, "Surface texture measurement for additive manufacturing," *Surface Topography: Metrology and Properties*, vol. 3, no. 2, p. 024002, may 2015. [Online]. Available: <https://doi.org/10.1088%2F2051-672x%2F3%2F2%2F024002>
- [65] D. Wang, Y. Yang, R. Liu, D. Xiao, and J. Sun, "Study on the designing rules and processability of porous structure based on selective laser melting (slm)," *Journal of Materials Processing Technology*, vol. 213, no. 10, pp. 1734–1742, 2013.
- [66] D. S. Watring, K. C. Carter, D. Crouse, B. Raeymaekers, and A. D. Spear, "Mechanisms driving high-cycle fatigue life of as-built inconel 718 processed by laser powder bed fusion," *Materials Science and Engineering: A*, vol. 761, p. 137993, 2019. [Online]. Available: <http://www.sciencedirect.com/science/article/pii/S0921509319307579>
- [67] K. Solberg and F. Berto, "The effect of defects and notches in quasi-static and fatigue loading of inconel 718 specimens produced by selective laser melting," *International Journal of Fatigue*, p. 105637, 2020.
- [68] A. den Hollander, "Process window for l-pbf of in718," *MvR-19-154107*, 2020.
- [69] ASTM-B311-93, "Test method for density determination for powder metallurgy (p/m) materials containing less than two percent porosity," ASTM, Tech. Rep., 06 2002.
- [70] "Chapter 10 - underwater vehicles," in *The Maritime Engineering Reference Book*, A. F. Molland, Ed. Oxford: Butterworth-Heinemann, 2008, pp. 728 – 783. [Online]. Available: <http://www.sciencedirect.com/science/article/pii/B978075068987800010X>

- [71] A. Keropyan, "Application of non-contact technologies for measuring roughness of interacting surfaces when monitoring friction coefficient," *Materials Today: Proceedings*, 2020. [Online]. Available: <http://www.sciencedirect.com/science/article/pii/S2214785320375787>
- [72] ISO-6507-1:2018, "Metallic materials — vickers hardness test — part 1: Test method," ISO, Tech. Rep., 01 2018.
- [73] T. A. McFalls, "The effect of hydrogen on gas porosity in laser powder bed fusion of als10mg," 2018.
- [74] L. L. Parimi, R. G. A., D. Clark, and M. M. Attallah, "Microstructural and texture development in direct laser fabricated in718," *Materials Characterization*, vol. 89, pp. 102 – 111, 2014. [Online]. Available: <http://www.sciencedirect.com/science/article/pii/S1044580313003835>
- [75] D. Titus, E. James Jebaseelan Samuel, and S. M. Roopan, "Chapter 12 - nanoparticle characterization techniques," in *Green Synthesis, Characterization and Applications of Nanoparticles*, ser. Micro and Nano Technologies, A. K. Shukla and S. Iravani, Eds. Elsevier, 2019, pp. 303 – 319. [Online]. Available: <http://www.sciencedirect.com/science/article/pii/B9780081025796000125>
- [76] M. Rombouts, J. Kruth, L. Froyen, and P. Mercelis, "Fundamentals of selective laser melting of alloyed steel powders," *CIRP Annals*, vol. 55, no. 1, pp. 187 – 192, 2006. [Online]. Available: <http://www.sciencedirect.com/science/article/pii/S0007850607603953>
- [77] A. Aggarwal, "Thermo-fluidic modelling of volume shrinkage and multi phase transition during selective laser melting process," Ph.D. dissertation, 11 2015.
- [78] R. Jiang, A. Mostafaei, Z. Wu, A. Choi, P-W. Guan, M. Chmielus, and A. D. Rollett, "Effect of heat treatment on microstructural evolution and hardness homogeneity in laser powder bed fusion of alloy 718," *Additive Manufacturing*, vol. 35, p. 101282, 2020. [Online]. Available: <http://www.sciencedirect.com/science/article/pii/S2214860420306540>
- [79] E. Chlebus, K. Gruber, B. Kuźnicka, J. Kurzac, and T. Kurzynowski, "Effect of heat treatment on the microstructure and mechanical properties of inconel 718 processed by selective laser melting," *Materials Science and Engineering: A*, vol. 639, pp. 647 – 655, 2015. [Online]. Available: <http://www.sciencedirect.com/science/article/pii/S0921509315005687>
- [80] G. Cao, T. Sun, C. Wang, X. Li, M. Liu, Z. Zhang, P. Hu, A. Russell, R. Schneider, D. Gerthsen, Z. Zhou, C. Li, and G. Chen, "Investigations of γ' , γ'' and δ precipitates in heat-treated inconel 718 alloy fabricated by selective laser melting," *Materials Characterization*, vol. 136, pp. 398 – 406, 2018. [Online]. Available: <http://www.sciencedirect.com/science/article/pii/S1044580317327158>
- [81] S. Hong, W. Chen, and T. Wang, "A diffraction study of the δ phase in inconel 718 superalloy," *Metallurgical and Materials Transactions A-physical Metallurgy and Materials Science - METALL MATER TRANS A*, vol. 32, pp. 1887–1901, 08 2001.
- [82] D. Zöllner, "Grain growth," in *Reference Module in Materials Science and Materials Engineering*. Elsevier, 2016. [Online]. Available: <http://www.sciencedirect.com/science/article/pii/B9780128035818031581>
- [83] Y. Lee and W. Zhang, "Modeling of heat transfer, fluid flow and solidification microstructure of nickel-base superalloy fabricated by laser powder bed fusion," *Additive Manufacturing*, vol. 12, pp. 178–188, 2016.
- [84] D. Dye, O. Hunziker, and R. Reed, "Numerical analysis of the weldability of superalloys," *Acta materialia*, vol. 49, no. 4, pp. 683–697, 2001.
- [85] V. Popovich, E. Borisov, A. Popovich, V. S. Sufiiarov, D. Masaylo, and L. Alzina, "Functionally graded inconel 718 processed by additive manufacturing: Crystallographic texture, anisotropy of microstructure and mechanical properties," *Materials & Design*, vol. 114, pp. 441–449, 2017.
- [86] F. Liu, X. Lin, C. Huang, M. Song, G. Yang, J. Chen, and W. Huang, "The effect of laser scanning path on microstructures and mechanical properties of laser solid formed nickel-base superalloy inconel 718," *Journal of Alloys and Compounds*, vol. 509, no. 13, pp. 4505–4509, 2011.
- [87] M. Li, D. Wilkinson, and K. Patchigolla, "Comparison of particle size distributions measured using different techniques," *Particulate Science and Technology*, vol. 23, no. 3, pp. 265–284, 2005.
- [88] J. Oblak, D. Paulonis, and D. Duvall, "Coherency strengthening in ni base alloys hardened by do 22 γ' precipitates," *Metallurgical Transactions*, vol. 5, no. 1, p. 143, 1974.
- [89] G. Sjöberg, N. Ingesten, and R. Carlson, "Grain boundary δ -phase morphologies, carbides and notch rupture sensitivity of cast alloy 718," *Superalloys*, vol. 718, no. 625, pp. 603–620, 1991.

A Detailed images of the part

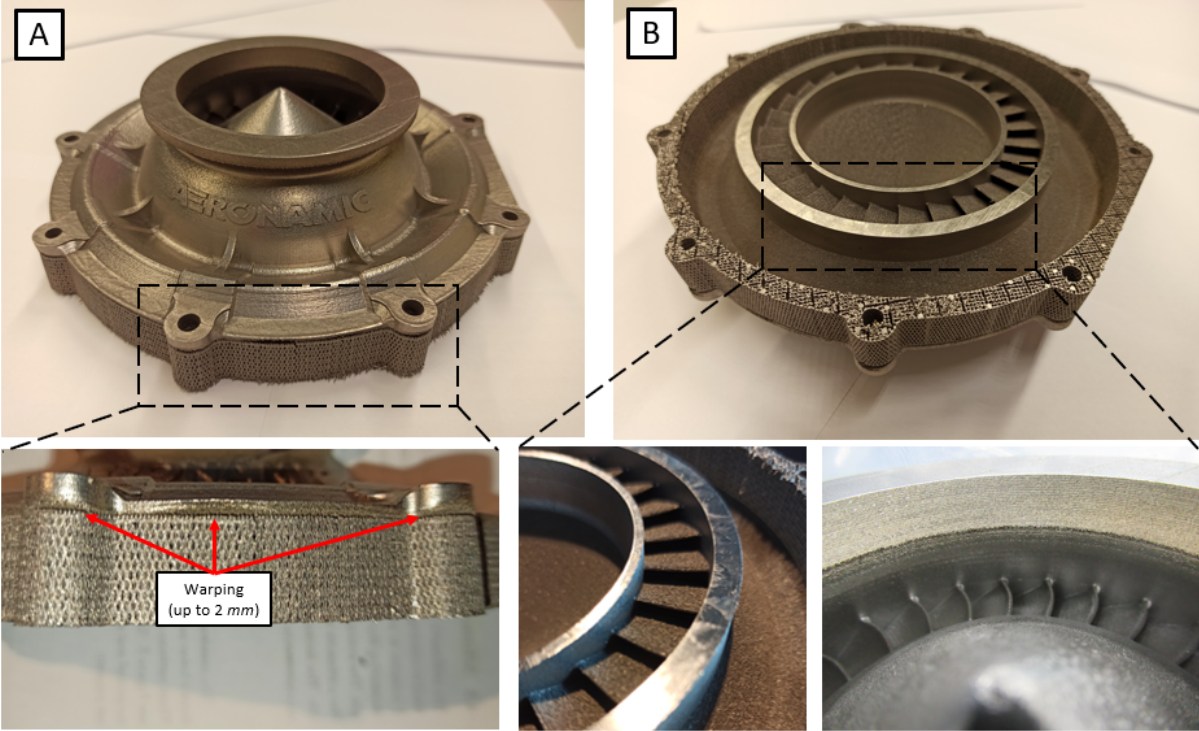


Figure 63: Detailed images of the inlet housing part, where (a) shows the front view and (b) depicts the bottom view. The transition from the support structure to the solid material exhibits warping up to 2 mm.

B Optical tomography images of the outer ring

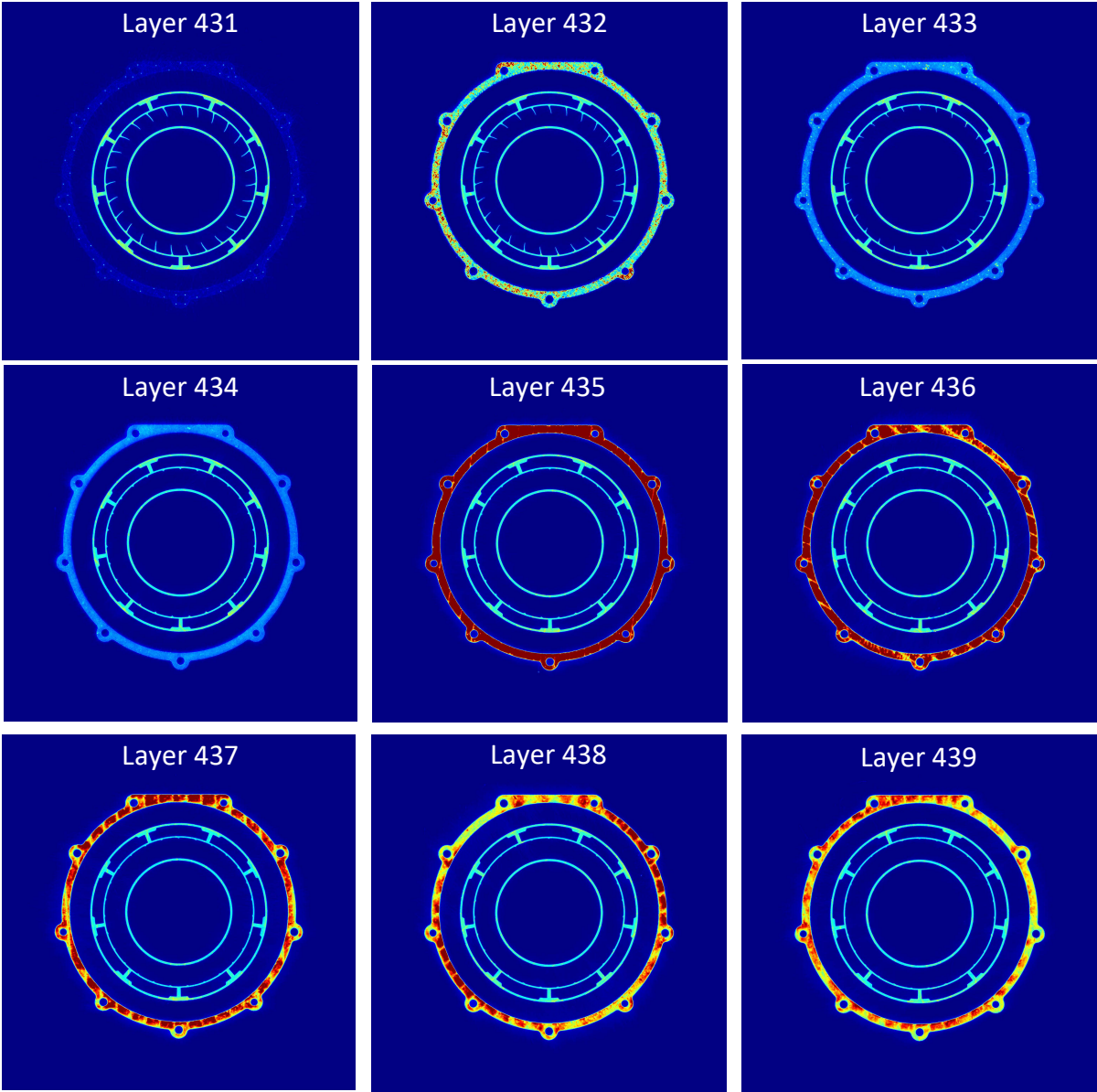


Figure 64: OT-images of the transition of support structure to the first few layers of the inlet housing part (1-2019-063). The support structure ends at layer 434 and the first layer of the inlet housing part is 435.

C Optical tomography images of the upper ring

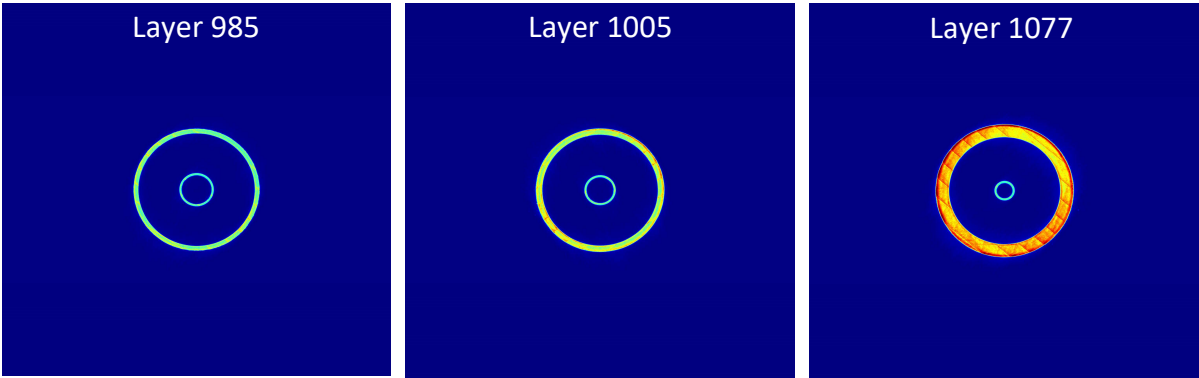


Figure 65: OT-images of the inlet housing part (1-2019-063) showing the high thermal radiation in the bulk material on the top.

D Optical tomography images of the vanes

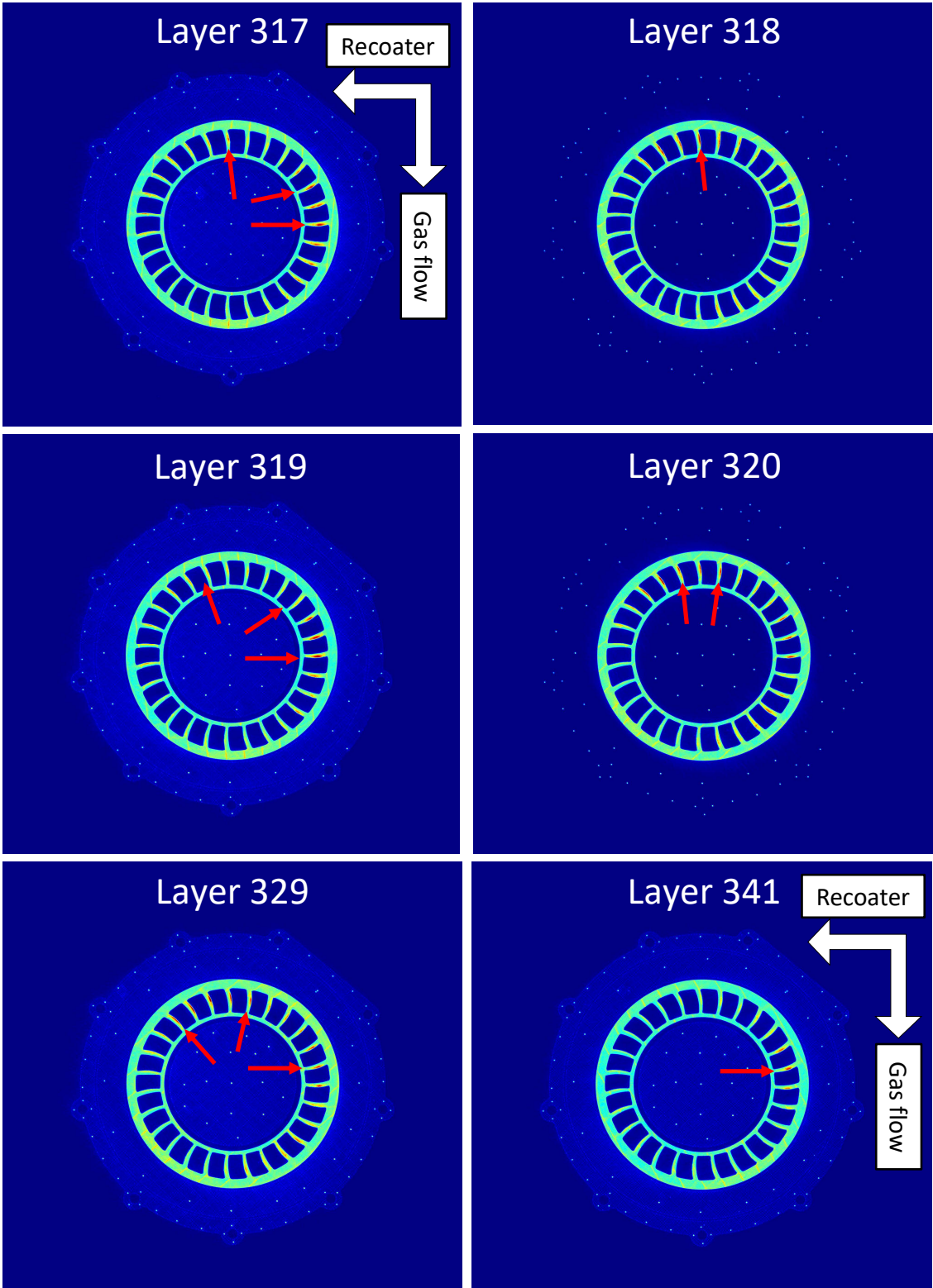


Figure 66: OT-images of the vane depicted overheating on the down-skin of the vane.

E Powder bed images of the vanes

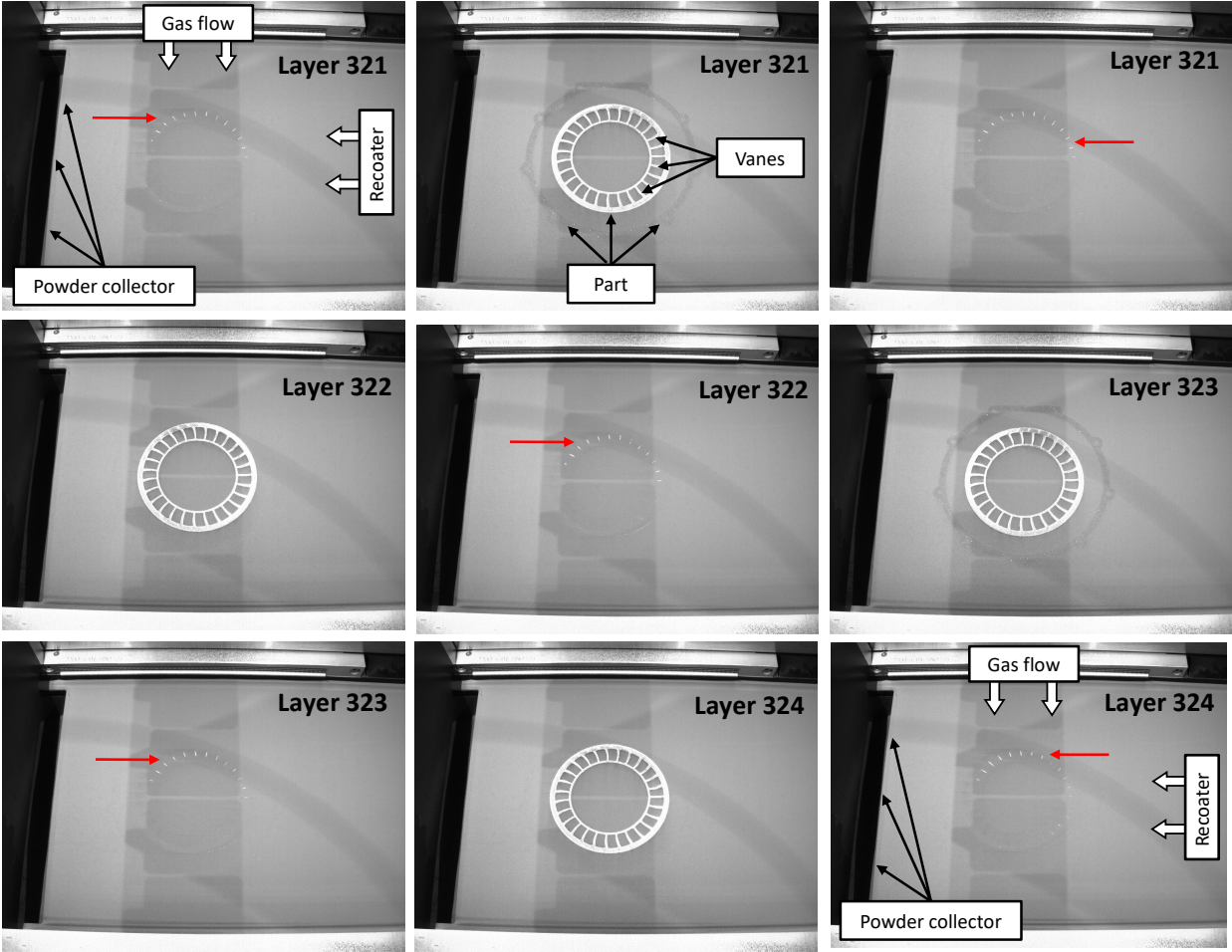
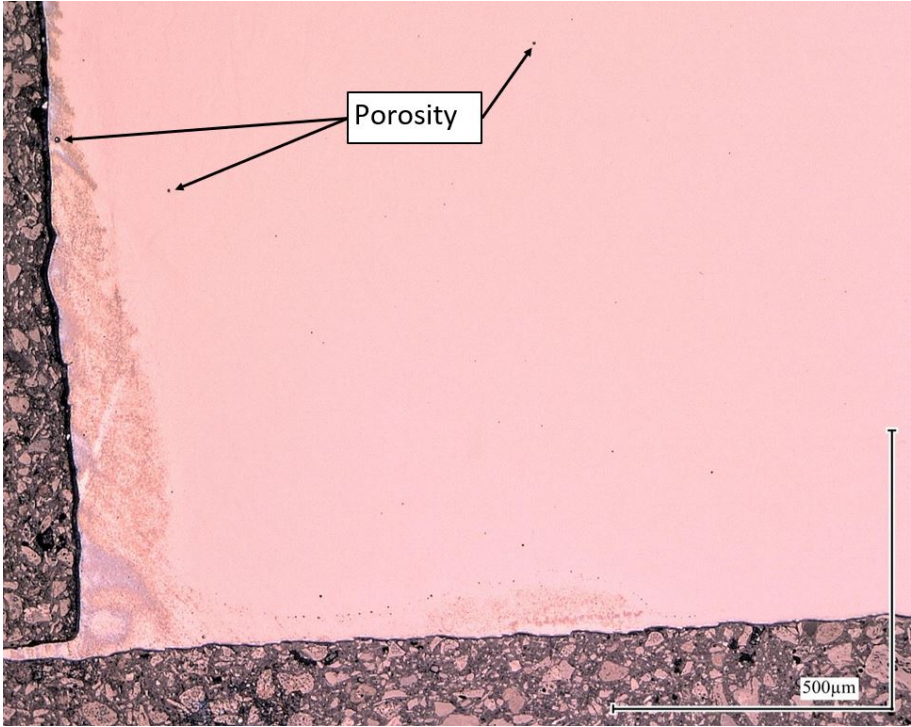
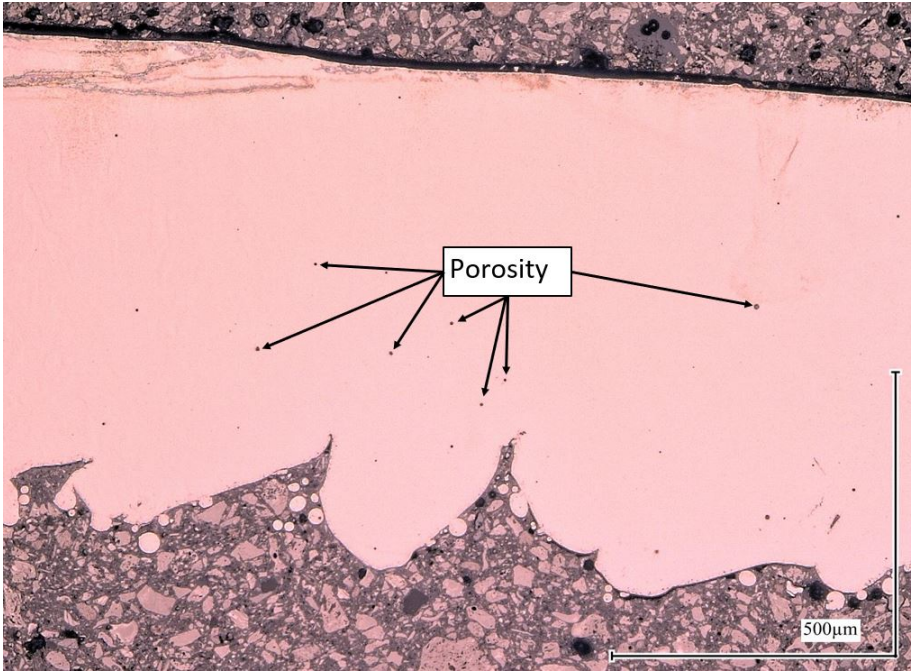


Figure 67: Powder bed images of the vanes on layer 320 to 324 indicating areas of the vanes without powder distribution after a recoater cycle.

F Micrographs showing porosity



(a) Bottom bulk (AS-1).



(b) Vane (AS-1).

Figure 68: Non etched optical images showing the porosity.

G Microstructure of the vanes

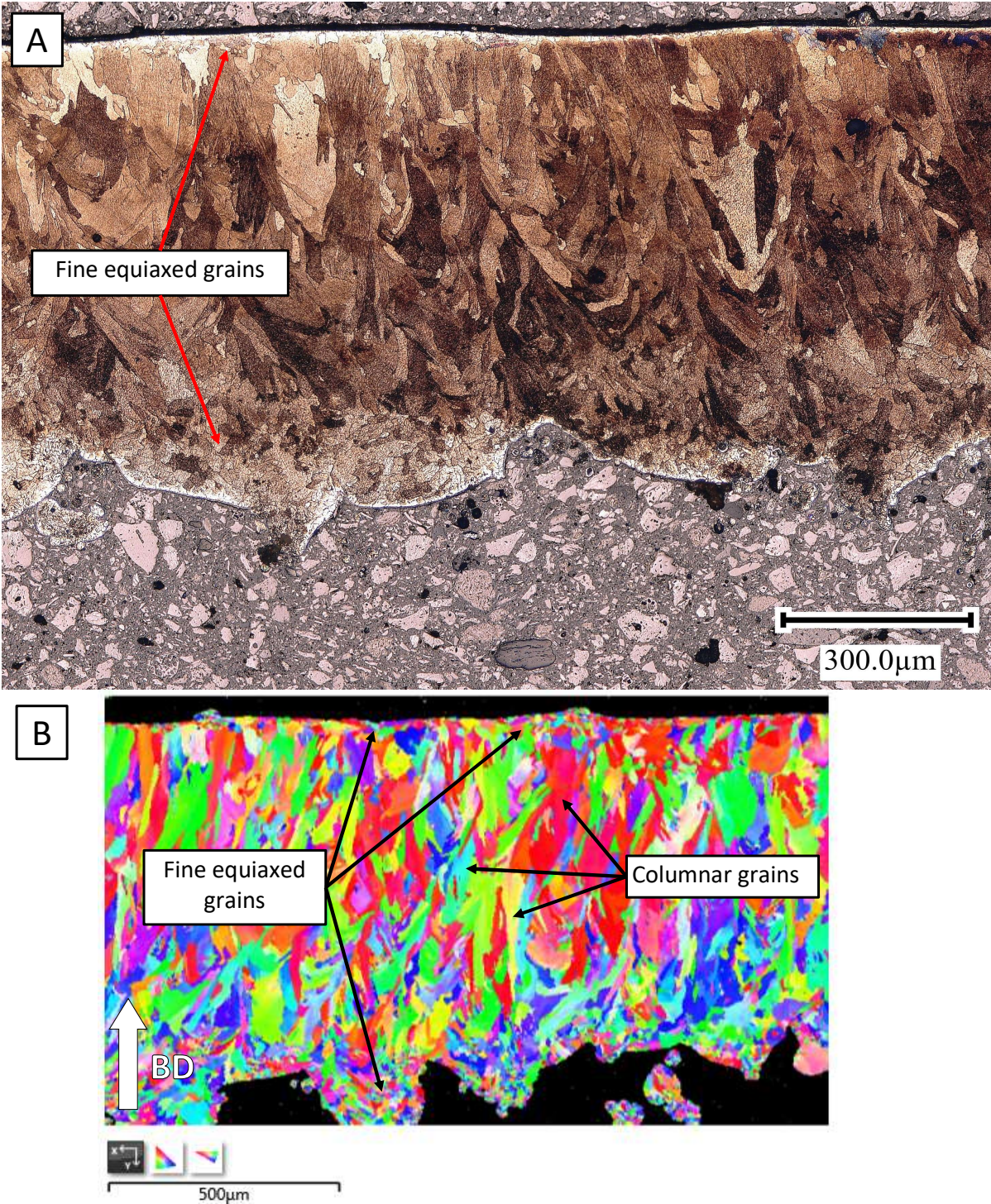


Figure 69: (a) The etched microstructure of the vane in heat-treated state and (b) EBSD analysis showing an overview of the grains in the as-build state (AS-1).

H The cause of the contamination

Two out of the three heat-treated samples showed contamination on the microstructure after the first time etching, see Figure 44. Remarkably, the as-built samples did not show the contamination on the optical micrographs. The bulk material of the heat-treated samples has multiple smaller contamination branches and the vanes show some relatively bigger ones. The contamination looks not part of the material by the reason that it crosses multiple grains and has seemingly random directions.

The following was done before the contamination was observed: The samples were cleaned with isopropanol after polishing and dried with a hair dryer. Afterwards, emerged in the etchant for 6 - 10 seconds, washed thoroughly in water, cleaned again with isopropanol and dried with a hair dryer.

Figure 44 shows the contamination with a pore. It seems that the contamination has a starting point at a pore or micro-crack and it continues to grow from there. The samples are cleaned again with isopropanol using a cotton swab which did not remove the contamination. Additional hardness measurements at the location of the contamination reveal no significant differences as compared to the uncontaminated regions. The root cause of the contamination had to be found to prevent it from occurring in the future. Two possible causes are considered:

- **Heat treatment:** The heat treatment is done in argon and it could be possible that there was still oxygen present in the furnace due to the leaking of the furnace. The heat-treated samples also have a blue/purple discolouration, which is certainly oxidation. It was expected to be removed by the grinding and polishing process. However, the oxidation might be penetrated rather deeply into the material.
- **Etching procedure:** The second cause considered is the used etching method. The etchant could cause contamination on the microstructure. The as-built samples did not show the contamination, but they are etched at another moment, with another etchant than the heat-treated samples.

Two different steps are taken to find the root cause. The first step is to grind, polish and etch two as-built and two contaminated heat-treated samples again. If the as-built and heat-treated samples exhibit contamination, the etchant must be the root cause. The results were only contamination on one of the heat-treated samples. However, the contamination was only obtained in the thin-walled section and was relatively small compared to the first time, see Figure 44b. Surprisingly, the contamination could be removed by cleaning with an alcohol-soaked cotton swab. The second step is to heat-treat two as-built samples in vacuum to exclude the presence of oxygen. After polishing and etching both samples, the optical and SEM microstructure reveals relatively small contamination, see Figure 44b. The contamination disappeared again after cleaning. Figure 70 shows a summary of the different steps taken with the contamination on the optical micrographs at each step.

It is concluded that the etching procedure causes contamination on the samples. It seems that etchant remains in pores, microcracks and gaps in the transition regions between the embedded resin and the sample. It is not washed away after cleaning, and the hairdryer blows the liquid out and over the surface, which creates these branches like contamination. It is obvious that the heat treatment did not cause the contamination. Peculiar, the contamination on the first etched samples could not be removed by proper cleaning. The explanation for this is properly that the samples are etched twice because the first time etching was not sufficiently long enough to observe a clear microstructure. Further, it is assumed to be a coincidence that the as-built samples did not contain contamination since multiple heat-treated samples also did not contain the contamination or only in certain regions.

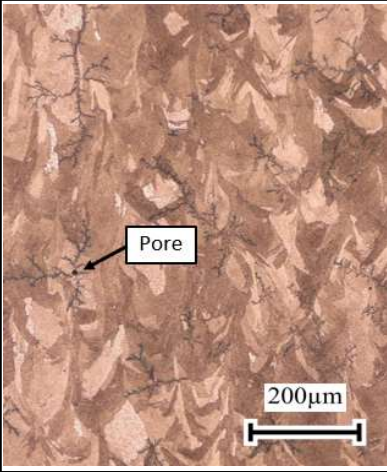
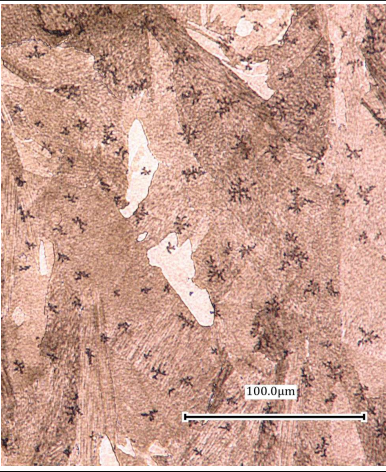
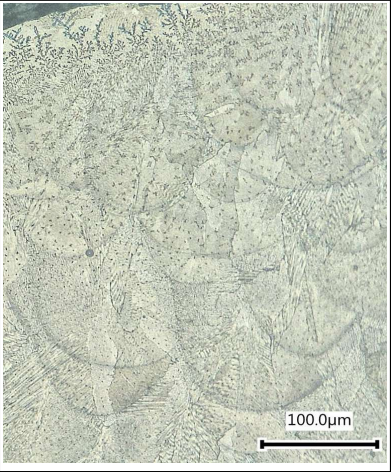
Contamination evaluation table			
	First time etching (solution and precipitation heat treatment in argon)	Second time etching (solution and precipitation heat treatment in argon)	First time etching (only precipitation heat treatment in vacuum)
Samples without contamination	AS-1, AS-7, AS-9 and HT-9	HT-1, AS-1 and AS-7	No samples
Remarks	The moment of etching was different as compared to the samples with contamination and multiple etchant was created due to the concentration loss over time.	The samples were etched with the same etchant as compared to the sample with contamination.	-
Samples with contamination	HT-1 and HT-4	HT-4	PHT-1 and PHT-4
Remarks	The samples were etched two times with the same etchant. Because the first time etching was not sufficient long enough to observe a clear microstructure.	Contamination was found in the thin-walled section. No contamination was present in the bulky regions.	Both samples showed contamination and were etched with the same etchant. Smaller and fewer contamination was found in the bulky regions.
Observed contamination			

Figure 70: Steps taken to find the root cause of the contamination and the contamination on the optical micrographs are shown at each step.

I Derivation of the thermal model

The heat build-up equation was derived by starting with the 1-dimensional (only in the z-direction) heat conduction equation:

$$\rho C_p \frac{\partial T}{\partial t} = k \frac{\partial^2 T}{\partial z^2} [50], \quad (12)$$

where z is the distance along the direction of the height. The area of the solid material, manufactured on the support structure, was calculated by using the outer diameter (D_{out}) minus the inner diameter (D_{in}) of the part, see Figure 54. By knowing the area, the left and right-hand-side of Equation 12 are multiplied with the differential volume of $A\Delta z$ (see paper [50]):

$$A h n \rho C_p \frac{\partial T}{\partial t} = q_{in} - A k f_s \frac{\partial T}{\partial z}, \quad (13)$$

where the first and second term of the left-hand side of the equation are the heat produced by laser (q_{in}) and the heat conducted out by the support structure (q_{out}). The support structure's volume fraction was added to the second term ($0 < f_s < 1$) where 1 represents solid material. The following equation calculates the heat produced by the laser per layer:

$$Q_L = q_{in} \Delta t_{L-on} = q_{in} \Delta t = \frac{q_{in} A}{v w} = \frac{P \eta A}{v w}. \quad (14)$$

The Δt consist of the laser exposure time and the laser-off time. The laser-off time is the time needed to distribute a new layer of powder and in this case, also the reaming time to manufacture the inner structure of the part that is not manufactured on the support structure, resulting in an estimation of 10 seconds laser off time. The following formula is used to approximate the laser-on time to manufacture solid material on top of the support structure:

$$\Delta t_{l-on} = \frac{A}{v w}, \quad (15)$$

where A , is the solid material area manufactured on the support structure. By integrating Equation 13 over the time for a duration of Δt the following equation is observed:

$$A H_p \rho C_p (T_n - T_0) = (q_{in} - A k f_s \frac{T_n - T_0}{H_s}) \Delta t, \quad (16)$$

where H_s is the height of the support structure and H_p the height of the solid material. Hence that the heat build up will be calculated for the first layer deposit on the support structure so $n = 1$ and therefore $H_b = h$. Dividing the equation 16 by the area (A) and substituting Equation 14 in it, the following equation is obtained:

$$h \rho C_p (T_1 - T_0) = \frac{P \eta}{v w} - k f_s \Delta t \frac{T_n - T_0}{H_s}. \quad (17)$$